Potential predictability of meridional heat and volume transports in the North Atlanic ocean

Dissertation
zur Erlangung des
Doktorgrades der Naturwissenschaften
im Fachbereich Geowissenschaften
der Universität Hamburg

vorgelegt von
Bente Tiedje
aus Hannover
Hamburg 2012

Als Dissertation angenommen
vom Fachbereich für Geowissenschaften der Universität Hamburg

auf Grund der Gutachten von
Prof. Dr. Johanna Baehr
und
Dr. Armin Köhl

Hamburg, den 29. Januar 2013
Prof. Dr. Dirk Gajewski
(Vorsitzender des Fach-Promotionsausschusses)

Abstract

The North Atlantic meridional overturning circulation (AMOC) and the associated meridional heat transport (MHT) play a fundamental role in the North Atlantic climate variability on multi-decadal time scales and are therefore of high interest for potential climate predictions. While several potential predictability studies exist for the AMOC at individual latitudes, the potential predictability remains mostly unstudied for the MHT. In this thesis, I analyze both the potential predictability of the AMOC and of the MHT, with a dedicated focus on their latitude-dependence and their interrelation.

To analyze the potential predictability on inter-annual to decadal times scales, I generate retrospective model simulations (hindcast ensembles) based on an oceanic state estimate (GECCO). I use two potential predictability measures (prognostic potential predictability and anomaly correlation) to assess the potential predictability structures for the North Atlantic. I initially analyze the potential predictability structures of the MHT and the AMOC separately, and then jointly.

For the MHT, I find a latitude-dependent potential predictability structure that indicates a clear separation between the subpolar and the subtropical regime. Decomposing the MHT shows that the gyre component controls the subpolar potential predictability structure of the MHT, while the overturning component controls the subtropical potential predictability structure of the MHT.

For the AMOC, I find a latitude-dependent potential predictability structure that is dynamically based on the potential predictability structure of the AMOC's geostrophic part. The geostrophic part is estimated by removing the wind-driven Ekman transport and by using the thermal wind relation based on the zonal density gradients. A detailed analysis of the density gradient variability indicates the dominant role of the western boundary for the potential predictability of the AMOC.

The joint analysis of the AMOC and the MHT shows that only the potential predictability of their geostrophic parts are related. The separate analyses of the MHT and the AMOC already suggest that the potential predictability structures of the MHT's overturning component and the AMOC are comparable at subtropical latitudes. But the missing link can only be found if one relates the potential predictability structure of the thermal wind transport to the MHT's overturning component from which the Ekman heat transport has been removed.

The results from this study emphasize that the potential predictability of the MHT and the AMOC can neither be interchanged with each other nor be generalized from one latitude to the entire North Atlantic.

Zusammenfassung

Die nordatlantische meridionale Umwälzzirkulation (AMOC) und der assoziierte meridionale Wärmetransport (MHT) spielen eine fundamentale Rolle in der multidekadischen Klimavariabilität des Nordatlantiks und sind deshalb von großem Interesse für potentielle Klimavorhersagen. Die potentielle Vorhersagbarkeit der AMOC wurde bereits in mehreren Studien untersucht, während die potentielle Vorhersagbarkeit des MHT weitestgehend unbeachtet blieb. In dieser Doktorarbeit untersuche ich hingegen die potentielle Vorhersagbarkeit beider Größen, wobei ich mich besonders auf die Breitenabhängigkeit und das Verhältnis beider Größen zueinander konzentriere.

Um die potentielle Vorhersagbarkeit auf einer Zeitskala von mehreren Jahren bis Dekaden zu untersuchen, generiere ich retrospektive Modellsimulationen (Ensembles), die auf einer Zustandsschätzung des Ozeans (GECCO) basieren. Für die Berechnung der potentiellen Vorhersagbarkeitsmuster für den Nordatlantik verwende ich zwei Metriken, die "anomaly correlation" und die "prognostic potential predictability". Die potentiellen Vorhersagbarkeitsmuster des MHT und der AMOC werden zunächst einzeln und danach in Verbindung analysiert.

Das Muster der potentiellen Vorhersagbarkeit des MHT weist auf eine klare Trennung zwischen dem subpolaren und dem subtropischen Regime hin. Die Dekomposition des MHT zeigt, dass die Wirbelkomponente des MHT das Vorhersagbarkeitsmuster des MHT in subpolaren Breiten maßgeblich beeinflusst, während die Umwälzkomponente des MHT das Vorhersagbarkeitsmuster des MHT in subtropischen Breiten maßgeblich beeinflusst.

Die dynamische Grundlage des potentiellen Vorhersagbarkeitsmusters der AMOC bildet das Vorhersagbarkeitsmuster des geostrophischen Anteils der AMOC. Hierfür bestimme ich den geostrophischen Anteil der AMOC durch die Subtraktion des windgetriebenen Ekman Transports von der AMOC und durch die Berechnung des Transports aus der thermischen Windgleichung und den zonalen Dichtegradienten. Eine genauere Analyse der Variabilität der Dichtegradienten verdeutlicht die wichtige Rolle der westlichen Randdichten für die potentielle Vorhersagbarkeit der AMOC.

Die gemeinsame Analyse des MHT und der AMOC zeigt, dass nur die potentielle Vorhersagbarkeit der geostrophischen Anteile des MHT und der AMOC in direkter Verbindung zueinander stehen. Die Einzelanalysen legen bereits nahe, dass die potentiellen Vorhersagbarkeitsmuster der Umwälzkomponente des MHT und der AMOC in den subtropischen Breiten vergleichbare Strukturen aufweisen. Das noch

fehlende Verbindungsstück zwischen der potentiellen Vorhersagbarkeit des MHT und der AMOC wird jedoch erst deutlich, wenn man den Transport aus der thermischen Windgleichung der Umwälzkomponente des MHT abzüglich des Ekman Wärmetransports gegenüberstellt.

Die Ergebnisse dieser Doktorarbeit zeigen, dass die potentielle Vorhersagbarkeit des MHT und der AMOC weder untereinander austauschbar sind, noch von deren Analyse an einem einzelnen Breitengrad auf die Vorhersagbarkeit der gesamten Nordatlantikregion geschlossen werden kann.

CONTENTS

1. INTRODUCTION

1.1 Motivation

The oceans play an important role in predicting the climate on inter-annual to multi-decadal time scales, because of their large thermal and mechanical inertia resulting from the relatively high heat capacity and from the long time constants of the sub-surface and deep circulation (GARP, 1975). Variations in the Atlantic meridional overturning circulation (AMOC) and the associated meridional heat transport (MHT) are influenced by a combination of anthropogenic, natural, and internal forcings (Meehl et al., 2009). Multi-decadal variations of both quantities were shown to affect the North American and European climate (e.g., Sutton and Hudson, 2005; Pohlmann et al., 2006). The potential ability to predict the AMOC and the MHT on inter-annual to decadal time scales could therefore be of considerable benefit to policymakers and society. Additionally, understanding the oceanic predictability associated with physical processes that have long time scales or a periodic behavior could lead to an improved understanding of the entire climate system (Collins et al., 2006).

Several studies provide estimations of the AMOC's predictability at a single, mostly subtropical latitude in the North Atlantic (Keenlyside et al., 2008). For the MHT, to my knowledge, no published estimate of predictability exists, although or (probably) rather because the variability of the AMOC and the MHT are thought to be closely linked. While the AMOC is dominantly driven by wind stress and density gradients, the MHT is additionally driven by the air-sea fluxes that set the temperature distribution. Thus changes in MHT across different climates and different latitudes cannot exclusively be explained in terms of changes in the AMOC (cp. Ferrari and Ferreira, 2011). In my thesis, I therefore analyze the inter-annual to decadal predictability of the MHT and the AMOC and their relation with a particular focus on their latitude-dependence.

1.2 Predictability analyses

Actual predictions (forecasts) of climate relevant quantities on inter-annual to multi-decadal time scales are subjected to high uncertainty, due to the lack of observational data to fully initialize the forecasts and also due to the imperfectness of models. Before predictions on these times scales become useful to society at some time in the future, they will be highly experimental in the near future (Mehta et al., 2011). Retrospective predictability experiments are designed to improve the understanding of the behavior of individual climate relevant quantities or the interrelation between them under different experimental influences (e.g., changing initial or boundary conditions (future climate scenarios), or changing model formulations). Since these are experiments that can at best provide a certain kind of degree to which an actual prediction can be made, the term predictability needs to be clearly distinguished from the term prediction. To design a predictability experiment that resembles a realistic forecast scenario, considers the importance of the initial climate state, and provides adequate reference data, is a challenging task.

Predictability in the climate system is thought to arise in two distinct ways (Lorenz, 1975; Fig. 1.1): On the one hand, predictability can be determined by the errors deriving from poorly known initial conditions which amplify and spoil the simulations at some lead time (initial value problem). On the other hand, predictability can be determined by assessing a change in climate due to predictable changes in the external forcing (boundary value problem). Therefore, depending on the investigated time scales, the choice of initial and boundary conditions play a fundamental role in climate predictability studies.

Concerning the initial value problem, Latif et al. (2004) concluded, that the predictability, however, depends on the availability of the initial state. Collins et al. (2006) stated, that in any “real” world prediction system an estimate of the three-dimensional ocean state would have to be made using data assimilation. Nowadays, data assimilation products provide the most reliable estimates of the oceanic state by combining all available ocean data in a dynamical consistent way with a numerical model. Regardless of the initialization technique, several studies indicate that the predictive skill of an initialized system improves over predictions without knowledge of the ocean state (e.g., Troccoli and Palmer, 2007; Smith et al., 2007; Keenlyside et al., 2008; Pohlmann et al., 2009; Zhang, 2011; Matei et al., 2012b; Robson et al., 2012).

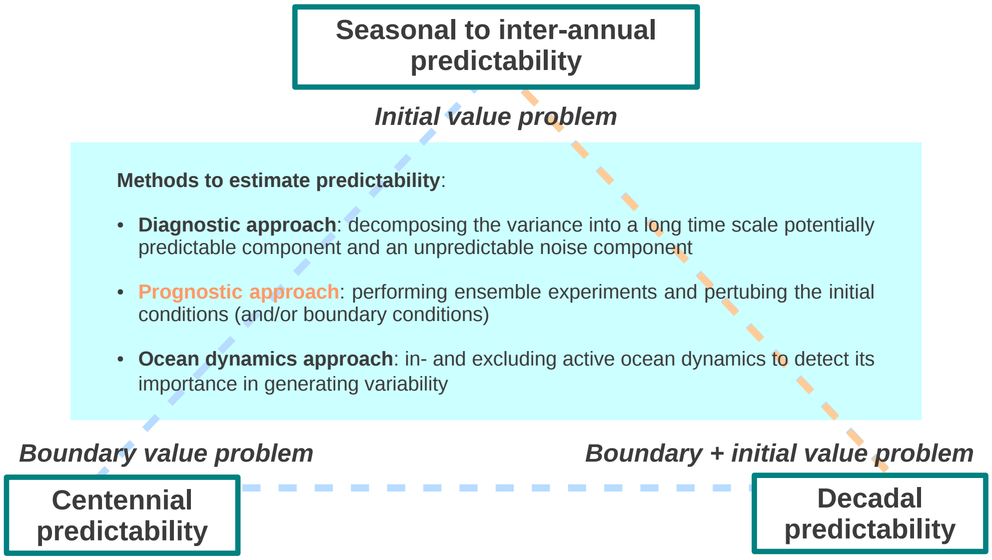

Methods to estimate predictability:

- **Diagnostic approach**: decomposing the variance into a long time scale potentially predictable component and an unpredictable noise component
- **Prognostic approach**: performing ensemble experiments and pertubing the initial conditions (and/or boundary conditions)
- **Ocean dynamics approach**: in- and excluding active ocean dynamics to detect its importance in generating variability

Fig. 1.1: Overview of the initial and boundary value problem in seasonal to multi-decadal predictability studies (adapted from T. Palmer (see for example http://www.wcc3.org/wcc3docs/pdf/PS3_palmer.pdf)), and methods used to study the problem. Orange color indicates where the present study can be located.

Generally, the approaches to estimate the predictability of a quantity on time scales ranging from a few seasons to a few centuries can be classified into three categories (Latif et al., 2006b; Fig. 1.1): The diagnostic approach, the ocean dynamics approach, and the prognostic approach. (i) In the diagnostic approach, the predictability is analyzed by decomposing the variance of a climate variable into a long time scale potentially predictable component and an unpredictable noise component (e.g., Pohlmann et al., 2004). (ii) In the ocean dynamics approach, the variability simulated with and without the inclusion of active ocean dynamics is analyzed to detect the regions where ocean dynamics are important in generating the variability (e.g., Park and Latif, 2004). (iii) The prognostic approach, consists of performing ensemble experiments and perturbing the initial or boundary conditions (e.g., Griffies and Bryan, 1997).

The prognostic predictability approach is also known as potential predictability approach, and it usually refers to ensemble experiments with perturbed initial conditions only. Thus, in a strict sense, potential predictability is defined as predictability assuming that the model being used is perfect and that the only source of error arises from uncertainties in the initial conditions (perfect model approach). In the present study, the term potential predictability is defined in a broader sense and refers to all kinds of predictability experiments that are verified against model simulations instead of observational data. Since oceanic observations are sparse in time and space, the validation against model simulations plays a special role when analyzing integrated quantities, such as the AMOC or the MHT, or quantities across several latitudes.

For the AMOC, several idealized predictability studies (e.g., Griffies and Bryan, 1997; Collins and Sinha, 2003; Pohlmann et al., 2004; Collins et al., 2006; Hermanson and Sutton, 2009; Msadek et al., 2010) and initialized predictability studies (e.g., Keenlyside et al., 2008; Pohlmann et al., 2009; Matei et al., 2012a; Kröger et al., 2012; Pohlmann et al., 2013) exist. The research interests range from the analysis of the interrelation of the AMOC with future climate scenarios (e.g., Keenlyside et al., 2008) to the assessment of actual predictive skill (Matei et al., 2012a), but no study with a dedicated focus on understanding the latitude-dependence of the AMOC's predictability exists. Except for the recent study of Kröger et al. (2012), who focused on the latitude-dependent impact of different data assimilation products on the decadal predictability, all studies investigated the predictability of the AMOC at a single latitude.

In addition to the variety of predictability approaches (e.g., diagnostic, prognostic, dynamic), the choice between an initialized or idealized experimental setup, and the considerable diversity of models (coupled or ocean-only), there is a variety of metrics to quantify predictability. Depending on the research question and the experimental setup, the quantification of the time period over which a certain quantity is potentially predictable (predictable lead time) is usually based on one or more of the following measures: The prognostic potential predictability (PPP; e.g., Collins and Allen, 2002; Msadek et al., 2010) indicating predictability by the relation of the ensemble spread and the variance of the reference simulation, the anomaly correlation (AC; e.g., Collins, 2002; Pohlmann et al., 2009) indicating predictability by the correlation of the ensemble mean to the reference simulation, or the root mean squared error (RMSE; e.g., Collins, 2002; Collins and Sinha, 2003) indicating predictability by the deviations of the hindcast simulation from the reference simulation. In most predictability studies one predictability metric is used, but also the usage of three metrics in one study can be found (e.g., Collins, 2002).

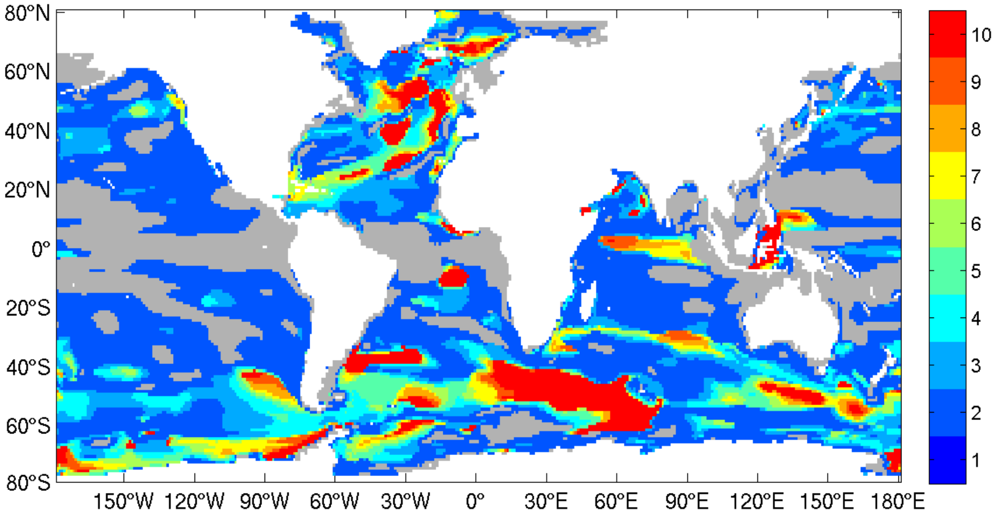

Fig. 1.2: Predictable lead times of the upper ocean heat content (0-~700m). The color scale ranges from dark blue, indicating a predictable lead time of 1 year, to red, indicating a minimum predictable lead time of 10 years. The predictable lead times are calculated based on the PPP metric and are significant at the 90% level.

1.3 Objectives of the Thesis

To analyze the latitude-dependent relation between the MHT's and AMOC's potential predictability on a multi-year time scale, I use a prognostic predictability approach. Retrospective ensembles (hindcasts) are generated in an ocean-only model by varying the initial and boundary conditions. The initial and boundary conditions are taken from a data assimilation product (GECCO[1]) which also serves as the reference run. Additionally, all simulations (reference run and hindcasts) and all data used to initialize and force these simulations were generated within the same data assimilation framework. While this limits the analysis to the "GECCO world", it also provides a self-consistent framework for the analysis. The predictable lead times are primarily quantified with the variance based PPP metric and later compared to the correlation based results of the AC metric.

As a first step, I present a global map indicating the predictable lead times of the upper ocean heat content (OHC) within my experimental setup (Fig. 1.2). Large regions in the North Atlantic Ocean and the Southern Ocean exceed predictable

---

[1] German partner of the consortium for Estimating the Circulation and Climate of the Ocean; Köhl and Stammer, 2008

lead times of 5 years, whereas other parts of the oceans show largely 1-2 years of predictable lead times or no significant potential predictability. These results are similar to previous studies of the OHC and the SST, particularly indicating the North Atlantic as a region where predictability may exist at inter-annual to multi-decadal time scales (e.g., Pohlmann et al., 2004; Matei et al., 2012b). For now, the main purpose of presenting a map of OHC predictability here, is to illustrate the global differences of the predictable lead times and in particular the differences between the subtropical and subpolar latitudes in the North Atlantic. These spatial differences in the OHC potential predictability give rise to the question of the dynamical origins and calls for a latitude-dependent potential predictability analyses of the meridional transports of mass and heat.

More specifically, I investigate three questions:

- Is the MHT potentially predictable? And if so, is the potential predictability of the MHT latitude-dependent?

- Can the current understanding of the latitude-dependent potential predictability of the AMOC be improved by removing the wind-driven variability and focusing on the latitude-dependence of the geostrophic part?

- And, as a consecutive question to the preceding ones: How is the potential predictability of the MHT related to the potential predictability of the AMOC?

1.4 Outline of the Thesis

This thesis is in its core a composite of one journal publication (chapter 2) and two chapters in preparation for submission to a journal (chapters 3 and 5). Two further chapters contain additional methodological background (chapter 4) and preliminary results as a starting point for future work (chapter 6). Particularly for chapters 2, 3 and 5, this structure implies some recurrences as each chapter has its own abstract, introduction and conclusion. The thesis is structured as follows:

Chapter 2 focuses on the latitude-dependent potential predictability of the MHT quantified with the PPP metric. The analysis of the potential predictability of the MHT's overturning and gyre component as well as the influence of the temperature and velocity field allows us to draw fundamental conclusions on the differences between the subpolar and subtropical latitudes in regard to potential predictability. This chapter has been published in *Journal of Climate*[2].

Chapter 3 focuses on the latitude-dependent potential predictability of the AMOC quantified with the PPP metric. The role of the geostrophic transport variability in the potential predictability of the AMOC is analyzed by comparing the PPP of the thermal wind transport calculated from boundary densities to the AMOC minus the Ekman transport. In order to identify the origins of the latitude-dependent potential predictability structure of the thermal wind transport, experiments are conducted to restrict the density variability to the eastern or western boundary. This chapter is in preparation for submission to *Climate Dynamics*[3].

Chapter 4 introduces the anomaly correlation as a second potential predictability measure. The potential predictability quantified with AC is tested for all quantities investigated in chapter 2, forming the starting point for the subsequent joint analysis of the AC and PPP in chapter 5.

Chapter 5 is a synthesis and extension of the results from the previous chapters with a dedicated focus on the relation between the AMOC and the MHT, using both the PPP and the AC as measures of potential predictability. This chapter is in preparation for submission to *Geophysical Research Letters*[4].

In chapter 6, I present preliminary results on the influence of the North Atlantic Oscillation (NAO) on the potential predictability of the MHT and the AMOC. Since the present ensemble setup is not ideally suited to analyze the influence of the NAO reasonably, I also suggest alternative setups for future work.

In chapter 7 overall conclusions are presented.

---

[2] Tiedje, B., Köhl, A., Baehr, J. (2012). Potential predictability of the North Atlantic heat transport based on an oceanic state estimate. *Journal of Climate*, 25(24): 8475-8486.

[3] Tiedje, B., Köhl, A., Baehr, J. (2012). North Atlantic thermal wind variability and its effects on potential predictability, in preparation.

[4] Tiedje, B., Köhl, A., Baehr, J. (2012). On the relation of the potential predictability of the AMOC and the MHT, in preparation.

2. POTENTIAL PREDICTABILITY OF THE NORTH ATLANTIC HEAT TRANSPORT BASED ON AN OCEANIC STATE ESTIMATE[1]

Abstract

This paper investigates the potential predictability of the meridional heat transport (MHT) in the North Atlantic on interannual time scales using hindcast ensembles based on an oceanic data assimilation product. The work analyzes the prognostic potential predictability (PPP), using the ocean synthesis of the German partner of the consortium for Estimating the Circulation and Climate of the Ocean (GECCO) as initial conditions and as boundary conditions. The PPP of the MHT varies with latitude: local maxima are apparent within the subpolar and the subtropical gyres, and a minimum is apparent at the boundary between the gyres. This PPP minimum can also be seen in the PPP structure of the Atlantic meridional overturning circulation (AMOC), although it is considerably less pronounced. The decomposition of the MHT shows that within the subpolar gyre, the gyre component of the MHT influences the PPP structure of the MHT. Within the subtropical gyre, the overturning component of the MHT characterizes the PPP structure of the MHT. At the boundary between the subpolar and the subtropical gyre, the dynamics of the Ekman heat transport limit the predictable lead times of the MHT. At most latitudes, variations in the velocity field control the PPP structure of the MHT. The PPP structure of the AMOC can also be classified into gyre and gyre boundary regimes, but the predictable lead times within the gyres are only similar to those of the overturning component of the MHT. Overall, the analysis provides a reference point for the latitude dependence of the MHT's PPP structure, and relates it to the latitude dependence of the AMOC's PPP structure.

---

[1] Tiedje, B., Köhl, A., Baehr, J. (2012). Potential predictability of the North Atlantic heat transport based on an oceanic state estimate. *Journal of Climate*, 25(24): 8475-8486.

2.1 Introduction

The transport of heat through the oceanic circulation has a profound influence on latitudinal variations in climate, since the ocean contributes to the time-mean meridional heat transport at approximately the same order of magnitude as the atmosphere (von der Haar and Oort, 1973). Fluctuations of the oceanic component of the meridional heat transport (MHT) originate from processes that are internal to the ocean, or in response to atmospheric fluctuations (Dong and Sutton, 2002). On short time scales, the variability of the MHT is dominated by Ekman processes. On interannual time scales, variability of the MHT arises primarily from the variability in the ocean circulation over most latitudes (Jayne and Marotzke, 2001; Dong and Sutton, 2002). More specifically, the variability of the velocity field acting on the time-mean temperature field is predominantly responsible for the MHT variability. The variability of the temperature field, i.e. temperature fluctuations advected by the time-mean velocity field, play a lesser role in the MHT variability. Jayne and Marotzke (2001) and Dong and Sutton (2002) both find that the influence of temperature variations increases at higher latitudes (i.e. the subpolar gyre), whereas Dong and Sutton (2002) also specify that the temperature variations particularly affect the decadal variability of the MHT at these latitudes.

At mid-latitudes, most of the MHT in the Atlantic is conducted through the Atlantic meridional overturning circulation (AMOC; Hall and Bryden, 1982), and repeated studies have shown that the fluctuations within both quantities are coherent (e.g., Pohlmann et al., 2006). Bingham et al. (2007) and Lozier et al. (2010) suggest that changes in the AMOC variability are latitude specific. At subpolar latitudes (north of 40°N), the AMOC variability has a strong decadal component, whereas at subtropical latitudes (south of 40°N), it is dominated by higher frequencies (Bingham et al., 2007). AMOC fluctuations on longer time scales than a decade are thought to be influenced by the North Atlantic Oscillation (NAO; e.g., Dong and Sutton, 2002; Eden and Willebrand, 2001).

The AMOC's latitude dependent variability is also thought to have an impact on its predictability at a specific latitude. AMOC predictability has mostly been studied in a perfect model framework (without direct comparison to observations) resulting in an estimate of potential predictability. The potential predictability of the AMOC has been analyzed at several individual latitudes (e.g., Collins and Sinha, 2003; Collins et al., 2006; Hermanson and Sutton, 2009; Pohlmann et al., 2009; Msadek et al., 2010), and recently also over a range of latitudes (Kröger et al., 2012). Although the variability of the AMOC and the MHT appear to be closely linked, the underlying mechanisms are not yet fully understood (e.g., Msadek et al., 2013). Further, different model formulations result in different AMOC states (Hurrell et al., 2010), and a long-term decrease in the AMOC's strength does not necessarily have to be followed by a decrease in MHT (Drijfhout and Hazeleger, 2006). Therefore, we focus here on the potential predictability of the MHT itself, rather than inferring the potential predictability of the MHT from the potential predictability of the AMOC. In the present study, we analyze the latitude dependencies of the potential predictability of the MHT, its components, and its relationship to the potential predictability of the AMOC on interannual time scales.

In order to analyze potential predictability on interannual time scales, both the initial and boundary conditions are important (Collins, 2002; Collins et al., 2006). Several studies indicate that on such time scales the predictive skill of an initialized system improves over predictions without knowledge of the ocean state (e.g., Troccoli and Palmer, 2007; Smith et al., 2007; Keenlyside et al., 2008; Pohlmann et al., 2009; Zhang, 2011). Further improvements are expected by using the same model environment to derive the initial conditions and the forecast simulations (e.g., Pohlmann et al., 2009). Here, we use the initial conditions from an oceanic state estimate and conduct hindcast simulations in the same model environment as that used to generate the state estimate.

We use the oceanic state estimate GECCO (German partner of the consortium for Estimating the Circulation and Climate of the Ocean; Köhl and Stammer, 2008). Since the GECCO state estimate is an ocean-only product, we use GECCO's past atmospheric forcing to force the hindcast simulations. The feedback from the atmosphere in such an ocean-only setup is missing, and thus we expect reduced predictive skill in comparison with a coupled climate model. However, since the forcing scenarios are prescribed and because they result from only a few decades, the full range of possible evolutions may not be explored. Nonetheless, the present study does benefit from the improved representation of oceanic variability in an oceanic state estimate. This is important, because such a dynamically consistent framework is crucial when studying an integrated quantity such as the MHT.

Ideally, hindcast predictions would be compared to the observational record over the hindcast period. In the ocean, however, and particularly for integrated quantities like the MHT and the AMOC, observations are limited both in time and space. At a specific latitude, the MHT and AMOC can be estimated from a zonal transect at the particular time of observation (e.g., Lumpkin and Speer, 2007). Recently, also time series of the MHT and the AMOC have become available at individual latitudes

(Cunningham et al., 2007; Willis, 2010; Johns et al., 2011; Hobbs and Willis, 2012). As the observations are too few to study the latitude dependent predictability of the MHT in the Atlantic, we investigate its *potential* predictability here by comparing hindcast ensembles initialized from an oceanic state estimate to the same oceanic state estimate.

2.2 Model and method

2.2.1 Model setup and reference run

We base our potential predictability analysis of the MHT on the currently available German-ECCO ocean synthesis. The ECCO framework aims to bring the global 1° MIT GCM (Massachusetts Institute of Technology general circulation model; Marshall et al., 1997) into agreement with as many observations as possible. Several ECCO products exist (http://www.ecco-group.org/products.htm) covering different periods from 1992 onwards, where GECCO provides an estimate of the oceanic state back to 1952. The currently available GECCO synthesis uses *in situ* and satellite observations that were collected over the period from 1952 through 2001 (Köhl and Stammer, 2008). During the optimization process, initial temperature and salinity conditions as well as time-dependent surface fluxes of momentum, heat and freshwater were adjusted by the adjoint method (Talagrand and Courtier, 1987).

Since the exact GECCO model setup used in Köhl and Stammer (2008) is no longer available due to technical problems, we have modified the optimized forcing of GECCO so that a very similar model setup produces similar results as the original GECCO output. The original GECCO forcing is corrected with the effect of SSS and SST relaxation to compensate for changes in the code. With this corrected optimized forcing, a 50-year integration is generated from 1952 to 2001 (covering the same period as the original GECCO run). This integration represents our reference run, though we focus on the period from 1959 to 2001 for our study.

2.2.2 Rationale of the experimental setup and ensemble generation

The reference run provides the initial conditions for the hindcast ensembles, which we construct to resemble a real forecast scenario such that no information is used in them that would not theoretically be available from observations at the time of ensemble generation. We initialize the ensembles from the second part of the reference

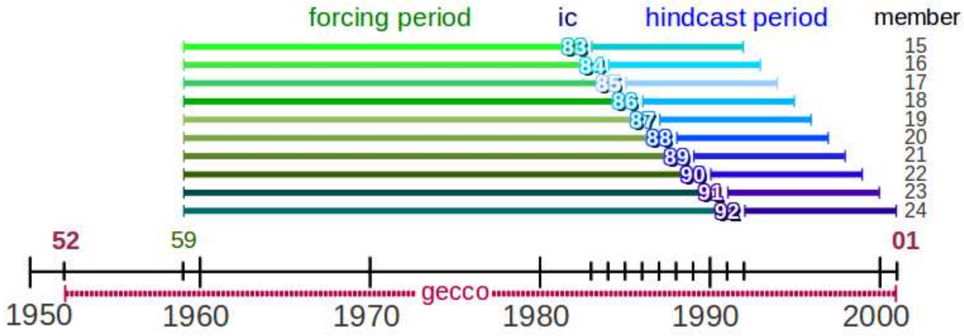

Fig. 2.1: Overview of the experimental setup: Above the time axis with the 50-year GECCO period (magenta), the forcing periods of the 10 hindcast ensembles are represented by the green lines, while the periods of the ensembles are represented by the blue lines. In addition, the start dates (years providing the initial conditions (ic)) and the number of ensemble members are shown.

run and force those ensembles with the optimized forcing from the first part of the reference run. This allows us to leave the option open to apply different methods to quantify predictability in the setup. We focus on the later part of the reference run when initializing the hindcast ensembles, since considerably more observations were available to constrain the GECCO state estimate during that period. By using the forcing from the earlier part of the reference run, we make the assumption that the forcing of the last decades is not significantly different from the future decades.

We initialize 10 ensembles from the reference run starting one year apart (1983, ..., 1992) to ensure continuous sampling of the initial conditions. In each ensemble, the ensemble members are generated using different 10-year periods from the corrected optimized atmospheric forcing. These 10-year forcing periods start one year apart (1959, ..., 1983) and end on the date of the initial conditions (1983, ..., 1992). This setup results in 15 to 24 members per ensemble with a simulation period of 10 years each (Fig. 2.1). The monthly mean model output is averaged to annual means for the potential predictability analysis.

The spreads of the ensembles and their latitudinal variations are similar amongst different ensembles. The small differences present are mostly due to varying initial conditions, though they are to some small extent also due to the number of forcing

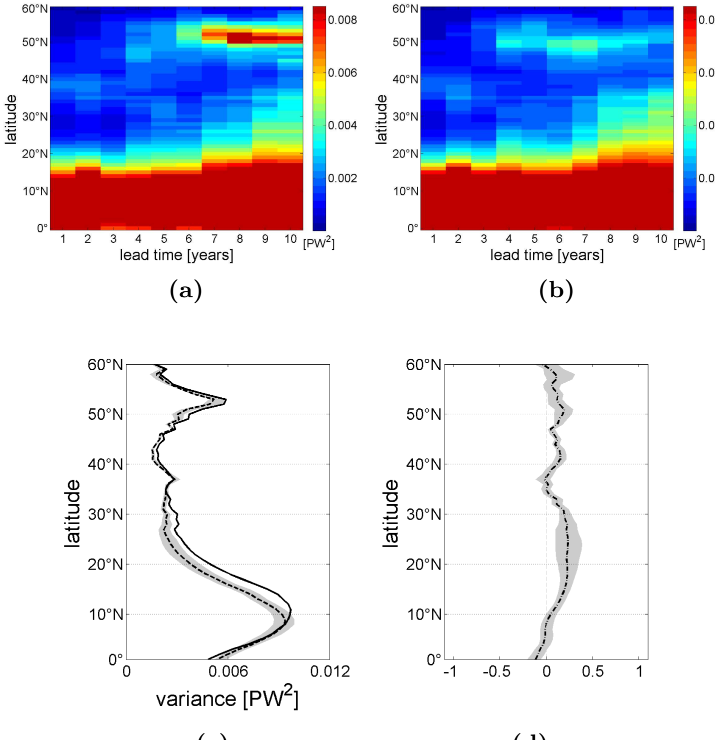

(a) (b)

(c) (d)

Fig. 2.2: MHT ensemble spread and MHT reference variance (Atlantic: 0° - 60°N): (a) and (b) Hovmöller diagrams of the ensemble spread for the ensembles initialized in 1986 and 1991. (c) Variance of the detrended reference run from 1959 to 2001 (solid line) and mean variances over the individual forcing periods of the detrended reference run (dashed line; gray shading indicates the range of individual forcing variances). The individual forcing periods cover the periods from 1959 to the individual initial conditions of the ensembles (1959 to 1983,...,1992). (d) The ratio of the dashed line and the solid line in (c) is subtracted from 1 to illustrate the potential predictability that is inherent in the experimental setup or the system itself (gray shading indicates the range of individual variances).

periods, or respectively to additional ensemble members. To illustrate the latitudinal variations of the ensemble spreads, we arbitrarily select two MHT ensembles (starting in 1986 and 1991; Fig. 2.2a and Fig. 2.2b). In both ensembles, we find increased spread between ∼0° and ∼20°N, and ∼50°N and ∼60°N, which is also visible in the averaged variances for the forcing periods (1959 to 1983, ..., 1992) of the reference run (Fig. 2.2c). The variances of the reference run are also similar over the forcing periods and the (entire) reference period (1959 to 2001). We show the variances and spreads for the MHT here as an example, but the above-mentioned statements apply to all investigated quantities.

2.2.3 Potential predictability method

We estimate potential predictability by calculating the prognostic potential predictability (PPP; Pohlmann et al., 2004). The PPP of a quantity is determined using the ratio of the ensemble spread as a function of time to the variance of a reference simulation:

$$PPP(t) = 1 - \frac{\frac{1}{N}\sum_{j=1}^{N}\frac{1}{(M-1)}\sum_{i=1}^{M}(X_{ij}(t) - \bar{X}_j(t))^2}{\sigma^2} \tag{2.1}$$

where X_{ij} is the i*th* member of the j*th* ensemble, $\bar{X}(t)$ is the ensemble mean, M is the number of ensemble members (here, M ranges between 15 and 24), and N is the number of ensembles (here, N=10). σ^2 represents the variance of a reference simulation, for which we use the reference run from 1959 to 2001. Note that the subtraction of the ensemble mean (as a function of time) effectively detrends the hindcasts in computing $PPP(t)$. To avoid artificial predictability we detrend the reference run by removing the best straight-line fit from the monthly mean model output at every latitude before averaging to annual means. Turning to the results for $PPP(t)$, a value of 1 indicates perfect potential predictability, whereas a value below 0 indicates no potential predictability.

In order to test whether there is any predictability inherent to the experimental setup, we first conducted a short predictability analysis similar in procedure to that described above, but which uses only the reference run. As the spread of the ensembles generally represent the variances of the forcing periods (Fig. 2.2a-c), we calculate 1 minus the ratio between the variances of the forcing periods and the reference period (Fig. 2.2d). The resulting values are quite small (<0.4), and are concentrated around 0, indicating that there is little to no predictability resulting from the experimental setup itself.

The significance of PPP is estimated using an F-test. Following Pohlmann et al. (2004), we denote a quantity as being potentially predictable as long as its PPP is greater than the critical significance limit:

$$PPP > 1 - 1/F_{\sum(M-1),dof}. \tag{2.2}$$

Since the forcing periods overlap, the ensemble members are not strictly independent. For the sake of simplicity, we assume the ensembles' degrees of freedom (dof)

are the total sum of the varying number of ensemble members minus 1 ($\sum(M-1)$). Varying the degrees of freedom of the ensemble does not significantly change the resulting critical significance limit. The degrees of freedom for the reference run are calculated from the decorrelation time of the first-order autoregressive process (e.g., von Storch and Zwiers, 1999):

$$dof = (n/\frac{1+\alpha}{1-\alpha}) - 1, \tag{2.3}$$

where n denotes the sample size of the reference period and α denotes its lag-1 autocorrelation coefficient. For all investigated quantities the critical significance limit varies with latitude. Since the variations are small, however, we take the average of the critical significance limit over the latitudes, preserving the latitude dependence of the the respective quantity's PPP. In the following, *PPP structure* stands for the spatial and temporal extent of the significant PPP values across the North Atlantic, and *predictable lead time* stands for the time period over which the PPP values are significant.

2.3 Results

2.3.1 Potential predictability of the total MHT

We find that the MHT is potentially predictable within the subtropical gyre (~15°N to ~35°N) and within the subpolar gyre (~45°N to ~60°N) with a gap around 40°N at the boundary between the gyres (Fig. 2.3). At subtropical latitudes, we find predictable lead times of 3 to 4 years. At subpolar latitudes, we find slightly higher PPP values than at subtropical latitudes and predictable lead times of 3 to 5 years.

To facilitate a better understanding of the predictable lead times of the MHT, we decompose the heat transport into three dynamic components (following Bryden and Imawaki, 2001): the barotropic component, the overturning component, and the gyre component. The three components are calculated as follows:

$$\begin{aligned} H(y) &= \rho c_p \int_0^D \int_0^L \langle v \rangle (y) \langle \theta \rangle (y) dxdz + \\ & \rho c_p \int_0^D \int_0^L [v](y,z)[\theta](y,z) dxdz + \\ & \rho c_p \int_0^D \int_0^L v'(x,y,z)\theta'(x,y,z) dxdz, \end{aligned} \tag{2.4}$$

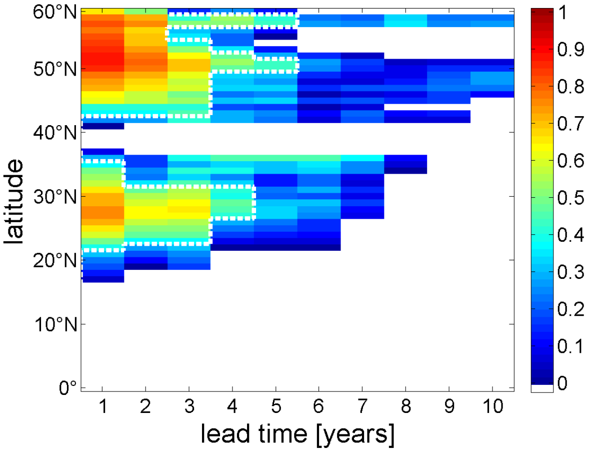

Fig. 2.3: Hovmöller diagram of the prognostic potential predictability (PPP) of the MHT as a function of lead time (Atlantic: 0° - 60°N). The white dashed line indicates values significant at the 90% level.

where v and θ denote the meridional velocity and the potential temperature. ρ is defined as the reference density and c_p the heat capacity per unit mass of water at constant pressure. D and L represent the depth and the width of the zonal transoceanic section. The angle brackets ($\langle\rangle$) denote the section average, the square brackets ($[]$) denote the zonal average minus the section average, and the primes ($'$) denote the deviations from the respective zonal average. Hence, the first term is the net transport across the section at the section-averaged temperature. The second term represents the contribution of the zonally-averaged meridional circulation, and the third term is the contribution of the large-scale gyre circulation. The decomposition of the MHT is calculated for monthly mean model data, while for the following analysis annually averaged values are used (cp. chapter 2.2).

Consistent with other modelling studies (e.g., Dong and Sutton, 2002), the barotropic component appears to be negligible, and the total MHT is dominated by the overturning component, apart from the subpolar latitudes (Fig. 2.4a). At the latter latitudes, the influence of the gyre component on the total MHT exceeds the influence of the overturning component, since the zonal temperature difference is as large as the vertical temperature difference. The spatial divide between the influence of the gyre and the overturning component on the total MHT becomes more clear in the variances (Fig. 2.4b). South of ∼45°N most of the total variance of the MHT can be explained by the high variance of the overturning component. Yet, the increased variance at subpolar latitudes is only evident in the gyre component.

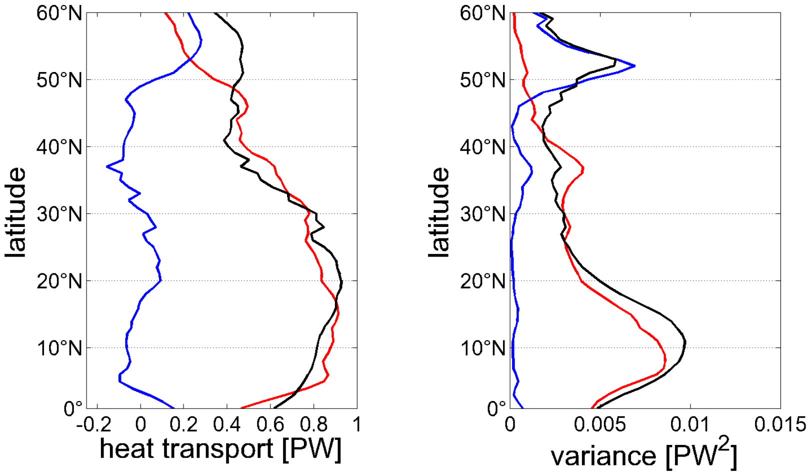

(a) (b)

Fig. 2.4: Total MHT and its components of the detrended reference run from 1959 to 2001: (a) Time mean values, and (b) variances of the total MHT (black), the overturning component (red), and the gyre component (blue) (Atlantic: 0° - 60°N).

2.3.2 Potential predictability of the MHT components

At subtropical latitudes, the predictable lead times of the overturning component indicate about 6 years of potential predictability (Fig. 2.5a). At subpolar latitudes, the predictable lead times indicate about 2 years of potential predictability. Around 40°N, we find a gap between the subpolar and subtropical gyre, just as exists in the total MHT's PPP structure (Fig. 2.3). Compared to the PPP structure of the total MHT, the overturning component shows longer predictable lead times at the subtropical latitudes, which also extend over a larger range of latitudes, and at subpolar latitudes slightly shorter predictable lead times and lower PPP values.

To analyze the overturning component's influence on the predictable lead times of the total MHT, we replace σ^2 in equation (2.1). That is, we divide the spread of the overturning component by the variance of the total MHT, instead of the variance of the overturning component. For latitudes south of ∼40°N, the resulting PPP structure is similar to the PPP structure of the overturning component (Fig. 2.5a compared to Fig. 2.5b). For latitudes north of ∼40°N, the resulting predictable lead times are considerably longer than the predictable lead times using the variance of the overturning component. These high values imply that predictable lead times of the total MHT are not limited by the influence of the overturning component at latitudes north of ∼40°N.

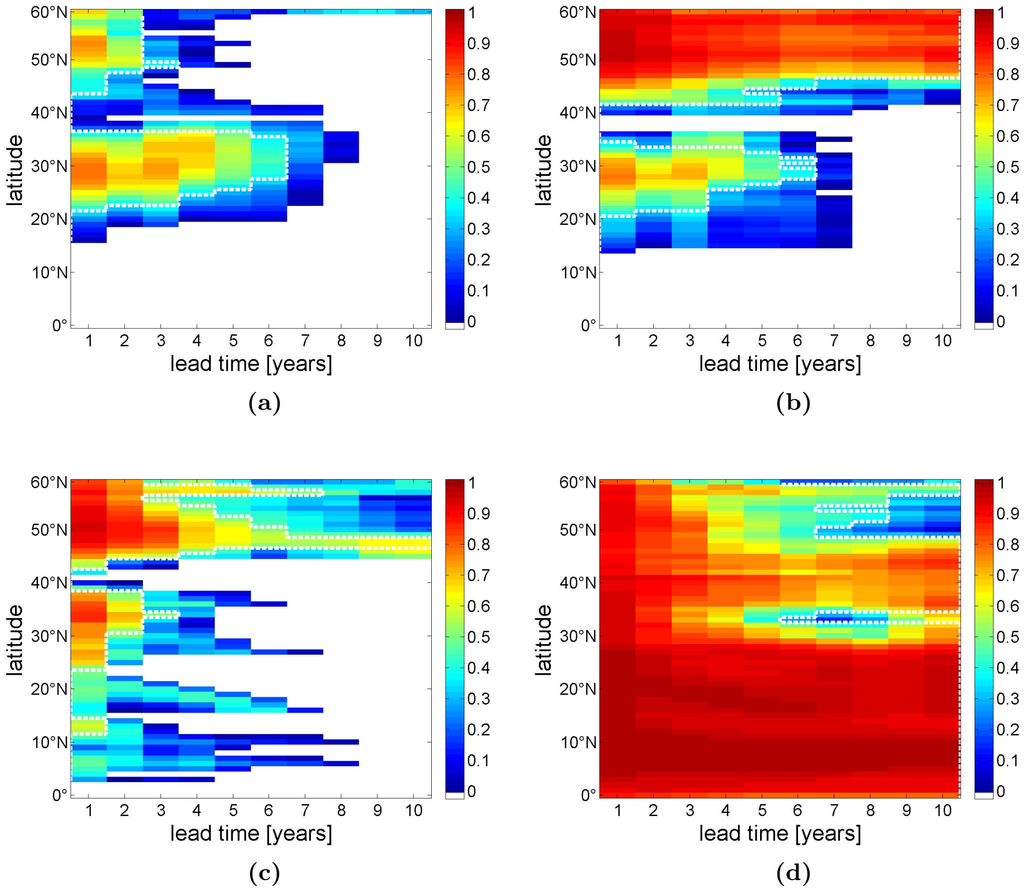

(a)

(b)

(c)

(d)

Fig. 2.5: Hovmöller diagrams of the PPP as a function of lead time (Atlantic: 0° - 60°N) for (a) the overturning component of the MHT, and (b) the overturning component of the MHT, where the ensemble spread is divided by the reference variance of the total MHT (instead of the reference variance of the overturning component). In (c) and (d) the same measures are presented as in (a) respectively (b), but for the gyre component of the MHT. The white dashed lines indicate values significant at the 90% level.

The predictable lead times of the gyre component indicate potential predictability of 5 to 10 years at subpolar latitudes (Fig. 2.5c). Between ∼30°N and ∼40°N, we find predictable lead times of about 2 years. South of ∼30°N, essentially no potential predictability is evident. Apart from the decrease of potential predictability at the gyre boundary and the higher PPP values at subpolar than at subtropical latitudes, the PPP structure of the gyre component shows no similarities to the PPP structure of the total MHT (Fig. 2.3).

As in the analysis of the overturning component, we divide the spread of the gyre component by the variance of the total MHT, instead of the variance of the gyre component in the PPP calculation. This analysis shows that the spread of the gyre component is large enough to influence the predictable lead times at the subpolar latitudes and between ∼30°N and ∼40°N (Fig. 2.5d). At the subpolar latitudes, this indicates that the predictable lead times of the total MHT are more heavily influenced by the spread of the gyre component than by the spread of the overturning component (Fig. 2.5b). Although we find longer predictable lead times for the gyre component (Fig. 2.5c) than for the total MHT (Fig. 2.3) at these latitudes, the influence of the gyre component can be seen in the enhanced potential predictability of the total MHT compared to the potential predictability of the overturning component. Between ∼30°N and ∼40°N the influence of the gyre component can be seen in shorter (and spatially less extended) predictable lead times of the total MHT compared to predictable lead times of the overturning component. Overall, the PPP structure of the total MHT (Fig. 2.3) can be reconstructed from the analysis of the overturning and gyre component's PPP structures (Fig. 2.5a and c) together with the relative influence of the component spreads on the total MHT (Fig. 2.5b and d).

2.3.3 Influence of velocity and temperature field variations

Jayne and Marotzke (2001) and Dong and Sutton (2002) have shown that the influence of the variability of the velocity field on the variability of the MHT clearly dominates over the variability of the temperature field, with the exception of the higher latitudes where temperature variations gain influence. To estimate the influence of the velocity (temperature) variations on the variability of the MHT, we calculate the MHT with a time mean temperature (velocity) field in the reference run from 1959 to 2001. South of ∼30°N the variance of the reference MHT is controlled by the variations in the velocity field (Fig. 2.6a). North of ∼30°N, the variance of the total MHT and the variance of the MHT with a constant velocity field show significantly smaller values than the variance of the MHT with a constant temperature field. Hence, we suggest that north of ∼30°N temperature field variations covary with velocity field variations, such that the net MHT variability remains relatively low.

We now turn to the assessment of whether this spatial separation, between the influence of the velocity field and the influence of the temperature field on the variability of the MHT, is also visible in the potential predictability of the MHT. To estimate the influence of the velocity (temperature) variations on the potential predictability of the MHT, we calculate the MHT of each ensemble member with a constant temperature (velocity) field (time mean of the respective ensemble member), but in the reference run we keep the full signal of the temperature (velocity) field.

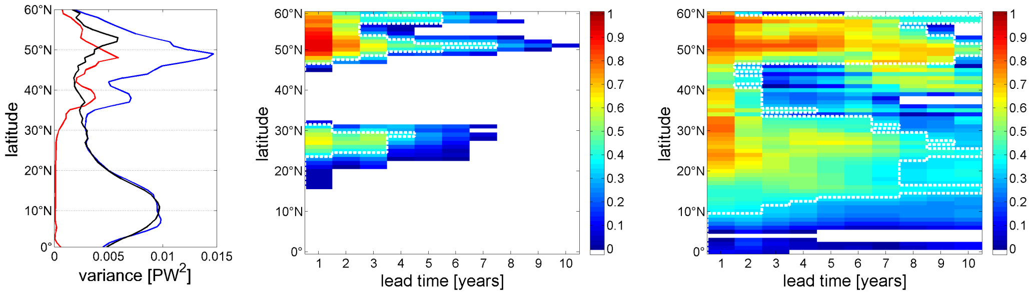

(a) **(b)** **(c)**

Fig. 2.6: MHT calculated with a constant mean temperature or velocity field (Atlantic: 0° - 60°N): (a) Detrended reference run: Variances of the total MHT (black), the MHT calculated with a constant mean temperature field (blue), and the MHT calculated with a constant mean velocity field (red) from 1959 to 2001. (b) and (c): Hovmöller diagrams of the PPP as a function of lead time for the MHT calculated with a constant mean temperature field for the ensembles (b), and the MHT calculated with a constant mean velocity field for the ensembles (c). The white dashed lines indicate values significant at the 90% level.

The PPP structure of the MHT using a constant temperature field and a varying velocity field (Fig. 2.6b) is in general similar to the PPP structure of the total MHT with both fields varying (Fig. 2.3). The PPP structure in both gyres is narrower for the MHT using a constant temperature field and a varying velocity field than for the total MHT with both fields varying, resulting in a wider band in which potential predictability is non-existent (∼35°N to ∼45°N).

At every latitude, the predictable lead times of the MHT using a constant velocity field and a varying temperature field are longer than the predictable lead times of the total MHT with both fields varying (Fig. 2.6c). This shows that the spread created by the temperature field variations alone is too small to restrict the potential predictability to resemble the PPP structure of the MHT with both fields varying (Fig. 2.3).

At most latitudes, the variations of the velocity field are more important than the variations of the temperature field for the PPP structure of the total MHT, except for the latitudes in the vicinity of the gyre boundary (∼30°N - 35°N and ∼40°N - 45°N). At these latitudes the velocity field variations alone are too large to represent the PPP structure of the total MHT. North of ∼30°N the influence of the temperature field variations on the total MHT variance increases (Fig. 2.6a). In the PPP structure, this increased influence becomes obvious in the vicinity of the gyre boundary, where temperature field variations reduce the total ensemble spread and lengthen the predictable time scales of the total MHT to narrow the boundary gap.

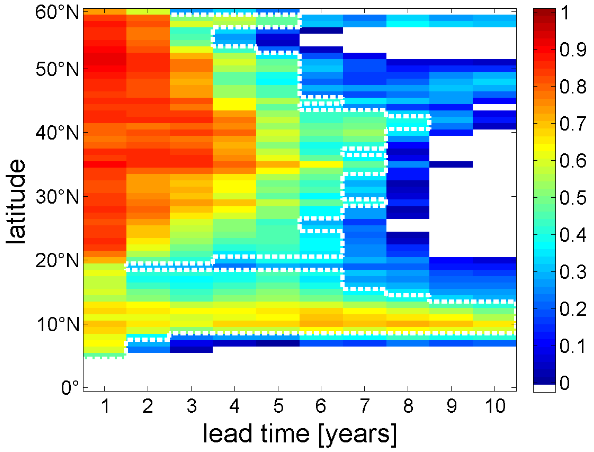

Fig. 2.7: Hovmöller diagram of the PPP of the MHT minus the Ekman heat transport, with the ensemble spread divided by the reference variance of the total MHT, as a function of lead time (Atlantic: 0° - 60°N). The white dashed line indicates values significant at the 90% level.

2.3.4 Influence of the Ekman heat transport

Ekman dynamics contribute significantly to the MHT variability on interannual time scales (Jayne and Marotzke, 2001; Dong and Sutton, 2002). To analyze the influence of the atmospheric wind field on the predictable lead times of the MHT, we now subtract the Ekman heat transport from the total MHT prior to the PPP analysis. Across a zonal section, the Ekman heat transport is defined as the integral of the meridional Ekman-layer mass flux, multiplied by the difference between the Ekman layer temperature T_{Ek} and the section-averaged potential temperature $\langle[\theta]\rangle$ (Jayne and Marotzke, 2001). This assumes that, for any given section, the mass transport in the Ekman layer is compensated by a section and depth uniform return flow, and thus the Ekman heat transport can be calculated as follows:

$$H_{Ek} = -\int \rho c_p \frac{\tau_x}{f\rho}(T_{Ek} - \langle[\theta]\rangle)dx, \tag{2.5}$$

where f is the Coriolis parameter, ρ is the reference density, and τ_x is the zonal wind stress. Here, we define T_{Ek} as the sea surface temperature since the actual depth of T_{Ek} appears to be insignificant.

To test the influence of the Ekman heat transport on the potential predictability of the MHT, we calculate the MHT minus the Ekman heat transport for the ensembles, but we keep the full MHT signal in the reference run for the PPP analysis (Fig. 2.7). The resulting predictable lead times are longer than the predictable lead times of the total MHT at all latitudes (Fig. 2.3). Within the gyres, the influence of the Ekman heat transport on the predictable lead times is not as strong, though it appears stronger at subtropical latitudes than at subpolar latitudes. Particularly at the gyre boundary and at the southern boundary of the subtropical gyre (between ∼5°N and ∼20°N), the influence of the Ekman heat transport variability is so strong that it prevents potential predictability of the total MHT at these latitudes entirely.

2.3.5 Potential predictability of the AMOC

Having analyzed the PPP structure of the total MHT, we now turn to the question of whether the predictable lead times of the total MHT are directly related to the predictable lead times of the AMOC. The predictable lead times of the AMOC increase continuously from 2 years in the supolar gyre to about 6-7 years in the subtropical gyre (Fig. 2.8). Especially for lead times of 1 year, the PPP values are higher in the gyres than at the boundary. Although there is no gap of potential predictability at the boundary between the subpolar and subtropical gyre, we can still distinguish between the gyres and the gyre boundary.

The PPP structures of the AMOC and the total MHT (Fig. 2.3) are generally different. The predictable lead times of the AMOC are longer at subtropical latitudes than at subpolar latitudes, as seen in the overturning component of the MHT (Fig. 2.5a), but not the MHT as a whole. The potential predictability of the AMOC is slightly shorter than the MHT's at subpolar latitudes. At these latitudes MHT's PPP structure is influenced by an increased contribution from the gyre component, induced by changes in the temperature field distribution (cp. chapters 2.3.1 and 2.3.2).

At the gyre boundary, the influence of the Ekman variability on MHT's PPP is so strong that it prevents any potential predictability, while the influence of the Ekman variability on the AMOC PPP merely decreases the PPP values, but the predictability lead times are nearly as long as in the subtropical gyre. Thus, Ekman variability appears to play a more important role in determining the potential predictability of the MHT than it does in determining that of the AMOC, since most of the heat transport occurs in the upper layers of the ocean.

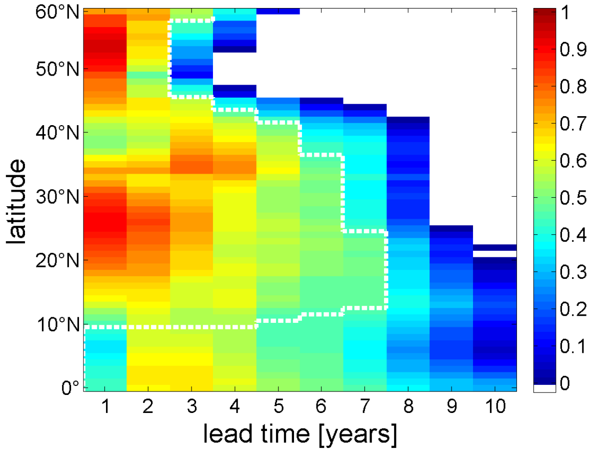

Fig. 2.8: Hovmöller diagram of the PPP of the MOC (at ∼1000m) as a function of lead time (Atlantic: 0° - 60°N). The white dashed line indicates values significant at the 90% level.

2.4 Discussion

The PPP of the total MHT is different in the subtropical gyre, the subpolar gyre, and the area forming the boundary between the gyres. Though a gyre dependence of the potential predictability can also be seen for the AMOC, its PPP structure is only similar to the overturning component of the MHT.

For the AMOC, our predictable lead times fall within the wide range of previous findings. This wide range is due to a considerable diversity in the models employed, their setups and the variety of initial conditions, as well as the applied methods used to quantify predictability: The AMOC's (potential) predictability lead times range from 3-6 years (Hermanson and Sutton, 2009; Pohlmann et al., 2009; Matei et al., 2012a; Kröger et al., 2012; Pohlmann et al., 2013) to a decade or even longer (Griffies and Bryan, 1997; Collins and Sinha, 2003; Pohlmann et al., 2004; Collins et al., 2006; Keenlyside et al., 2008; Msadek et al., 2010). With the exception of Kröger et al. (2012), these AMOC (potential) predictability studies were conducted at a single (mostly subtropical) latitude or a basin-wide maximum AMOC index, and not over a range of latitudes across the North Atlantic.

In contrast to the diverse findings for the AMOC's potential predictability time scales, there are to the authors' best knowledge no published studies on the potential predictability of the MHT. Particularly the minimum in the MHT's potential predictability at the gyre boundary is a surprising result. However, an indication of latitudinal variations in the potential predictability, and an area of decreased potential predictability at mid-latitudes in the North Atlantic can also be seen in previous predictability studies on the SST (Pohlmann et al., 2004; Boer, 2009; Matei et al., 2012b), the upper ocean heat content (Matei et al., 2012b), and the AMOC (Kröger et al., 2012). Since no estimate thus far exist for the MHT's predictable lead time, our results serve as a reference point for the discussion of meridional variability in MHT PPP structures, and their relation to AMOC PPP structures.

Our PPP structures of the AMOC and the overturning component of the MHT contradict the widely accepted view that the AMOC's potential predictability is higher at subpolar latitudes than at subtropical latitudes. This view is based on the close relationship between the potential predictability of the thermohaline circulation and the North Atlantic SST (e.g., Pohlmann et al., 2004; Latif et al., 2004), and the notion that SST anomalies are more predictable in the subpolar than in the subtropical North Atlantic (e.g., Msadek et al., 2010). Pohlmann et al. (2009) anticipated that the AMOC's predictive skill might be limited to high latitudes due to the close connection between the NAO and the AMOC strength. On the other hand, propagating AMOC signals (e.g., Köhl and Stammer, 2008; Getzlaff et al., 2005) could also provide longer predictable time scales in the subtropics. While we maintain that the gyre dependence of the PPP is a robust result, our analysis cannot fully explain why the predictable lead times are shorter or longer at specific latitudes within our analysis. Thus, the actual distribution of the predictable lead time lengths remains a matter of discussion and should be subjected to further investigation.

Limitations of our analysis primarily arise from the setup employed. For example, hindcast ensembles are not generated in a coupled model but rather by using predefined atmospheric forcing (historical forcings from 1959 to 1992). Assuming that the forcing in the next decade is not unlike the forcing in previous decades, the present results cover a range of expected forcings. The forcing comes from both NAO^+ and NAO^- periods, but the initial conditions are restricted to mostly NAO^+ states. This is a consequence of limiting the initialization of the ocean to the last two decades of the GECCO state estimate, which is done to ensure the use of independent forcing data from the previous decades. Unfortunately, the present setup does not allow us to clearly distinguish between different NAO states in order to analyze the sensitivity of potential predictability within the context of the NAO's state of the initial and boundary conditions. Since changes in the NAO are thought to influence the time scales of AMOC variability at subpolar latitudes (Eden and Willebrand, 2001; Lozier et al., 2010), and GECCO furthermore shows an AMOC that is sensitive to the state of the NAO (Köhl and Stammer, 2008), an influence by these conditions on our results cannot be excluded.

The actual lengths of the calculated predictable time scales depend on a number of parameters selected in the analysis to derive the predictable lead times (chapter 2.2.3). For example, using a different reference period (e.g., the forcing or the hindcast period), or not detrending the reference run could increase or decrease the predictable lead times by a couple of years. Another example is the parameters entering the calculation of the significance level, and the actual method chosen to calculate the significance level. None of the choices change the general latitudinal PPP structure for the analyzed quantities. We therefore refrain from insisting on a specific number of predictable years at a certain latitude, but emphasize the relation of potential predictability between different latitudes.

While we cannot initialize the atmosphere, our setup represents a self-consistent framework with respect to both initialization and consistency with observations. Previous studies have shown that the initialization procedure can impact resulting predictions, as is visible in the comparison between the SST predictions of Keenlyside et al. (2008) and Pohlmann et al. (2009), who use the same model but a different initialization method. The model formulation also has a considerable impact on the model state (see, e.g., the AMOC in Hurrell et al. (2010)). Here, we use the same model framework for the synthesis with the observations, the hindcast simulations, and the verification of the ensemble spread. Further studies using initialized hindcast ensembles from coupled models, and potentially also verifying the ensemble spread against observations are therefore essential in establishing the robustness of the conclusions.

We have restricted the current analysis to potential predictability as it is currently not possible to analyze the latitude dependence of the MHT and the AMOC against real observations. But the present experimental setup allows us to evaluate possible oceanic states (ensemble hindcasts) against an oceanic state estimate instead. In the present study we evaluate the theoretical limit of the predictable lead times by means of the PPP method, but the yearly start dates of the initial conditions (to continuously sample variability) together with the independent hindcast reference periods also allow us to quantify the potential predictability by means of the anomaly correlation (following Pohlmann et al., 2009). Given the different informative value of both methods, it is not a trivial result that the general conclusions of the PPP analysis can be confirmed with the anomaly correlation. In the chosen model environment, regardless of the chosen method, our conclusions represent an indication of latitude-dependent potential predictability of both the MHT and the

AMOC, which are in agreement with previous studies of both the variances of the MHT and the AMOC (Jayne and Marotzke, 2001; Lozier et al., 2010).

2.5 Conclusions

Based on our analysis of the prognostic potential predictability (PPP) of the MHT in the North Atlantic in hindcast ensembles initialized from the GECCO oceanic state estimate, we conclude that:

- The PPP of the MHT varies with latitude, changing between the subtropical and subpolar gyre, and at the gyre boundary.
- Within the subtropical gyre, the PPP structure of the MHT is characterized by the overturning component. Within the subpolar gyre, the PPP structure of the MHT is characterized by the gyre component.
- At most latitudes, variations in the velocity field play a determining role on the PPP structure of the MHT. The influence of temperature field variations on the PPP structure of the MHT can so far only be confirmed in the vicinity of the gyre boundary.
- On the investigated interannual time scales, Ekman dynamics influence the PPP structure of the MHT at all latitudes, and limit the predictable lead times of the MHT particularly at the gyre boundary and at the southern extent of the subtropical gyre.
- We confirm earlier results that the PPP of the AMOC varies with latitude. Here, we find that Ekman dynamics decrease the PPP of the AMOC at the gyre boundary, though in contrast to the MHT, no distinctive minimum is apparent at the gyre boundary.
- The PPP structure of the AMOC cannot be directly related to the PPP structure of the MHT. But the predictable lead times of the AMOC are similar to the predictable lead times of the MHT's overturning component.
- The suggested gyre-dependent predictable lead times of both MHT and AMOC indicate that caution should be exercised when interpreting the potential predictability of the MHT or AMOC at a single latitude.

Acknowledgments This study is supported through the Cluster of Excellence 'CliSAP' (EXC177), University of Hamburg, funded through the German Science Foundation (DFG). We thank Daniela

Matei for discussion. Robert Piontek, Sebastian Brune, and the two reviewers provided valuable comments which considerably improved the manuscript.

3. NORTH ATLANTIC THERMAL WIND VARIABILITY AND ITS EFFECTS ON POTENTIAL PREDICTABILITY[1]

Abstract
We investigate the influence of boundary density variability on the potential predictability of the North Atlantic meridional overturning circulation (AMOC) by analyzing the potential predictability of the thermal wind transport. The potential predictability on inter-annual time scales is assessed by using hindcast ensembles based on an oceanic data assimilation product. The potential predictability of the thermal wind transport is latitude-dependent and shows a maximum of predictability lead times around 40°N and decreasing potential predictability to the north and south. To understand the roles of the eastern and western density boundary variability we conduct experiments by holding the density boundary values temporally constant at one side of the basin, while keeping the full signal at the other side prior to the potential predictability analysis. These experiments suggest that the variability of the upper western boundary densities is sufficient to reconstruct most of the latitudinal variations of the potential predictability of the total thermal wind transport. In contrast, the influence of the lower western boundary densities and the eastern boundary densities on the potential predictability of the total thermal wind transport is small. Although we find similarities, the potential predictability of the AMOC cannot be directly concluded from the potential predictability of the thermal wind transport without considering the regional influence of the Ekman transport. However, the findings open the prospect to use density boundary values in combination with wind field data for estimating the potential predictability of the AMOC, and underline the importance to maintain and extend the current observing system in the North Atlantic.

---

[1] Chapter 3 is in preparation for submission to *Climate Dynamics*.

3.1 Introduction

The AMOC is composed of a dominant buoyancy-driven part and a wind-driven part. More specifically, it can (theoretically) be reconstructed from the contributions related to the barotropic (depth-averaged) velocities, to the geostrophic shear and to the Ekman transports (Lee and Marotzke, 1998). In order to design a monitoring system for the AMOC, numerical models were used to test whether the AMOC can be reconstructed from boundary densities and the zonal wind stress alone (e.g., Hirschi et al., 2003; Baehr et al., 2004). These studies laid the ground for the implementation of the RAPID/MOCHA array at 26.5°N (Kanzow et al., 2007; Cunningham et al., 2007).

Since AMOC estimates at a single latitude do not allow for immediate conclusions about adjacent latitudes (Baehr, 2010), model studies are still needed to facilitate a better understanding of the contributions of the boundary densities and the wind stress to the basin-scale variability of the AMOC. For example, Hirschi and Marotzke (2007) showed in a model study that the leading modes of the temporal and spatial AMOC variability can be reproduced with the boundary densities and the zonal wind stress. Primarily, the inter-annual AMOC variability can largely be captured from changes in the boundary densities, and plans are underway to extent the continuous AMOC monitoring to other latitudes in the North Atlantic (Cunningham et al., 2010).

Despite of the variety of studies decomposing the AMOC at one or more latitudes, no previous study has concentrated on the the possibility to use density boundary values, respectively the variability of the thermal wind transport, for a potential predictability analysis of the AMOC. More specifically, we analyze whether the latitudinal varying potential predictability of the AMOC (Kröger et al., 2012; Tiedje et al., 2012) can be reconstructed from the latitudinal varying zonal density gradients. Furthermore, we test whether we can separate the eastern and western boundary influence on the total thermal wind transport's potential predictability. This part of the study is motivated by previous observation-based and model-based studies that indicate that the longterm variability of the AMOC primarily arises from the western boundary, while the contribution to the seasonal variability is slightly higher from the eastern than from the western boundary (e.g., Chidichimo et al., 2010; Fischer et al., 2013).

Actual predictive skill in the density gradient can be found at 26°N (Matei et al., 2012a) but for other latitudes only *potential* predictability is possible, and thus our analysis will be based on a numerical model. We use the same variance based prognostic potential predictability approach (PPP) as in Tiedje et al. (2012) and generate a hindcast ensemble based on an oceanic state estimate. Since the oceanic state estimate is dynamically consistent with observations over a 50 year period, it provides an observation-based reference simulation, as well as good initial conditions for the ensemble generation. These are important for potential predictability analysis on inter-annual time scales (Collins, 2002; Collins et al., 2006) and improve over predictions without the knowledge of the ocean state (e.g., Troccoli and Palmer, 2007; Smith et al., 2007; Keenlyside et al., 2008; Pohlmann et al., 2009; Zhang, 2011).

In short, we test in the present study whether the basin-wide AMOC can be potentially predicted pre-dominantly relying on capturing the thermal wind variability from observations. Specifically, we firstly analyze the variability and potential predictability of the thermal wind transport in comparison to the AMOC minus the Ekman contribution, before we discuss the relation between the potential predictability of the thermal wind transport and the total AMOC.

3.2 Model and methods

3.2.1 Reference run and hindcast ensembles

We base our analysis of the thermal wind variability and the subsequent ensemble predictability analysis on the oceanic data assimilation product GECCO (German partner of the consortium for Estimating the Circulation and Climate of the Ocean; Köhl and Stammer, 2008). We use a slightly corrected version of the GECCO synthesis' optimized forcing to generate a 50-year integration, covering the same period as the original GECCO run (1952-2001). This integration represents the reference run for the predictability analysis and provides the initial conditions for the ensemble generation. For all following analyses, we focus on the period from 1959 to 2001 of this integration.

As in Tiedje et al. (2012), we initialize 10 ensembles from the reference run starting one year apart (1983, ..., 1992). In each ensemble, the ensemble members are generated using different 10-year periods of GECCO's corrected optimized atmospheric forcing. Within each ensemble, the forcing periods (from 1959 to initial condition's date) and the hindcast period (from initial condition's date onward) do not overlap. This setup results in ten 10-year ensembles at 15 to 24 members. Further details on the reference run and the rationale of the ensemble generation can be found in

Tiedje et al. (2012).

3.2.2 AMOC decomposition

Based on the AMOC decomposition of Lee and Marotzke (1998) and Marotzke et al. (1997), several studies continued the approach of reconstructing the AMOC from the zonal wind stress and the zonal density differences (e.g., Hirschi et al., 2003; Baehr et al., 2004; Hirschi and Marotzke, 2007; Fischer et al., 2013). In the following, we will describe the theoretical calculation and the implementation of the thermal wind transport (Hirschi and Marotzke, 2007) and the depth-dependent Ekman transport (Baehr et al., 2004). Subsequently, we will test the agreement between the thermal wind and the AMOC minus the Ekman variability, by analyzing the mean and the variance of the depth- and latitude-dependent zonally averaged velocity fields and integrated transports. Note that we analyze in chapter 3.2.2.3 only the reference run (1959 to 2001), and that the variance calculations are based on annual means (as the subsequent inter-annual potential predictability analysis is on annual means, too).

3.2.2.1 Theory

Based on the thermal wind balance, we obtain a depth dependent meridional velocity component for every investigated latitude (0° to 60°N):

$$\tilde{v}(x,z) = -\frac{g}{\rho^* f}\int_{-H}^{z}\frac{1}{L(z')}(\rho_e(x,z') - \rho_w(x,z'))\ dz', \tag{3.1}$$

where g is the earth's gravity, ρ^* is the reference density, f is the Coriolis parameter, H is the ocean depth ($-H \leq z' \leq 0$), $L(z')$ is the basin width, and ρ_e and ρ_w are the densities at the eastern and western boundary. $\tilde{v}$ is then used to obtain a stream function:

$$\tilde{\psi}(z) = \int_{x_w}^{x_e}\int_{-H}^{z}\tilde{v}(x,z')\ dxdz', \tag{3.2}$$

where x_e and x_w are the western and eastern limits of the basin. In order to ensure mass balance across a zonal section, we introduce a correction for $\tilde{v}$:

$$\hat{v}(x,z) = \Psi(0)/A. \tag{3.3}$$

We divide the transport imbalance $\Psi(0)$ across a longitude-depth section by the section area A. The stream function for the thermal wind transport can now be written as:

$$\Psi_{TW}(z) = \int_{x_w}^{x_e} \int_{-H}^{z} (\tilde{v}(x, z') - \hat{v}(x, z'))\ dxdz'. \tag{3.4}$$

For details and limitations of this method see e.g. Hirschi and Marotzke (2007). In the following, we will abbreviate the thermal wind velocity field with TWv and the thermal wind transport with TW.

The depth-dependent transport related to the wind stress is calculated following Baehr et al. (2004). Based on the Ekman velocity (v_{ek}; eq. 3.5), a corrected Ekman velocity field is introduced ($v_{ek_{corr}}$; eq. 3.6) to ensure no net meridional mass transport related to the zonal wind stress:

$$v_{ek}(x, y, z) = -\frac{1}{\rho^* f A_d} \int_0^{L(y,0)} \tau(x, y)\ dx, \tag{3.5}$$

$$v_{ek_{corr}}(x, y, z) = \begin{cases} v_{ek} - \frac{v_{ek} A_d}{A} & \text{for } -d \geq z \\ -\frac{v_{ek} A_d}{A} & \text{for } -d < z \end{cases}, \tag{3.6}$$

where $\tau(x, y)$ is the zonal wind stress, A_d is the section area to the Ekman depth d, and $L(y, 0)$ is the zonal extent of the basin. Integrating $v_{ek_{corr}}$ results in an Ekman transport that is zero at the surface and at the bottom of the ocean. In the following, we will abbreviate the model velocity field minus the Ekman velocity field with *v-Ekv* and the AMOC minus the Ekman transport with *AMOC-Ek*.

3.2.2.2 Implementation

Kanzow et al. (2009) and Chidichimo et al. (2010) find that the density (ρ_e and ρ_w) needs to be taken directly at the continental slope to compute the full-basin density gradient and to capture the variability of the AMOC reliably. Figure 3.1 illustrates the positions of the density values used for the TW calculations. Note that the Mid Atlantic Ridge has to be cut out to capture the zonally integrated (geostrophic) shear between the eastern and western boundary. At some latitudes, the irregular topography complicates the decision for the best boundary value position. We therefore define to select the density values right at the boundary only as

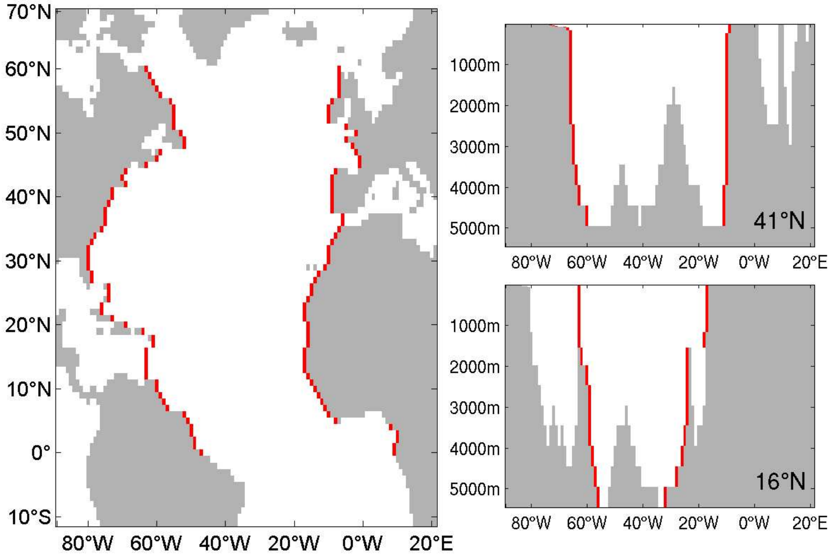

Fig. 3.1: North Atlantic surface layer mask for selecting density boundary values (left panel). The right panels show the selected density boundary values for two sections (41°N and 16°N).

long as there are at least 10° between the continental slope and the closest submarine topographic elevation. If the distance is smaller than 10°, the density values are selected at the open-ocean-side of the topographic elevation. Based on this definition, the Gulf of Mexico and the Caribbean Sea are topographically separated from the basin. Therefore, we consider only the mid-ocean transport between ∼10°N and ∼30°N (see lower right panel in Figure 3.1). Note that the problematic manual selection of the density boundary values could lead to irregularities or outliers in the resulting TW.

For the calculation of the depth-dependent Ekman velocity field, we define the Ekman depth as the upper 10m of the ocean (surface model layer). The subsequent potential predictability analysis of AMOC-Ek is conducted with the subtraction of the transports at ∼1000m depth.

3.2.2.3 Representativeness of the thermal wind transport

Without correcting the TWv, we would assume vanishing velocity at the bottom, which could lead to an inaccurate representation of the velocity (Baehr et al., 2004). To test whether the correction significantly changes structural features of the zonally averaged velocity field in the reference run, we compare the mean and the variance

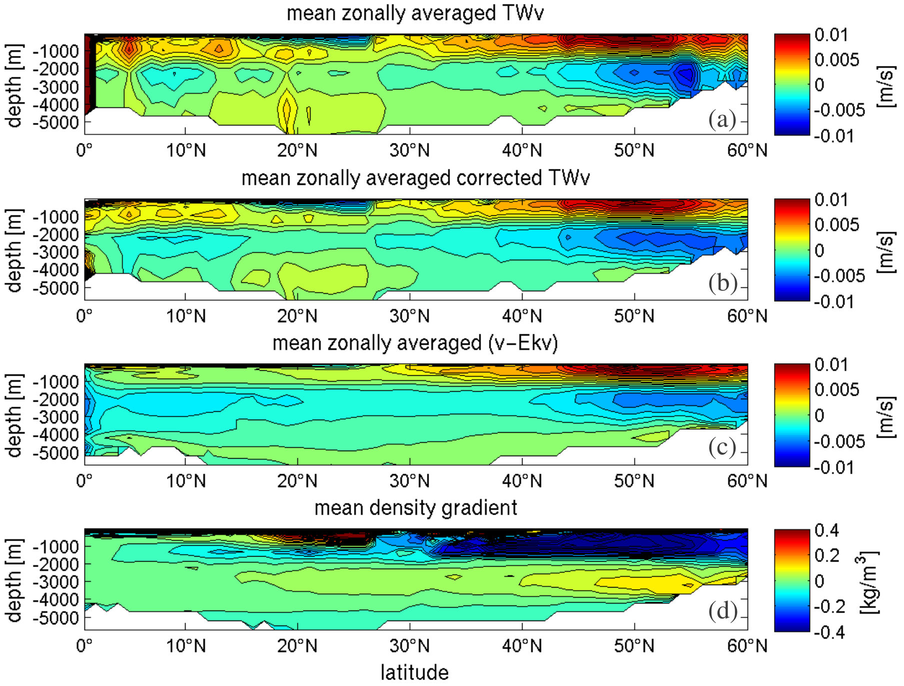

Fig. 3.2: Mean zonally averaged velocity fields of the reference run: (a) uncorrected thermal wind velocity field (TWv), (b) corrected TWv, (c) meridional velocity field minus the Ekman velocity field (v-Ekv). (d) Mean density gradient. The contour intervals are 0.001 m/s and 0.04 kg/m^3. Note that the topographic elevation is not the same for the v-Ekv section and the TWv section because the density boundary values could not always be selected at the deepest point of the section.

of the corrected and the uncorrected TWv in latitude-depth sections (Fig. 3.2a and b and Fig. 3.3a and b).

North of ∼30°N, both the uncorrected and corrected TWv show an upper positive (above ∼2000m) and a lower negative region with maximum and minimum values about 0.02 m/s and -0.008 m/s (Fig. 3.2a and b). Towards the bottom (below ∼3000m) mean velocities are northwards again. For the uncorrected TWv the minimum of the negative region is slightly stronger and shifted northward. South of ∼30°N, these regions of northward and southward velocities seem to continue southward, but the gradient decreases and irregular local maximum velocities occur. Despite small differences, the main features of the TWv are not altered by the mass balance correction.

Particularly with regard to the subsequent potential predictability analysis, we need

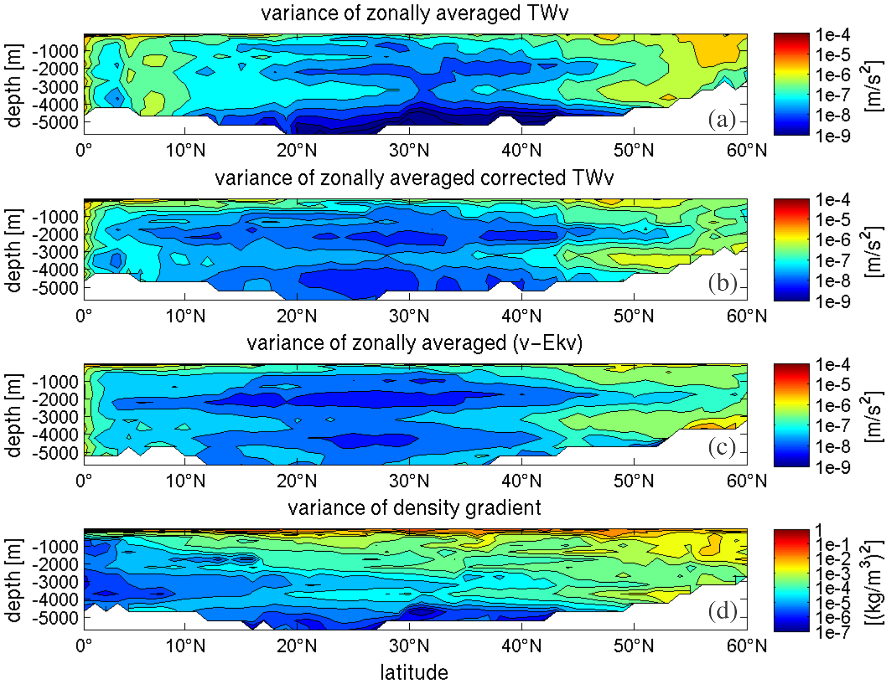

Fig. 3.3: Variance of annual mean values of the zonally averaged velocity fields of the reference run: (a) uncorrected thermal wind velocity field (TWv), (b) corrected TWv, (c) meridional velocity field minus the Ekman velocity field (v-Ekv). (d) Mean density gradient. The contour intervals are 0.07 $(m/s)^2$ and 0.07 $(kg/m^3)^2$. Note that the topographic elevation is not the same for the v-Ekv section and the TWv section because the density boundary values could not always be selected at the deepest point of the section.

to test whether the variance of the TWv is altered by the mass balance correction (Fig. 3.3a and b). As for the mean, we find that the overall representation is not significantly different between the uncorrected and the corrected TWv (Fig. 3.3a and b). Between ∼10°N to ∼40°N, we find small variance values that increase to the north and south. The highest variances occur north of ∼45°N, where we find an upper (∼1000m) and an lower maximum (∼4000m). In between, at ∼2000m, small variance values occur, right where we find the the boundary between the northward and southward flowing water (Fig. 3.2a and b). We also find a second variance minimum region near the bottom, implying another direction change in the velocity field.

Additionally, figure 3.2d and figure 3.3d show the mean and the variance of the density gradient to illustrate the relation given in equation 3.1. North of ∼30°N, we find for the mean values a strong negative gradient above ∼2000m and a weak positive

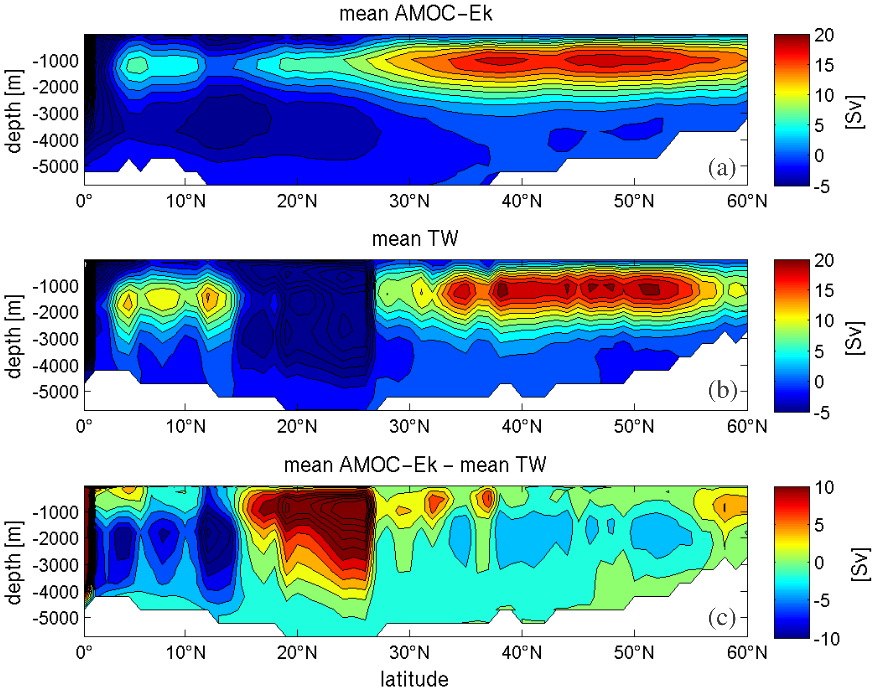

Fig. 3.4: (a) Mean AMOC minus the Ekman transport (AMOC-Ek) based on the meridional velocity field. (b) Reconstruction based on the mean thermal wind contribution (TW). (c) Difference between the mean AMOC-Ek and the reconstruction. The contour interval is 2 Sv.

gradient below. In the mid-ocean transport region, the density gradient becomes positive in the upper 500m. For the variance, we find high values everywhere in the upper ocean and north of ∼40°N also in the deeper ocean.

So far, we have ensured that the mass balance correction does not alter the TWv. With this result we can now turn to our physical analysis and estimate the agreement between the TWv and the v-Ekv (Fig. 3.2c and Fig. 3.3c). North of ∼30°N, the structural features of the mean zonally averaged v-Ekv (Fig. 3.2c) are very similar to those of the TWv (Fig. 3.2b). In contrast to the TWv, the gradient in the v-Ekv decreases very smoothly south of ∼30°N. The biggest differences can be found between ∼10°N and ∼30°N, since we only assess the mid-ocean transport for the TWv at these latitudes. At these latitudes, we also notice unfitting southward velocities in the upper 500m. For the variance, only small differences in structure and magnitude can be seen between the v-Ekv (Fig. 3.3c) and the TWv (Fig. 3.3b). It seems that even between ∼10°N and ∼30°N, the variances of the TWv and the v-Ekv show a reasonable agreement.

In a next step, we calculate the stream functions from the zonally- and depth-integrated velocity fields to show if the overturning cells of the AMOC-Ek and the TW exhibit similar features. We first consider the mean of both quantities and their difference (Fig. 3.4), before we turn to the variances that will play a more important role in the subsequent potential predictability analysis (Fig. 3.5).

The main AMOC-Ek overturning cell extents from ∼60°N to ∼30°N (Fig. 3.4a). Maximum values are reached around 45-50°N and at ∼1000m depth with values of 22 Sv. Between ∼30°N and ∼10°N AMOC-Ek values decrease to around 0 Sv, before they increase again up to 5 Sv around ∼5°N. North of ∼30°N, the meridional extent and strength of the TW overturning cell (Fig. 3.4b) are similar to what is seen for the AMOC-Ek, except for some irregularities (which are probably due to the problematic selection of density boundary values). Between ∼15°N and ∼25°N, we find strong negative TW values as a consequence of the omitted positive velocities in the Gulf of Mexico and the Caribbean Sea. Here, the shortcomings between the AMOC-Ek and the TW are most pronounced in the upper 3000m (Fig. 3.4c). Towards the equator, the TW values increase again, but exceed the AMOC-Ek values by 5 to 10 Sv. North of ∼30°N, the difference seldom exceeds 2 Sv.

Turning to the variance of the annual mean AMOC-Ek and TW, we find high variance at about the same depth and latitude where we find high mean values for both quantities (Fig. 3.5a,b). As the mean values, the variance decreases north of ∼55°N and between ∼15°N and ∼25°N until it increases again towards the equator. The extremely high values at the equator reflect the division by the Coriolis parameter in the TW and Ekman transport calculation, and should therefore be ignored. The differences between the variance of the AMOC-Ek and the TW are largely zero below ∼3000m (Fig. 3.5c). With the equatorial region excluded, we find the largest differences between 45°N and 55°N where the variance of the TW exceeds that of the AMOC-Ek by more than 2.5 Sv. Southward, the difference alternates until the variance of the AMOC-Ek exceeds that of the TW from ∼30°N to ∼15°N. Further south, the difference changes sign again.

Overall, we find similar spatial structures for both the mean and the variance for the zonally averaged velocity fields and the transports, although the absolute values show some differences. One has to be careful about the region between ∼15°N and ∼25°N because of the reversed mean TW, yet this region does not significantly stand out for the variance. The agreement between the spatial structure of the variances

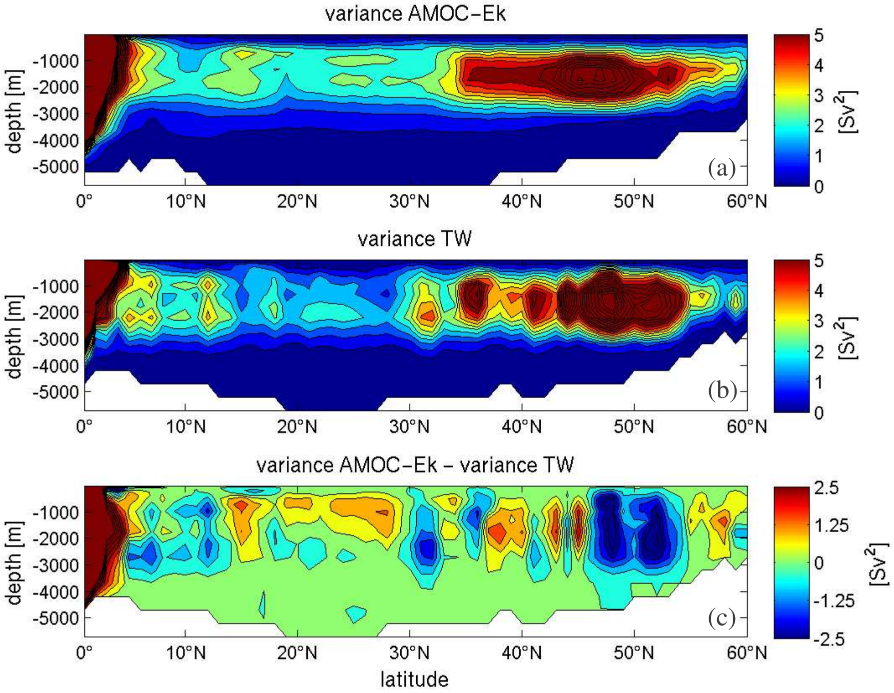

Fig. 3.5: (a) Variance of annual mean values of the AMOC minus the Ekman transport (AMOC-Ek) based on the meridional velocity field. (b) Variance of annual mean values of the reconstruction based on the mean thermal wind contribution (TW). (c) Difference between the variance of AMOC-Ek and the variance of the reconstruction. The contour interval is 0.5 Sv^2.

is eventually the more important part when turning to the potential predictability analysis, since only the ratio of the spread and the variance will play a role.

3.2.3 Quantifying the potential predictability

As in Pohlmann et al. (2004) and Tiedje et al. (2012), the prognostic potential predictability (PPP) of a quantity is determined using the ratio of the ensemble spread as a function of time to the variance of the detrended reference run from 1959 to 2001. Since this ratio is subtracted from 1, a PPP value of 1 indicates perfect potential predictability, whereas a PPP value below 0 indicates no potential predictability. Following Pohlmann et al. (2004), we estimate the significance of PPP using an F-test.

Detrending the reference run is necessary to avoid artificial predictability. The reference run is detrended by removing the best straight-line fit from the monthly mean model data. The potential predictability is estimated for every latitude from 0° to 60°N in the North Atlantic. In the following, *PPP structure* stands for the spatial and temporal extent of the significant PPP values across the North Atlantic, and *predictable lead time* stands for the time period over which the PPP values are significant. Further details on the potential predictability measure, the significance calculation, and the limitations of the used ensemble can be found in Tiedje et al. (2012).

3.3 Results

This section is divided into three parts: First, the potential predictability of the TW as introduced in the methods section (in the following: *total TW*) is analyzed. Second, boundary experiments are conducted to analyze the influence of the eastern and western boundary on the total TW's potential predictability. Third, we investigate the relation between the potential predictability of the total TW and the total AMOC. In all parts, the results are always considered in regard to the AMOC-Ek.

Since the reference run and the ensembles are conducted with the same model setup, we assume similar dynamical evolutions of the integrations. Tiedje et al. (2012) has already shown that the spread of the ensemble mirrors the variance of the detrended reference run to a certain degree. Thus, prior to every potential predictability analysis, we specifically consider the latitudinal variation of the respective quantities' variability in the detrended reference run.

3.3.1 The total thermal wind transport

3.3.1.1 Variability of the thermal wind transport

The variance of the detrended and annually averaged AMOC-Ek and TW show similar latitudinal variations, with increased variance at the high latitudes (45°N-60°N) and towards the equator (0°-20°N), and a minimum in between (∼30°N; Fig. 3.6). The region of the reversed mean TW (15°N-30°N, Fig. 3.4b) does not significantly stand out in the variance of the detrended TW. Of particular note, however, are the large fluctuations of the TW's variance at the northern latitudes. But since in the TW calculations for the ensembles the same boundary density positions are used, we assume that the outliers are reduced in the ratio between the spread and the reference variance in the subsequent potential predictability calculation.

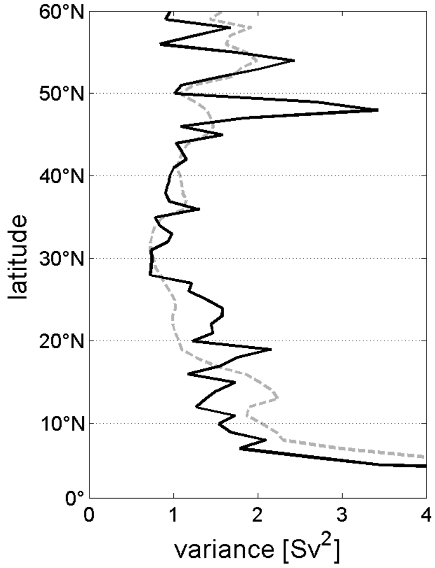

Fig. 3.6: Variance of AMOC-Ek (grey) and TW (black) in the reference run. The monthly mean model output is detrended prior to the annual averaging and variance calculation.

3.3.1.2 Potential predictability of the thermal wind transport

We now turn to the analysis of the PPP structures of the AMOC-Ek, the TW and the depth-integrated density gradient from 360m to the bottom (Fig. 3.7). The AMOC-Ek's PPP structure shows a maximum between 35°N and 45°N with predictable lead times of about 4 years. To the north and south, the predictable lead times decrease quickly to about 1-2 years (Fig. 3.7a). Except for some irregularities, we find the same PPP structure for the TW (Fig. 3.7b). Even a small increase in PPP around 10°N is comparable in both PPP structures. We find this concentration of high predictable lead times between 35°N and 45°N as well for the depth-integrated density gradient, indicating that the presented TW's PPP structure results from the variability of the density gradient (Fig. 3.7c). It should be noted, that a similar structure is evident for depth-integrations of the density gradient from 0m-1000m to the bottom. These PPP structures of the depth-integrations of the density gradient become more similar to the PPP structure of the TW, the more surface signals are excluded (not shown).

We cannot fully explain the characteristic PPP structure of the AMOC-Ek, the TW and the depth-integrated density gradient, but we give some elements of explanation below. We assume that the variance increase of the reference run at lower and higher

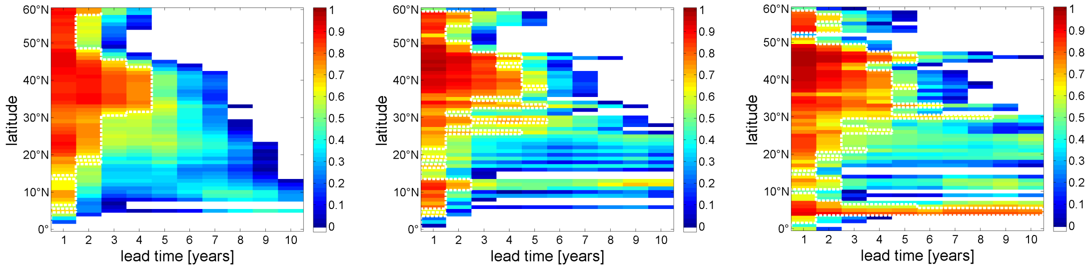

(a) (b) (c)

Fig. 3.7: Hovmöller diagrams of the PPP as a function of lead time (Atlantic: 0° - 60°N) for (a) AMOC-Ek, (b) TW, and (c) density gradient (depth-integrated from 360m to bottom). The white dashed lines indicate values significant at the 90% level.

latitudes (Fig. 3.6) originates from spatially restricted complex dynamics that result in temporally irregular occurring variations. Further, we assume that the ensemble members show a similar dynamical behavior as the reference run, which results for the temporal evolution in a faster growing spread between the members. In other words, highly variable regions leave more room for the ensemble members to evolve differently, respectively, to run into different directions.

I assume that at the northern latitudes, the AMOC predictability is influenced by Kelvin waves that communicate density anomalies, originating from the NAO, from the subpolar region toward the subtropical region (e.g., Köhl, 2005; Köhl and Stammer, 2008). These southward traveling density anomalies at the western boundary could be a reason for the shorter predictable lead times at the northern latitudes and longer predictable lead times when the signal travels further south. Rossby waves that affect the AMOC variability by modifying the east-west density gradient become more important farther south and travel at the southern edge of the subtropical gyre (e.g. Köhl, 2005; Getzlaff et al., 2005; Hirschi et al., 2007). These westward propagating density anomalies could be responsible for the limitation of the potential predictability of the density-driven AMOC at the subtropical latitudes.

Focusing now on the full potential predictability field (i.e. all PPP values above 0), we find from 15°N northward decreasing predictable lead times with increasing latitudes. We assume that this can be explained by the relation between the mean absolute density gradient and the strength of the variability: The stronger the density gradient, the more difficult it is for the members to vary in their paths (indicated by a small growing spread), and the predictable lead times become longer. If we calculate the simple ratio between the mean absolute density gradient and the vari-

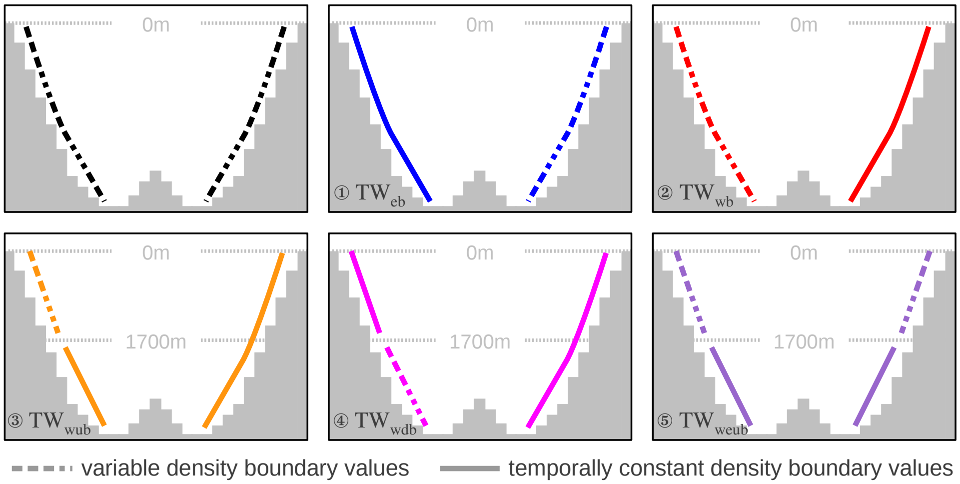

Fig. 3.8: Overview of the conducted experiments to calculate the TW from density boundary values: The upper left panel shows the total TW, with temporally varying density values at both boundaries. For all cases the dashed lines represent temporally varying density values and the solid lines represent temporally constant density values. In the following analysis, each experiment is indicated by the color presented here. The total TW is always represented in black.

ance of the reference run, we find a decrease towards the high latitudes, indicating a decreasing PPP structure (not shown).

3.3.2 Boundary experiments: spatially separating the total thermal wind transport's contributions

To investigate the relative contribution of the eastern and western boundary density to the variability of the total TW, we design 5 experiments, which are summarized in figure 3.8. To calculate the depth-dependent meridional velocity $\tilde{v}$ (equation 3.1), we hold the density boundary values temporally constant at one side of the basin, while keeping the full signal at the other side in experiment 1 and 2. For the experiments 3 and 4, we hold the density values at the eastern boundary and the western upper or lower temporally constant (above or below ∼1700m). For the 5th experiment we keep only the density variability of the upper 1700m. We refer to these experiments by TW_{eb} (1), TW_{wb} (2), TW_{wub} (3), TW_{wdb} (4), TW_{weub} (5), indicating with the subscript the region where the density variability is maintained.

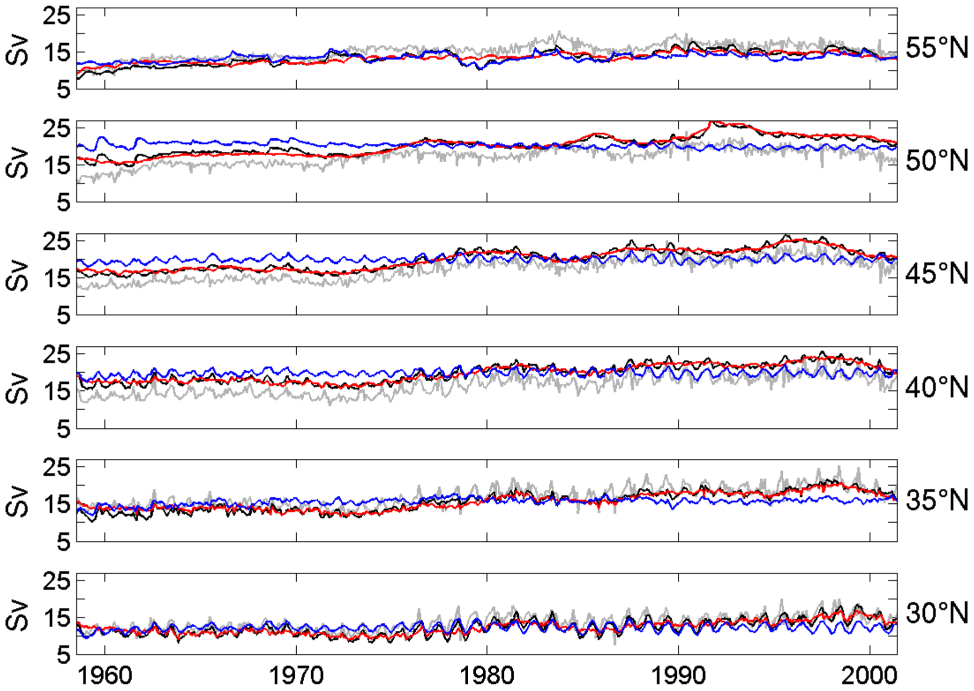

Fig. 3.9: Time series of monthly mean values of the reference run at different latitudes in the North Atlantic: AMOC-Ek (gray), total TW (black), TW_{eb} (blue), and TW_{wb} (red).

3.3.2.1 Boundary experiments: Variability of the thermal wind transport

The monthly mean time series of the total TW, TW_{eb}, TW_{wb} and AMOC-Ek show not only a temporal variability (seasonal and inter-annual) but also a latitudinal variability in the reference run (Fig. 3.9). Whereas the seasonal variability becomes smaller with increasing latitude, the maximum inter-annual variability is found between 40°N and 50°N. Particular at these latitudes it becomes obvious that TW_{eb} shows essentially no inter-annual variability, while TW_{wb} continues along the inter-annual variations of the total TW and the AMOC-Ek.

In order to clarify the spatial separation of variability contributions, we initially consider all boundary experiments at a single latitude (Fig. 3.10). We find that not only the seasonal variability but also the nearly decadal variations of the AMOC-Ek can be represented by the total TW, although its mean is about 1-2 Sv higher. According to Köhl and Stammer (2008), changes of the NAO state are responsible for the long-term variations in the AMOC. The temporal evolution of TW_{wb},

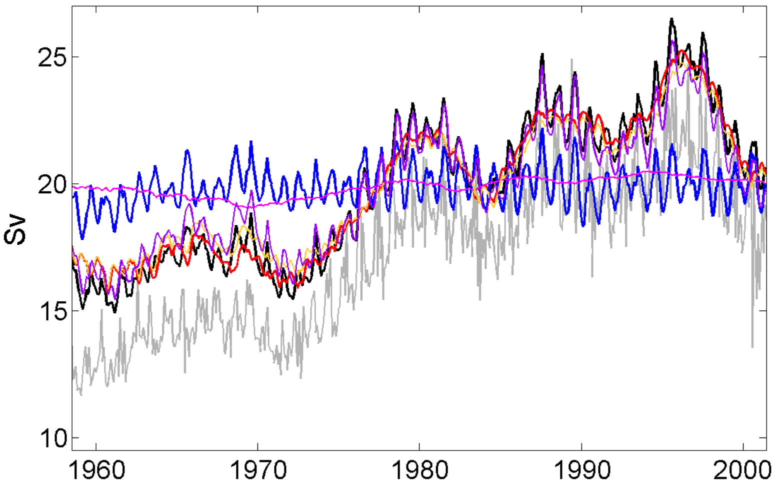

Fig. 3.10: Time series of monthly mean values of the reference run at 45°N: AMOC-Ek (gray), TW (black), TW_{eb} (blue), TW_{wb} (red), TW_{wub} (orange), TW_{wdb} (pink), and TW_{weub} (violet).

TW_{wub} and TW_{weub} are very close to the total TW, with TW_{wb} and TW_{wub} showing smaller seasonal variability than TW_{weub}, since TW_{weub} also includes variability from the upper eastern boundary. In contrast, TW_{eb} shows essentially no inter-annual variability, but a distinctive annual cycle. TW_{wdb} shows neither significant seasonal nor inter-annual variability. In conclusion, the seasonal variability originates to larger parts from the eastern boundary densities than from the western, while the inter-annual variability mainly originates from the upper ∼1700m of the western boundary. Note that this depth-dependent separation can also be seen in the variances figure 3.5b.

In order to quantify these findings not only at a single latitude but at every latitude, we calculated the correlation between the AMOC-Ek and the TW as well as all TW experiments, on a monthly mean and annual mean basis (Fig. 3.11). To exclude artificially increased correlation coefficients, we detrend the reference run.

On a monthly basis, the correlation coefficient of the AMOC-Ek and the total TW largely varies around 0.5 (Fig. 3.11a). Minimum correlation around 0.4 can be seen between 15°N and 25°N and maximum correlation up to 0.7 is evident around 10°N and between 25°N and 55°N. TW_{weub} shows a very similar correlation with AMOC. TW_{eb}, TW_{wb}, TW_{wub}, and TW_{wdb} show at most latitudes a weaker correlation to

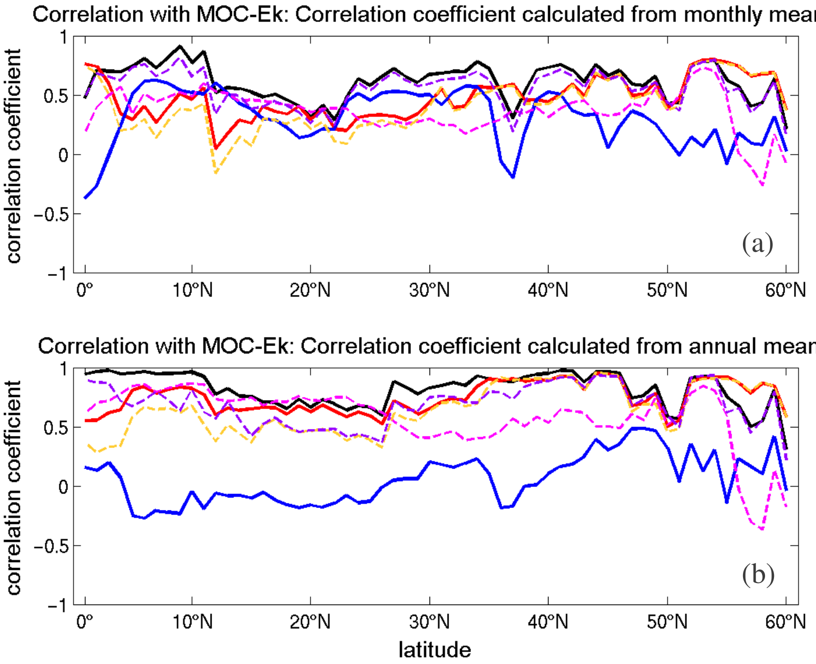

Fig. 3.11: Correlation on a (a) monthly and (b) annual basis between AMOC-Ek and: total TW (solid black), TW_{eb} (solid blue), TW_{wb} (solid red), TW_{wub} (dashed orange), TW_{wdb} (dashed pink), TW_{weub} (dashed violet) . Prior to the calculations, the monthly mean values are detrended.

AMOC-Ek, with correlation coefficients ranging mainly between 0 and 0.5. Between 5°N and ~40°N, TW_{eb} shows a higher correlation with AMOC-Ek than the very similar running TW_{wb} and TW_{wub}, while north of ~40°N, TW_{wb} and TW_{wub} show a higher correlation.

On an annual basis, the correlation of TW_{eb} with AMOC-Ek decreases, while the correlation of the total TW and TW_{wb}, TW_{wub}, TW_{wdb}, and TW_{weub}generally increase (Fig. 3.11b). Small correlation coefficients of TW_{eb} (ranging around zero and never exceeding 0.5) indicate that the variability originating from eastern boundary densities contributes only little to the total inter-annual total TW variability. Most of the total TW variability can be represented by the variability of the western boundary densities. North of 35°N, particularly the upper ~1700m seems to be responsible for the good correlation to the AMOC-Ek.

Although correlating two time series does not express anything about the magnitude of variability, figure 3.11 confirms the conclusions for figure 3.10 at all latitudes, and

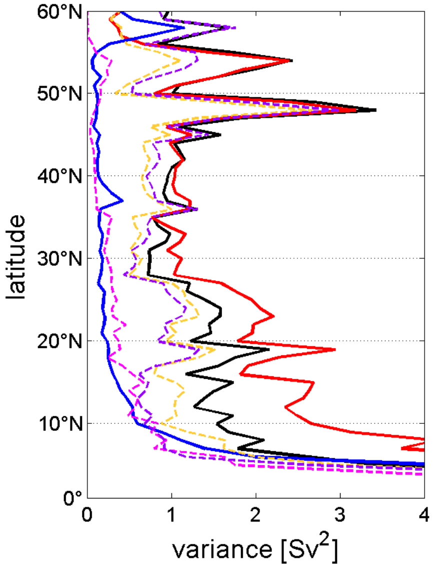

Fig. 3.12: Variance of detrended and annually averaged reference run: total TW (solid black), TW$_{\mathrm{eb}}$ (solid blue), TW$_{\mathrm{wb}}$ (solid red), TW$_{\mathrm{wub}}$ (dashed orange), TW$_{\mathrm{wdb}}$ (dashed pink), TW$_{\mathrm{weub}}$ (dashed violet).

reveals quite clearly the eastern and western boundary contribution to the total TW variability.

So far, we have considered monthly and annual TW averages of the reference run to facilitate a better understanding of the variability contributions from the eastern and western boundary densities. On the way towards inter-annual potential predictability, we are only interested in the inter-annual variability for the following analysis. As before in chapter 3.3.1, we initially present the detrended and annually averaged variance of all boundary experiment's TW for the reference run (Fig. 3.12).

We find that the variability of the eastern boundary (TW$_{\mathrm{eb}}$) and the western deeper boundary (TW$_{\mathrm{wdb}}$) alone contribute only little to the total variance of TW. In contrast, the variability of the western boundary (TW$_{\mathrm{wb}}$) alone generally continues along the total variance, but overestimates the total variance of TW south of ∼30°N. This implies that another signal is included in the western boundary variability that does not play a role for the total variability, or that the signal is superimposed by signals from the eastern boundary. The variances of the upper ocean (TW$_{\mathrm{wub}}$ and TW$_{\mathrm{weub}}$) are at all latitudes smaller than that of the total TW, but show similar latitudinal variations with the smallest spread between ∼30°N and ∼50°N. Note

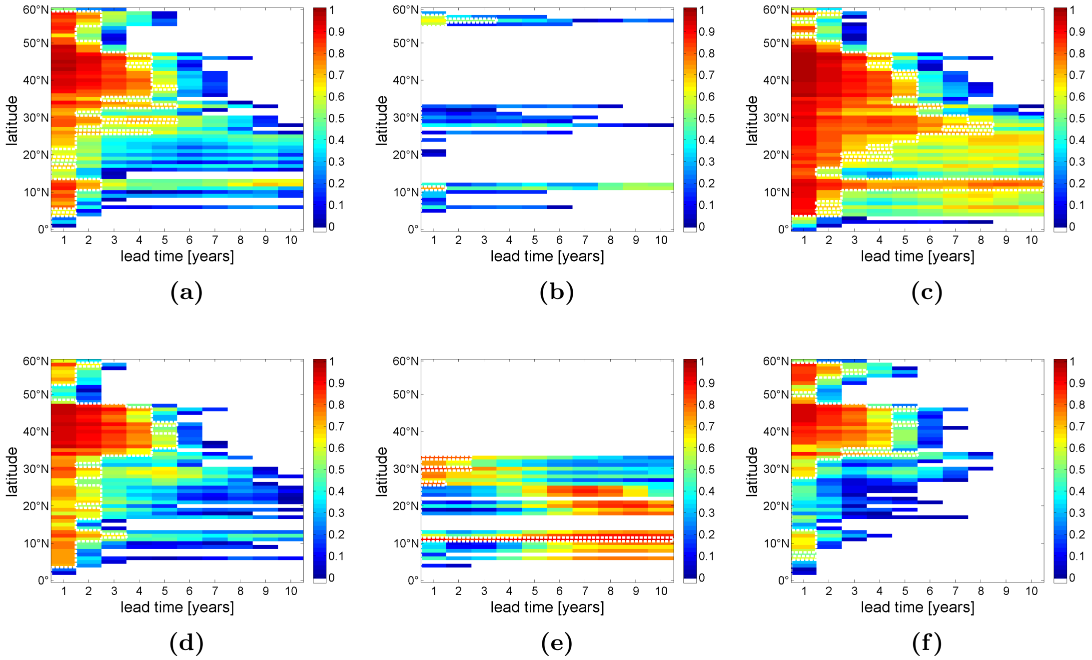

(a) (b) (c)

(d) (e) (f)

Fig. 3.13: Hovmöller diagrams of the PPP as a function of lead time (Atlantic: 0° - 60°N) for (a) total TW (same as in figure 3.7b) and (b-f) TW for all boundary experiments (arranged in the same order as in figure 3.8). The white dashed lines indicate values significant at the 90% level.

that north of 55°N a significant contribution to the total variance seems to originate from the upper eastern boundary.

Overall, we find that only the density variability of the upper ∼1700m, and mainly that of the western boundary, contribute significantly to the full inter-annual TW signal, respectively, would be necessary to reconstruct most of the total inter-annual TW variance. For the subsequent PPP analysis, we expect a similarly dominant influence of the western boundary on the total TW's PPP structure.

3.3.2.2 Boundary experiments: Potential predictability of the thermal wind transport

We now turn to the potential predictability analysis for the boundary experiments. As for the reference run, the boundary densities are held temporally constant at one side of the basin and/or below or above ∼1700m for every ensemble member. Not surprisingly, the temporal evolution of the western boundary densities is sufficient to reconstruct most of the total TW's PPP structure although particular south of 30°N, TW_{wb} shows higher PPP values and longer predictable lead times (Fig. 3.13c).

By additionally omitting the influence of the deeper western boundary densities, the PPP structure becomes more similar to the total TW's PPP structure south of 30°N ($\mathrm{TW}_{\mathrm{wub}}$; Fig. 3.13d). If we add the influence of the upper eastern boundary densities to the upper western boundary densities, we find that the potential predictability is underestimated south of 30°N, but the PPP structure north of 50°N shows a closer resemblance to the total TW's PPP structure ($\mathrm{TW}_{\mathrm{weub}}$; Fig. 3.13f).

The influence of the lower western boundary densities and the eastern boundary densities on the inter-annual potential predictability is small ($\mathrm{TW}_{\mathrm{wdb}}$ and $\mathrm{TW}_{\mathrm{eb}}$; Fig. 3.13e and b). Both TW experiments show significant potential predictability only at a few latitudes. But since these few occasions are not total outliers, a small regional influence cannot be excluded. For example, the increased potential predictability of $\mathrm{TW}_{\mathrm{eb}}$ around 55°N, could indicate an influence of the upper eastern boundary densities at these latitudes.

3.3.3 Relating the potential predictability of the thermal wind transport to the AMOC

So far, only the relation between the TW and AMOC without the Ekman transport was considered. This leaves us with the question of how much would we know about the potential predictability of the total AMOC by only observing the boundary densities.

As before, we start with analyzing the variance of the reference run (Fig. 3.14a). The inter-annual variance of the AMOC shows a slight decrease from the higher latitudes ($\sim$1.5Sv^2) to about 30°N ($\sim$1Sv^2), followed by a slight increase towards the equator ($\sim$1.1Sv^2). North of 30°N, the variability of the variance values is much higher. From 60°N to 20°N, the variance of the Ekman transport remains constant about 0.1Sv^2 until it abruptly increases at 20°N and exceeds the AMOC's variance at 10°N. Between 60°N and 20°N, the subtraction of the Ekman transport from the AMOC seems to play a minor role on inter-annual time scales. The expected reduction of the variance is only evident between 30°N and 55°N. South of 20°N, the variance of the AMOC-Ek increases disproportionately towards the equator, indicating that with the subtraction of the Ekman transport a signal is removed that does (originally) not contribute to the total AMOC's variance. If we calculate the variances with monthly means, we find, as expected, smaller variances for the AMOC-Ek than for the total AMOC everywhere north of 7°N (not shown). The correlation between the AMOC and the Ekman transport is significantly lower on an inter-annual time scale than on a seasonal time scale.

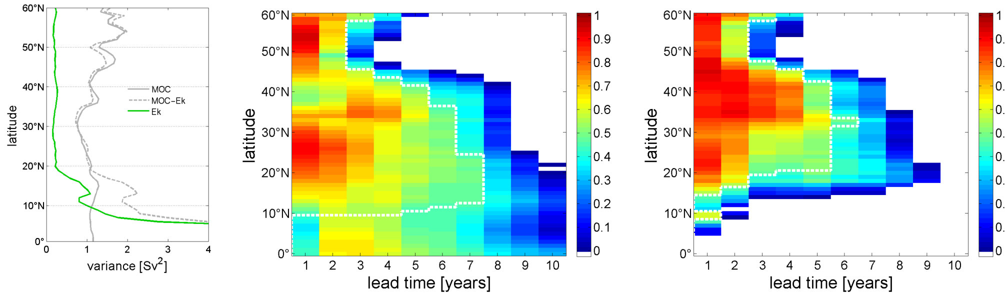

(a) **(b)** **(c)**

Fig. 3.14: Relation between AMOC and Ekman transport (Atlantic: 0° - 60°N): (a) Detrended and annually averaged reference run: variance of the Ekman transport (green), AMOC (gray), and AMOC-Ek (gray dashed). (b) and (c): Hovmöller diagrams of the PPP as a function of lead time for the AMOC (b; cp. Fig. 8 from Tiedje et al. (2012); *cp. Fig. 2.8*) and the AMOC-Ek with the ensemble spread divided by the reference variance of the total AMOC (c). The white dashed lines indicate values significant at the 90% level.

The PPP structure of the AMOC was already shown in Tiedje et al. (2012), however, its origins were not discussed in detail (Fig. 3.14b). The predictable lead times increase continuously from 2 years between 45°N and 60°N to about 6-7 years between 15°N and 25°N. At a first glance, the AMOC's PPP structure does not seem similar to the AMOC-Ek's PPP structure (Fig. 3.7a), implying that the influence of the Ekman transport on the inter-annual PPP cannot be ignored. To analyze the Ekman transport's influence on the predictable lead times of the AMOC, we divide the ensemble spread of the AMOC-Ek by the variance of the total AMOC, instead of the variance of the AMOC-Ek in the PPP calculation (Fig. 3.14c). The resulting PPP structure is already quite similar to the original PPP structure of the AMOC-Ek (Fig. 3.7a), but the changes in the ensemble spread due to subtraction of the Ekman transport are easier to understand, since the denominator and the significance limit are the same for both PPP calculations. Between 60°N and 40°N, the predictability lead times are generally the same as for the AMOC, but south of 35°N, the potential predictability decreases faster. In contrast to the AMOC, we find continuously high PPP values around 40°N, where we find the maximum predictable lead times.

To understand the structural changes in the PPP, we need to distinguish between the ensemble spread behavior of the first 1-2 years, that influences the initial magnitude of the PPP values, and the temporal evolution of the ensemble spread. We assume that the dynamical behavior of the reference run and the individual ensemble members is similar, and that an increase of the reference run's variance is equivalent to a faster growing ensemble spread. As indicated by the behavior of the reference run's variance between 30°N and 55°N, the subtraction of the Ekman transport decreases the initial ensemble spread, resulting in significantly higher PPP values around 40°N. To the south (particular south of 20°N), the increase of the reference run's variance after the Ekman transport subtraction implies for the ensemble a faster growing spread, and thus shorter predictable lead times. The remaining differences between the figure 3.14c and the original AMOC-Ek's PPP structure (Fig. 3.7a) can be explained by the changes in the reference run's variance due to the Ekman transport (Fig. 3.14a) and a higher significance limit. With this consideration, we can at least understand the technical origin of the transition from the AMOC's to the AMOC-Ek's PPP structure.

We assume that the dynamical origin of the initially low PPP values around 40°N are due to irregular wind fields at the gyre boundary that are able to offset the initial conditions for the ensemble members (resulting in a large initial spread), but have no significant influence on the temporal evolution of the AMOC on longer timescales. Indeed, the Ekman transport does not seem to influence the predictable lead times significantly north of 35°N-40°N. South of 20°N, where the reference run's variance indicates that the Ekman signal does not contribute to the AMOC variability (cp. Fig. 3.14a), the predictable lead times could be artificially lengthened and the presented PPP structure could be misleading at these latitudes. Possible dynamical reasons for the general PPP structure, with one maximum around 40°N and decreasing potential predictability to the north and south, are assumed to lie in temporally irregular occurring density anomalies at the northwestern boundary and at the subtropical latitudes (cp. chapter 3.3.1.2).

3.4 Discussion

The PPP structure of the total TW can largely be reconstructed from the temporal variability of the upper western density boundary values. Although we find similarities between the PPP structure of the TW and the AMOC, the influence of the Ekman transport cannot be neglected.

The similarities between the PPP structures of the TW and the AMOC without the Ekman contribution, give confidence to the robustness of the presented structure. However, especially the mean TW shows limitations for the region between 15°N and

25°N, where a large part of the western boundary current was totally excluded due to the topographic separation of the marginal seas. Yet, the inter-annual correlation between the AMOC and the TW exceeds 0.5 at these latitudes (Fig. 3.11b), and a misleading effect of the omitted regions on the TW's PPP structure cannot be seen. Nevertheless, a revision of the definition to find the significant boundary density positions, that includes the Caribbean Sea and the Gulf of Mexico and results in a smoother latitudinal distribution of the TW, would improve the study and is a matter for future work.

Prior to the PPP analysis, the analysis of the variance and correlation have already shown that on inter-annual time scales the eastern boundary densities would only have little influence on the total TW's PPP structure. This raises the question whether the influence of the eastern boundary densities would be more prominent in the TW's PPP structure on a monthly time scale. We find that changing the temporal averaging of the input data does not significantly change the general PPP structures of the TW boundary experiments (except for the visibility of an distinctive annual cycle). Since the variability of the western boundary densities also includes seasonal variability, although it is not as strong as in the eastern boundary densities, the signal of the western side of the basin still dominates the total TW's PPP structure.

However, the PPP measure is rather unsuited for the analysis of seasonal potential predictability, since the seasonal variations can easily be strong enough to determine the potential predictability directly after the first annual cycle and all significant inter-annual information are lost or superimposed by the seasonal variations. Nevertheless, the consideration of the monthly PPP shows again, how important it is not to rely completely on the significance limit. Tiedje et al. (2012) already discussed that the predictable lead times are subjected to variations, depending on the parameters used to calculate the significance limit. Thus, it is additionally useful and appropriate to consider the PPP values as long as the ensemble spread lies within the variance of the reference run. For example, we consider the full potential predictability field to facilitate a better understanding of the TW's PPP structure and its relation to the AMOC. Anyway, it would be useful to test the robustness of the presented PPP structures with an additional potential predictability measure. Using for example the anomaly correlation (Pohlmann et al., 2009) could also clarify to what extent the PPP measure indicates the temporal correlation between the ensembles and the reference run.

However, neither the agreement between the PPP structures of the AMOC-Ek and the TW, nor the agreement between different potential predictability measures could ultimately prove if the presented structure is robust (in the sense of model independent) or an artificial product of the generated ensemble. The present ensemble is subjected to the limitation of the used ocean-only model. Nonetheless, the present study benefits from the initialization from an oceanic state estimate, and the improved representation of its oceanic variability. A detailed discussion on the limitations of the ensemble setup can be found in Tiedje et al. (2012), however the Ekman transport was only briefly discussed. Since we don't use a coupled model, we can only use the meridional wind stress from GECCO's optimized forcing to calculate the Ekman transport. To calculate AMOC-Ek for the ensemble simulations, every ensemble member is reduced by the Ekman transport of its respective 10-year forcing period. In a coupled model, the atmospheric feedback from the ensemble simulations would influence the Ekman transport, and this might lead to a different PPP structure than we find for the ocean-only model.

Based on the present analysis in an oceanic state estimate, the basin-wide AMOC can be potentially predicted pre-dominantly relying on capturing the thermal wind variability from observations. However, since we assess the presented results only with the assumption of (nearly) perfectly measured boundary densities in time (monthly means) and space (depth and latitude), the implementation of the required observational system would be challenging. Following previous observing system design studies, it would be useful to test, how many densities measurements in space and time are at least required to asses the presented PPP structure of the TW.

3.5 Conclusions

Based on the analysis of the North Atlantic thermal wind transport's variability (TW) in the GECCO oceanic state estimate, and the prognostic potential predictability (PPP) of the TW and the AMOC in hindcast ensembles generated using GECCO, we conclude that:

- We confirm earlier results that, across the whole North Atlantic, the density gradient and thus the TW controls the main features of the AMOC minus the Ekman transport variability (AMOC-Ek).
- The PPP structure of the total AMOC cannot be directly concluded from the PPP structure of the TW without considering the regional influence of the Ekman transport on the AMOC variability.

- The TW and the AMOC-Ek show similar PPP structures as the depth-integrated density gradient, with a maximum of predictability lead times around 40°N and decreasing potential predictability to the north and south.
- The contributions to the TW's variability are spatially and temporally separated: the seasonal variability originates to larger parts from the eastern boundary densities than from the western, while the inter-annual variability mainly originates from the upper ~1700m of the western boundary.
- The variability of the upper western boundary densities is sufficient to reconstruct most of the total TW's PPP structure, while the influence of the lower western boundary densities and the eastern boundary densities on the inter-annual potential predictability is small.

Acknowledgments This study is supported through the Cluster of Excellence 'CliSAP' (EXC177), University of Hamburg, funded through the German Science Foundation (DFG).

4. POTENTIAL PREDICTABILITY QUANTIFIED WITH ANOMALY CORRELATION

4.1 Introduction

To test whether our conclusions on the potential predictability depend on the PPP measure used in the previous chapters, I introduce here the anomaly correlation as a second potential predictability measure. In chapter 2.4 I briefly mention that the results calculated with the anomaly correlation generally confirms our results calculated with the PPP measure. The investigations that led to this statement were, however, in an early state and needed more work that is now presented in this chapter. Note that only the quantities investigated in Tiedje et al. (2012; chapter 2) are tested with the anomaly correlation.

Several different approaches to quantify potential predictability of ensemble experiments can be found in the literature (cp. chapter 1.2). Collins (2002) used and compared three different potential predictability measures: the anomaly correlation (which differs from the anomaly correlation I will use here), the PPP measure and the root mean square error (RMSE). Collins concluded that "... there is no universally defined [prediction] skill standard. Hence the reader is free to interpret these measures of potential predictability as they wish.". In contrast, Murphy (1988) concluded in his study on the mean square error and their relationships to the correlation coefficient that a correlation coefficient as the only forecast measure ignores important types of biases in the forecast. Thus, it is always desirable to test two forecast measures instead of one. However, in more recent ensemble experiment studies, authors usually settle for one potential predictability measure, which is selected according to the respective research questions. But since the different measures require very different sets of model simulations, one is left with the impression that the experimental setup is designed to suit the chosen measure.

Here, I use the PPP measure following Pohlmann et al. (2004), which goes originally back to Collins and Allen (2002), and the anomaly correlation following Pohlmann et al. (2009). Other ensemble predictability studies that used the PPP or a PPP-like approach (based on variance ratios, originally going back to ANOVA) use long-time-scale reference simulations (50 to >100 years) and often multi-decadal ensemble experiments (e.g., Rowell, 1998; Collins and Allen, 2002; Collins, 2002; Boer, 2004, 2009; Msadek et al., 2010). The research questions in these studies focus in general on the respective model's (upper) limit of potential predictability in long-time-scale experiments, including the analysis of climate predictability and climate change predictability. It is also of interest which regions show the best potential for predictability in regard to (future) observation systems. Further, the PPP measure is also used for systematic studies on the dependence of potential predictability on the model formulation, the initial conditions or the boundary conditions of the experiment.

In contrast, the anomaly correlation is used for ensemble predictability experiments around 10 years of simulation time (e.g., Chen et al., 2010; Matei et al., 2012a). These studies often focus on the predictive skill on short time scales and how to improve it by testing initialization techniques and boundary conditions. (If the actual predictive skill is tested, the ensemble experiment periods are limited due to short observational records.) But the studies aim also to provide insight in causes leading to predictability.

Both, the PPP measure and the anomaly correlation formally quantify potential predictability. But the resulting calculated potential predictability needs to be interpreted differently. The PPP measure tests if the spread of the ensemble members (possible oceanic states) lies within the variance of the reference run. The PPP measure does not provide any information about the agreement between the temporal evolution of the ensemble members and the temporal evolution of the reference run. In contrast, the anomaly correlation tests whether the temporal evolution of the reference run can be reproduced with the ensemble means. The temporal behavior of the ensemble members as a whole, the spread within the ensemble, is not considered by the anomaly correlation measure. In general, the PPP measure offers more independence in terms of the starting dates for the ensemble setup, while the anomaly correlation needs successive starting dates. Given these differences between both measures, it is not trivial that the analysis of the present ensembles with the anomaly correlation achieves similar results as the analysis with the PPP measure.

In this chapter, I first describe how the anomaly correlation and the significance limit (the critical correlation coefficient) is calculated by means of the total MHT. Second, as noted above, the potential predictability is equally calculated for all quantities investigated in Tiedje et al. (2012; chapter 2). Third, I give a short conclusion on the potential predictability results generated with the anomaly correlation measure and the PPP measure and on the question if it makes sense to combine the two measures in the following chapter.

4.2 Method

The potential predictability of the ensemble experiments (described in chapter 2.2.2) is measured in terms of the the anomaly correlation as a function of lead time t, $ac(t)$ (Pohlmann et al., 2009):

$$ac(t) \quad = \quad \frac{\sum_{i=1}^{N}\left[\tilde{x}_i(t)-\bar{x}_i\right]\left[r_i(t)-\bar{r}_i\right]}{\sqrt{\sum_{i=1}^{N}\left[\tilde{x}_i(t)-\bar{x}_i\right]^2\sum_{i=1}^{N}\left[r_i(t)-\bar{r}_i\right]^2}}, \tag{4.1}$$

with

$$\bar{x}_i = \frac{1}{T}\sum_{t=1}^{T}\tilde{x}_i(t) \qquad \text{and} \qquad \bar{r}_i = \frac{1}{T}\sum_{t=1}^{T}r_i(t),$$

where N is the number of ensembles (here, $N = 10$), T is the number of lead times (here, $T = 10$), $\tilde{x}_i$ is the mean of the ith ensemble, and r_i is the reference run starting in the same year as the ith ensemble. This calculation is carried out for each latitude from 0° to 60°N. To avoid artificial predictability the reference run and the ensemble means are detrended and averaged to annual means prior to the anomaly correlation analysis. An overview of the anomaly correlation measure is given in Figure 4.1.

An anomaly correlation value of 1 indicates perfect potential predictability, whereas a value below (or equal to) 0 indicates no potential predictability. In order to derive a statistical significance and therewith an interpretable spatial structure of anomaly correlation values, a critical correlation value is calculated for every latitude in two steps:

1. An effective number of observations n_{eff} (degrees of freedom) is calculated by using the lagged autocorrelations of the respective time series of the ensemble means and the reference run for every lead time (e.g., Jungclaus and Koenigk, 2010; von Storch and Zwiers, 1999):

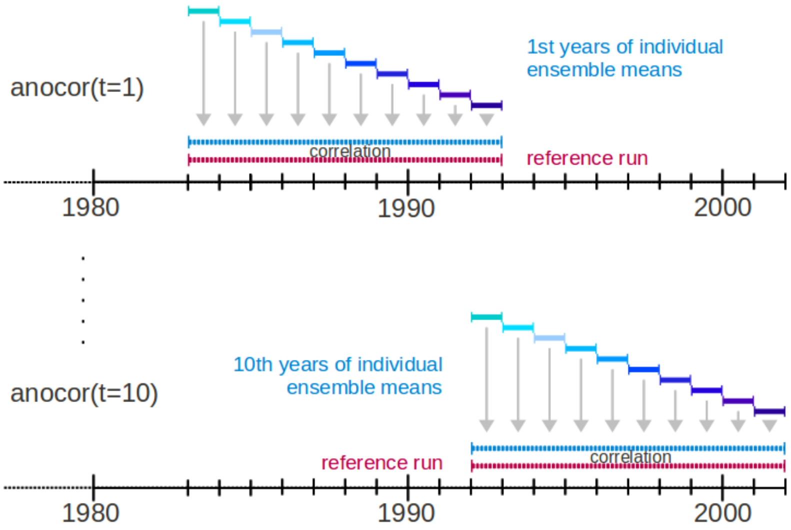

Fig. 4.1: Overview of the anomaly correlation method. The upper panel shows how the anomaly correlation value for the first lead time is calculated from the correlation between the ensemble means (first years) and the reference run. The lower panel shows the same for the 10th lead time. (The coloring of the individual ensembles and the reference run is based on Figure 2.1.)

$$n_{eff} \quad = \quad n/\left[1+2(\rho_1^x\rho_1^r+\rho_2^x\rho_2^r+\ldots+\rho_n^x\rho_n^r)\right], \tag{4.2}$$

where n denotes the sample size (length of the correlation time series) and ρ_1^x and ρ_1^r are the lag-1 autocorrelations of the two time series, ρ_2^x and ρ_2^r are the corresponding lag-2 autocorrelations and so on. The denominator of equation 4.2 gives the decorrelation time.

2. Since only positive correlations indicate predictive skill, respectively potential predictability, the critical correlation coefficient ccc at the significance level α is estimated using a one-sided t-test (for every lead time; following Sachs, 1997):

$$ccc \quad = \quad \sqrt{t^2_{n_{eff},\alpha}/\left[n_{eff}+t^2_{n_{eff},\alpha}\right]}, \tag{4.3}$$

where $t_{n_{eff},\alpha}$ is the Student's t inverse cumulative distribution function using the degrees of freedom n_{eff} for the corresponding probabilities in α. The

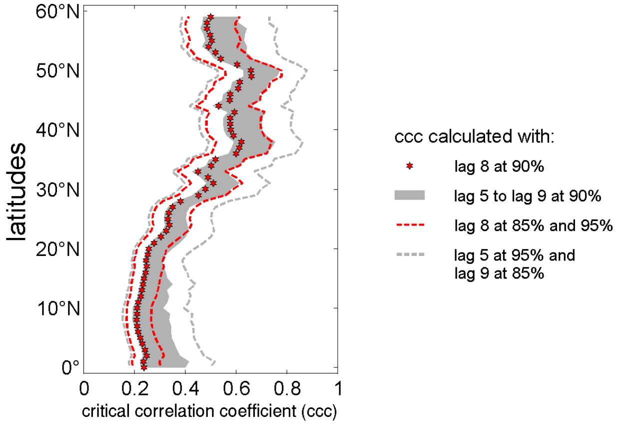

Fig. 4.2: Critical correlation coefficient (*ccc*) for the anomaly correlation of the MHT at various significance level and autocorrelation lags. The ccc is calculated at the 90% significance level with a lag-8 autocorrelation (red stars), at the 85% or 95% significance level with a lag-8 autocorrelation (red dashed lines), at the 90% significance level with a lag-5 to lag-9 autocorrelation (gray shading), and at the 95% (85%) significance level with a lag-5 (lag-9) autocorrelation (gray dashed lines).

anomaly correlation value is statistical significant if *ac* is greater than or equal to the critical correlation coefficient.

The overall aim with these calculations is to find a balance between a statistically sound solution and the preservation of the spatial structure that can already be seen without cutting insignificant values. The short time series together with the interdependence of the ensemble members make it actually impossible to find a totally sound statistical solution. But by reasonably choosing of parameters, the obvious anomaly correlation results can be statistically supported.

In principle, a critical correlation coefficient could be calculated at every latitude and for every lead time. Here, I assume that for a specific latitude the degrees of freedom stay more or less constant over the lead times and I take the median of the the degrees of freedom to calculate a critical correlation coefficient for every latitude. Figure 4.2 shows the median of the critical correlation coefficient of the MHT for different numbers of lags in the decorrelation time calculations (lag-5 to lag-9) and at different significance levels (85%, 90% and 95%). The critical correlation coefficient is higher at the subpolar latitudes (∼0.5-∼0.6) than at the subtropical latitudes (∼0.3-∼0.4). This structure is similar for all investigated lags and significance levels. For the MHT as well as for all forthcoming quantities I use a significance level of 90% and limit the decorrelation time calculations at an autocorrelation lag of 8 lead times (red stars and red dashed curves in figure 4.2). To remain consistent with the significance calculations for the PPP measure, I average the critical correlation coefficients over the latitudes. For comparison, the significance limit calculations for the anomaly correlation result in 0.4 for the MHT and 0.55 for the AMOC, whereas the significance limit calculations for the PPP result in 0.4 for the MHT and 0.45 for the AMOC.

To test if the assumptions and simplifications cut the "right" insignificant correlation values, I now compare the Hovmöller plots of the MHT's potential predictability with and without cutting the anomaly correlation values at the critical correlation coefficients (Fig. 4.3a and b). Generally, both figures show a similar spatial structure, except that the long predictable lead times are interrupted between the subpolar and subtropical gyres (∼40°N-∼45°N). In the following, *AC structure* stands for the spatial and temporal extent of the significant anomaly correlation values across the North Atlantic, and *AC predictable lead time* stands for the time period over which the anomaly correlation values are significant.

4.3 Results from chapter 2 tested with anomaly correlation

4.3.1 Potential predictability of the MHT

The AC predictable lead times of the total MHT indicate up to 9 years of potential predictability around 50°N. These long AC time scales decrease with decreasing latitudes to 3-4 years between 20°N and 30°N. In comparison to the PPP structure of the MHT (Fig. 2.3 or gray dashed lines in Fig. 4.3b), I find good agreement in the subtropical gyre and between 50°N and 60°N. The location of maximum potential predictability (around 50°N) is similar as well. But at most latitudes between 35°N and 50°N the AC predictable lead times are much longer than the predictable lead times calculated with the PPP measure. Additionally, the gap between the subpolar and subtropical latitudes is much less apparent and shifted about 5° to the north.

4.3.2 Influence of the MHT components, velocity and temperature field variations

As in chapter 2.3.2, I continue the potential predictability analysis by decomposing the MHT into the overturning and the gyre component (Fig. 4.4a and d). As the PPP structure of the MHT, the AC structure of the MHT can be reconstructed from

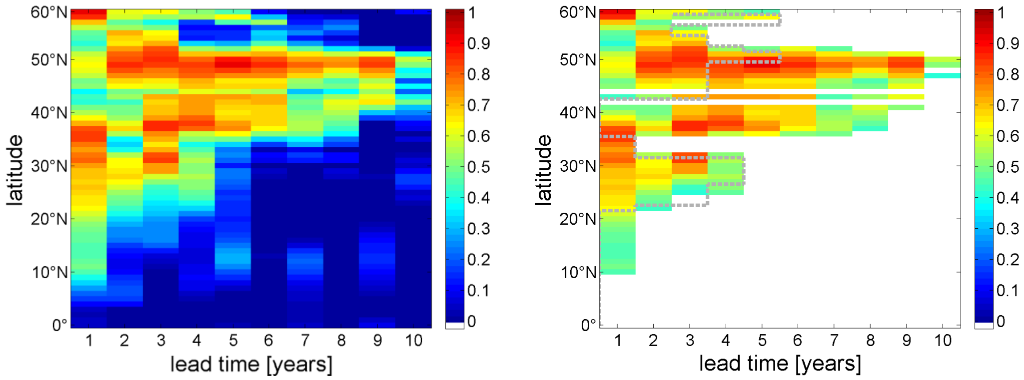

(a) **(b)**

Fig. 4.3: (a) Hovmöller diagram of the potential predictability of the MHT as a function of lead time quantified with anomaly correlation (Atlantic 0° - 60°N). (b) Same as (a) but at the 90% significance level. The gray dashed line in (b) indicates the PPP significance limit.

both components. At the subtropical latitudes, the AC structure can be explained with the contributions from the overturning component, whereas at the subpolar latitudes the AC structure can be explained with the contributions from the gyre component. In their respective areas of influence both components show slightly longer AC predictable lead times than the total MHT (Fig. 4.3b). Additionally, the anomaly correlation values of the components are higher. In comparison to the PPP, the predictable lead times of the gyre component agree quite well, whereas the predictable lead times of the overturning component are longer north of 35°N for the anomaly correlation, and the gap between the gyres seems to be shifted to the north as for the total MHT.

The spatial separation of the contributions becomes even more obvious when we allow the total MHT signal for the reference run instead of the respective component's signal (Fig. 4.4b and e). It is, however, noticeable that this method of opposing the MHT components of the ensemble to the total MHT of the reference run has to be interpreted differently for the anomaly correlation and for the PPP measure. Where no limitation of potential predictability with the PPP measure can be found (because the ensemble spread stays smaller than the variance of the reference run), I conclude that the respective component has no significant influence on the total MHT's potential predictability. In contrast, the way of interpreting the results of the anomaly correlation measure stays the same as for opposing the MHT components of the ensemble to the MHT components the reference run. Nevertheless, it can be concluded from both measures and approaches that the overturning component has more influences on the potential predictability of the total MHT at subtropical

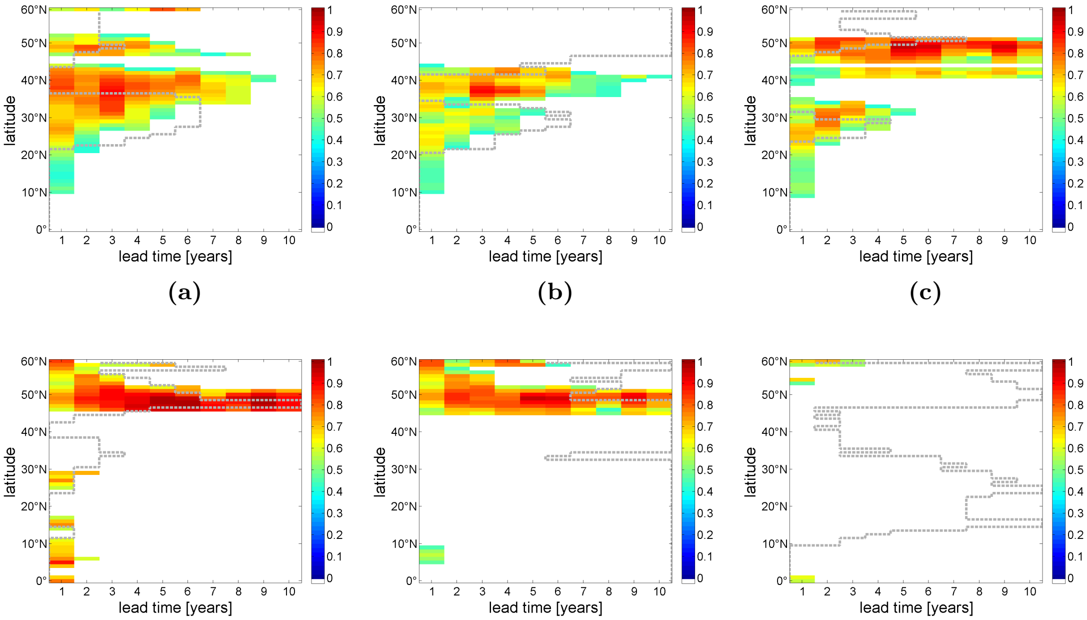

(a) (b) (c)

(d) (e) (f)

Fig. 4.4: Hovmöller diagram of the potential predictability as a function of lead time quantified with anomaly correlation at the 90% significance level of the following quantities (Atlantic: 0° - 60°N): (a) the overturning component of the MHT, (b) the overturning component of the MHT tested against the full reference MHT signal, (c) the MHT calculated with a constant mean temperature field tested against the full reference MHT signal, (d) the gyre component of the MHT, (e) the gyre component of the MHT tested against the full reference MHT signal, and (f) the MHT calculated with a constant mean velocity field tested against the full reference MHT signal. The gray dashed lines indicate the PPP significance limits.

latitudes and the gyre component has more influence at the subpolar latitudes.

Following chapter 2.3.3, I now estimate the influence of the velocity (temperature) field on the potential predictability of the MHT by holding the velocity (temperature) field temporally constant for the ensembles but keeping the full MHT signal for the reference run (Fig. 4.4c and f). Especially at the subtropical but also at the southern subpolar latitudes, the variations of the velocity field alone (Fig. 4.4c) seem to be sufficient to reproduce the AC structure of the total MHT. As for the total MHT, the AC structure and the PPP structures agree particularly well in the subtropical gyre.

In contrast, the calculations for the MHT using a temporally constant velocity field and a varying temperature field show no significant potential predictability (Fig. 4.4f). In chapter 2.3.3, I concluded for the PPP measure that the influence of

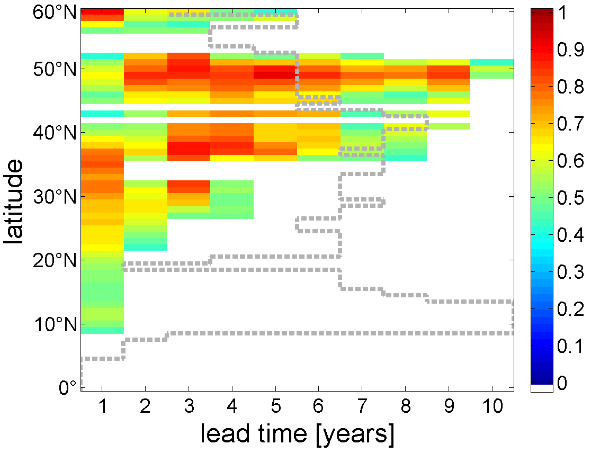

Fig. 4.5: Hovmöller diagram of the potential predictability as a function of lead time quantified with anomaly correlation at the 90% significance level of the MHT minus the Ekman heat transport tested against the full reference MHT signal (Atlantic: 0° - 60°N). The gray dashed line indicates the PPP significance limit.

the temperature variations is mostly restricted to the vicinity of the gyre boundary, where the temperature field variations reduce the ensemble spread and lengthen the PPP time scales of the total MHT. From the result of the anomaly correlation, I can only draw the rather general conclusion that the temperature variations alone do not correlate with the total MHT variations. I assume that temperature variations might also have a limiting effect on the AC predictable lead times at the southern subpolar latitudes, since the AC predictable lead times of the velocity variation analysis are longer at these latitudes than those of the total MHT.

4.3.3 Influence of the Ekman heat transport

The influence of the wind field is estimated by subtracting the Ekman heat transport from the MHT prior to the anomaly correlation analysis. As for the PPP, the MHT minus the Ekman heat transport is tested against the total MHT signal for the reference run (Fig. 4.5). In contrast to the PPP structure, the AC structure does not change significantly between the MHT structure and the MHT minus the Ekman heat transport structure.

4.3.4 Potential predictability of the AMOC

The anomaly correlation of the AMOC shows isolated short AC predictable lead times of about 2 years at the subpolar latitudes and longer AC predictable lead times of 8 years around 40°N and of 3 to 4 years at the subtropical latitudes (Fig. 4.6).

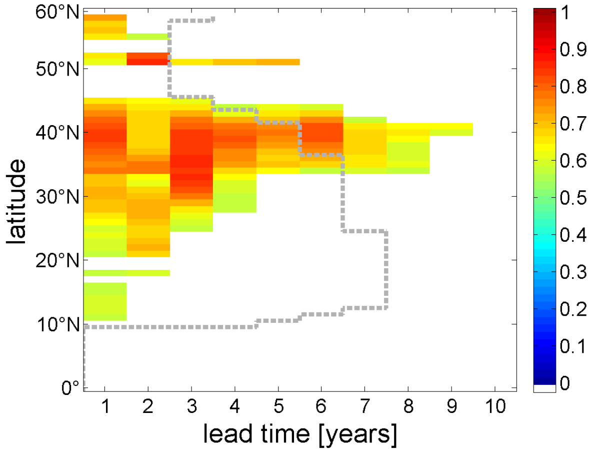

Fig. 4.6: Hovmöller diagram of the potential predictability of the AMOC as a function of lead time quantified with anomaly correlation at the 90% significance level (Atlantic: 0° - 60°N). The gray dashed line indicates the PPP significance limit.

Especially in the subtropics, the AC predictable lead times are significantly shorter than the PPP predictable lead times. The PPP structure shows decreased PPP values around 40°N (Fig. 2.8) while the anomaly correlation structure shows a gap of potential predictability further north (45°N-50°N).

Despite these differences, I come to the same conclusion for both measures: The spatial structure of shorter AMOC predictable lead times at subpolar latitudes than at subtropical latitudes is more comparable to the overturning component of the MHT than to the total MHT. Therefore, the predictable lead times of the AMOC are only similar to the predictable lead times of the MHT where the overturning component controls the predictable lead times of the MHT (subtropical latitudes).

4.4 Concluding remarks

The aim of this chapter was to test the robustness of the results from Tiedje et al. (2012) (chapter 2) with a second potential predictability measure. The anomaly correlation was introduced and applied to all quantities investigated in chapter 2.

Although the AC and PPP structures do not always agree in all details, most of the dynamic conclusions appear robust with respect to both the ensemble spread (PPP) and the degree of linear association between the hindcast ensembles and the reference run (anomaly correlation). Both measures show that the MHT's potential predictability structure can be reconstructed from the potential predictability structure of its dynamical components. Further, a transition from the overturning component dominated region (subtropical latitudes) to the gyre component dominated region (subpolar latitudes) can be seen with both measure, although the region of transition is not spatially consistent. Around 40°N, maximum AC predictable lead times occur, where a gap of potential predictability is present in the PPP structure. The AC structure also shows a gap of potential predictability, but it is significantly smaller and shifted to the north by about ∼5°.

It seems that the transition from the subtropical to the subpolar gyre is detected differently by the anomaly correlation and the PPP measure. While with the PPP measure the spread grows bigger than the variance of the reference run (∼40°), the anomaly correlation method does still detect good correlation between the ensemble means and the reference run. But only ∼5° further north, the gyre transition also affects the agreement of the temporal evolution, resulting in small correlation coefficients. The gyre boundary is a region of high variability and it spatially shifts during the investigated period. I assume that although the input data for the anomaly correlation analysis are detrended, the ignorance of biases could lead to an overestimation of the potential predictability at the gyre boundary. Overall, due to the high variability and dynamical complexity in the region around the gyre boundary (∼40° and ∼50°), one should be cautious to draw conclusions on the potential predictability here.

The PPP analysis of the MHT minus the Ekman heat transport seems intuitive at first sight, since we find longer predictable lead times at all latitudes if we subtract the Ekman variability from the ensemble simulations (chapter 2.3.4). On the other hand, the nearly unchanged AC structure of the MHT minus the Ekman heat transport is a surprising result. So, we do find a limiting effect of the Ekman dynamics on the potential predictability with the PPP measure, but not with the anomaly correlation. Possibly, the Ekman transport influences the total amount of variability (ensemble spread; PPP) more severe than the linear association (temporal evolution; anomaly correlation) on inter-annual time-scales.

Another point that can be discussed is the influence of the temperature variations on the potential predictability of the MHT and its different representation in the PPP and AC structure (chapter 4.4). For the PPP measure, we argue that the potential predictability time scales are longer at subpolar latiudes because the increased influence of the temperature field reduces the spread of the ensembles (chapter 2.3.3).

For the anomaly correlation, the approach of holding the velocity field constant for calculating the MHT and test the resulting signal against the full MHT signal cannot be interpreted as straightforward as for the PPP measure. I assume that there is simply too little variability left that can correlate well with the full signal of the MHT, and thus the variation of the temperature field leaves no trace in the anomaly correlation plot (Fig. 4.4f).

The predictable lead times of both the anomaly correlation and the PPP analysis can be influenced by a different choice of the parameters that set the statistical significance limit (chapter 4.2). Despite the efforts to make the anomaly correlation and PPP measure comparable in terms of the statistical interpretation, the predictable lead times vary between the two measures, and insisting on a specific number of predictable years would not be helpful. After all, the PPP measure and the anomaly correlation are two independent measures of potential predictability.

In chapter 2.2.3 we have shown that there is essentially no predictability inherent in the experimental setup for the PPP measure, although the reference period (1959-2001) was forced with the same optimized forcing as the ensemble members. The reference period of the anomaly correlation is naturally the hindcast period (1983-2001), whose optimized forcing was not used to generate the ensemble members. Thus, from this point of view, the anomaly correlation would be the preferable potential predictability measure. However, the use of a variance-based and a correlation-based potential predictability measure provides also new insights and may modify the conclusions. Further, the use of both measures in combination could prevent us from too optimistic predictable lead times that could result from a high correlation concealing an offset (bias) or a small spread concealing no linear association between the ensembles and the reference run.

In the following, I briefly summarize the conclusions from the analysis of the potential predictability quantified with the anomaly correlation and the PPP measure:

- The PPP measure is useful to estimate whether the hindcast variability (ensemble spread) lies within the variance of the reference run which comprises several different oceanic states.
- The anomaly correlation is useful to estimate whether the temporal evolution of the reference run's hindcast period can be reproduced by the ensemble means.
- Either measure can be used to estimate a dynamical component's influence on

the potential predictability of the total quantity (by dynamical decomposition). The PPP measure is preferential to estimate the limiting effect of an individual component's variability on the potential predictability of the total quantity (by holding one individual component constant and opposing it to the full signal).

- Although the anomaly correlation and the PPP measure do not show the same potential predictability lead times, the agreement of both measures in terms of the dynamic conclusions strengthens the robustness of these conclusions.

The prospect to benefit from a joint analysis of both measures' predictability criteria (significant correlation and ensemble spread) motivates the combination of both measures in the next chapter.

5. ON THE RELATION OF THE POTENTIAL PREDICTABILITY OF THE AMOC AND THE MHT[1]

Abstract
The latitude-dependent potential predictability of the North Atlantic meridional overturning circulation (AMOC) cannot be directly transfered to that of the meridional heat transport (MHT; Tiedje et al., 2012). To further understand the dynamical relation between both quantities we analyze hindcast ensembles based on an oceanic state estimate using two potential predictability measures. The latitude-dependent structures show that only the geostrophic parts of the AMOC's and the MHT's potential predictability are related. For the geostrophic part of both quantities and for both measures, a robust potential predictability structure of maximum predictable lead times around the gyre boundary can be found.

---

[1] Chapter 5 is in preparation for submission to *Geophysical Research Letters*. The chapter is therefore written as a stand-alone journal publication. In contrast, chapter 4 is not intended for independent publication. Hence, chapter 5 draws from chapter 4, but only makes references to published literature.

5.1 Introduction

The North Atlantic meridional overturning circulation (AMOC) and the meridional heat transport (MHT) are thought to be closely linked (e.g., Pohlmann et al., 2006), but their connection is not straight forward. In addition to wind stress and the density gradients that dominantly drive the AMOC, the MHT is driven by the air-sea fluxes that set the temperature distribution. Thus changes in MHT across different climates cannot be explained exclusively in terms of changes in the AMOC (Ferrari and Ferreira, 2011). Also, a long-term decrease in the AMOC does not necessarily have to be followed by a decrease in MHT (Drijfhout and Hazeleger, 2006).

Both the AMOC and the MHT have been studied in separate predictability studies. For the AMOC, several idealized potential predictability studies (e.g., Griffies and Bryan, 1997; Collins and Sinha, 2003; Pohlmann et al., 2004; Collins et al., 2006; Hermanson and Sutton, 2009; Msadek et al., 2010) and initialized (potential) predictability studies (e.g., Keenlyside et al., 2008; Pohlmann et al., 2009; Matei et al., 2012a; Kröger et al., 2012; Pohlmann et al., 2013) have focused on the analysis of individual latitudes (except for Kröger et al. (2012)). None of these studies focused on understanding the latitude-dependence of the AMOC's potential predictability. For the MHT, we analyzed the latitude-dependence in an earlier paper (Tiedje et al., 2012), but did not focus on the relation of the MHT's and AMOC's latitude-dependent potential predictability.

To analyze the latitude-dependence of the AMOC's and MHT's predictability, we have to turn to model simulations not only for the hindcast simulations, but also for the verification of the hindcasts as present observations of the AMOC and MHT are limited to 26.5°N and at 41°N (Cunningham et al., 2007; Willis, 2010; Johns et al., 2011; Hobbs and Willis, 2012).

Here, we analyze the potential predictability in a set of hindcast ensembles which benefit from the initialization from an oceanic state estimate (as suggested by e.g., Collins, 2002). The quantification of potential predictability also benefits from this oceanic state estimate due to its dynamical consistence with observations and thus its improved representation of oceanic variability. To quantify the potential predictability of the AMOC and the MHT, we use two common potential predictability measures, of which one is correlation based (anomaly correlation; Pohlmann et al., 2009) and one is variance based (prognostic potential predictability; Pohlmann et al., 2004). The combined use of these two measures of potential predictability tests for both correct phasing and magnitude of variability in the hindcast simulations.

5.2 Model and methods

We base our analysis on the oceanic data assimilation product GECCO (German partner of the consortium for Estimating the Circulation and Climate of the Ocean; Köhl and Stammer, 2008). We use a slightly corrected version of the GECCO synthesis' optimized forcing to generate a 50-year integration, covering the same period as the original GECCO run (1952-2001). This integration represents the reference run for both potential predictability methods and provides the initial conditions for the ensemble generation. We initialize 10 ensembles from the reference run starting one year apart (1983, ..., 1992). The ensemble members are generated using different 10-year periods of GECCO's corrected optimized atmospheric forcing between 1959 and the respective initial condition start date. The setup results in ten 10-year ensembles at 15 to 24 members. Prior to the potential predictability analysis, the data are detrended and annually averaged. Further details of the experimental setup can be found in Tiedje et al. (2012).

To analyze the AMOC and MHT, we remove the wind-driven variability from both quantities. For the AMOC, we remove the depth-dependent Ekman transport that is corrected to ensure no net meridional mass transport related to the zonal wind stress (following e.g., Baehr et al. (2004)). For the MHT, we remove the Ekman heat transport following Jayne and Marotzke (2001). We calculate the geostrophic part of the AMOC from the thermal wind balance (Hirschi and Marotzke, 2007). The thermal wind transport is calculated from the eastern and western boundary densities and corrected to hold mass balance. At every latitude between 0° and 60°N, the boundary densities are taken directly at the continental slope (e.g., Kanzow et al., 2009), except for the Gulf of Mexico and the Caribbean Sea, which are topographically separated from the basin (∼10°N and ∼30°N), where we only consider the mid-ocean transport. We calculate the geostrophic part of the MHT from decomposing the the MHT into an overturning and a gyre component (Bryden and Imawaki, 2001). The overturning component is based on the zonally averaged meridional flow, from which we remove the Ekman heat transport to derive the geostrophic part of the MHT.

Two measures are used to quantify the potential predictability of the AMOC and MHT: anomaly correlation (AC; Pohlmann et al., 2009) and prognostic potential predictability (PPP; Pohlmann et al., 2004). AC tests whether the temporal evolution of the reference run can be reproduced with the ensemble means. For the AC, we estimate the significance limit using a t-test (e.g., von Storch and Zwiers, 1999; Jungclaus and Koenigk, 2010; Sachs, 1997). In contrast, PPP tests if the spread of the ensemble members (possible oceanic states) lies within the variance of the reference period. PPP does not provide any information about the agreement between the temporal evolution of the ensemble members and the temporal evolution of the reference run. We define the reference period for the PPP calculation from 1959 to 2001 (cp. Tiedje et al., 2012) and estimate the significance limit using an F-test (Pohlmann et al., 2004).

For both metrics a value of 1 indicates perfect potential predictability and a value below 0 indicates no potential predictability. In the following, *AC* or *PPP structure* stands for the spatial and temporal extent of the significant values across the North Atlantic, and *AC* or *PP predictable lead time* stands for the time period over which the values are significant.

Given the different characteristics, we do not expect that both measures necessarily show the same potential predictability results. Here, we assume that potential predictability in the given model environment is more robustly estimated, if both measures indicate significant potential predictability. Thus, we particularly focus on the potential predictability structure that forms from the overlap of AC's and PPP's predictable lead times and satisfies both the ensemble spread criterion as well as the correlation criterion (*LAP structure*).

5.3 Potential predictability of AMOC and MHT

For the AMOC, both AC and PP predictable lead times are longer at the subtropical latitudes and the gyre boundary (∼40°N) than at the subpolar latitudes (Fig. 5.1a and b). In contrast, for the MHT, the AC predictable lead times are longer and the PPP values are higher at subpolar latitudes than at the subtropical latitudes, indicating the influence of the gyre component (Fig. 5.1d and e). The spatial separation between the dominant influence of the gyre component (mostly at subpolar latitudes) and overturning component (mostly at subtropical latitudes) was already shown for the PPP by Tiedje et al. (2012). Tiedje et al. (2012) also pointed out that the PPP structure of the AMOC and that of the MHT's overturning component are comparable. Both findings can be similarly transfered to the AC (not shown).

Comparing the AMOC's and the MHT's potential predictability, we find smaller differences between the two measures of potential predictability than between the

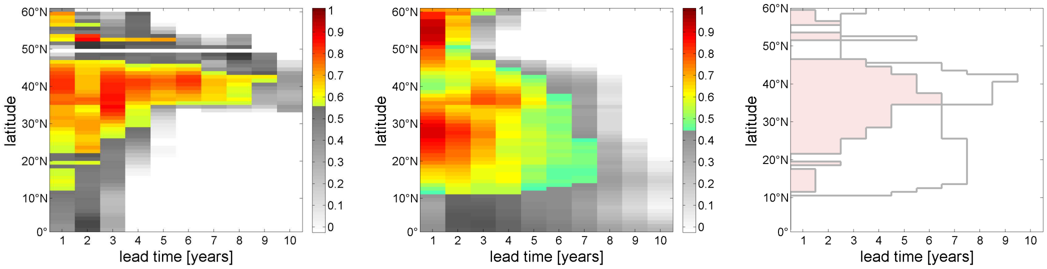

(a) AC **(b)** PPP **(c)** LAP

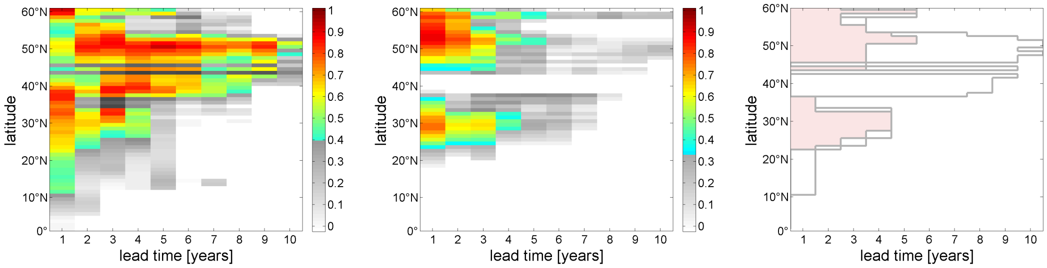

(d) AC **(e)** PPP **(f)** LAP

Fig. 5.1: Hovmöller diagrams of the potential predictability as a function of lead time in the North Atlantic (0°-60°N): (a) AMOC quantified with AC (*cp. Fig. 4.6*), (b) AMOC quantified with PPP (cp. Fig. 8 from Tiedje et al. (2012); *cp. Fig. 2.8*), (c) combination of the predictable lead times of (a) and (b), (d) MHT quantified with AC (*cp. Fig. 4.3*), (e) MHT quantified with PPP (cp. Fig. 3 from Tiedje et al. (2012); *cp. Fig. 2.3*), (f) combination of the predictable lead times of (d) and (e). The colored values in (a,b,d,e) are significant at the 90% level. The pink areas in (c,f) indicate the overlap of AC's and PPP's predictable lead times.

AMOC and the MHT. Hence, the LAP structures for the AMOC and the MHT are different. While the LAP structure for the AMOC indicates maximum predictable lead times of 5-6 years around the gyre boundary (Fig. 5.1c), the LAP structure for the MHT indicates no potential predictability at the gyre boundary and maximum predictable lead times of 4-5 years at subpolar and subtropical latitudes (Fig. 5.1f).

The subtraction of the Ekman transport from the AMOC (AMOC-Ek) shortens the AC and in particular the PP predictable lead times at several latitudes and leads to an intensification of AC and PPP values around the gyre boundary (Fig. 5.2a and b). The subtraction of the Ekman heat transport from the MHT (MHT-Ek) also results in an increase in AC and PPP values around the gyre boundary (Fig. 5.2d and e). For the AC, however, only the long predictable lead times at the subtropical latitudes (that are dominated by the gyre component) are preserved, while the predictable lead times are shorter than for the total MHT almost anywhere else (Fig. 5.2d). For the PPP, only the predictable lead times at the gyre boundary

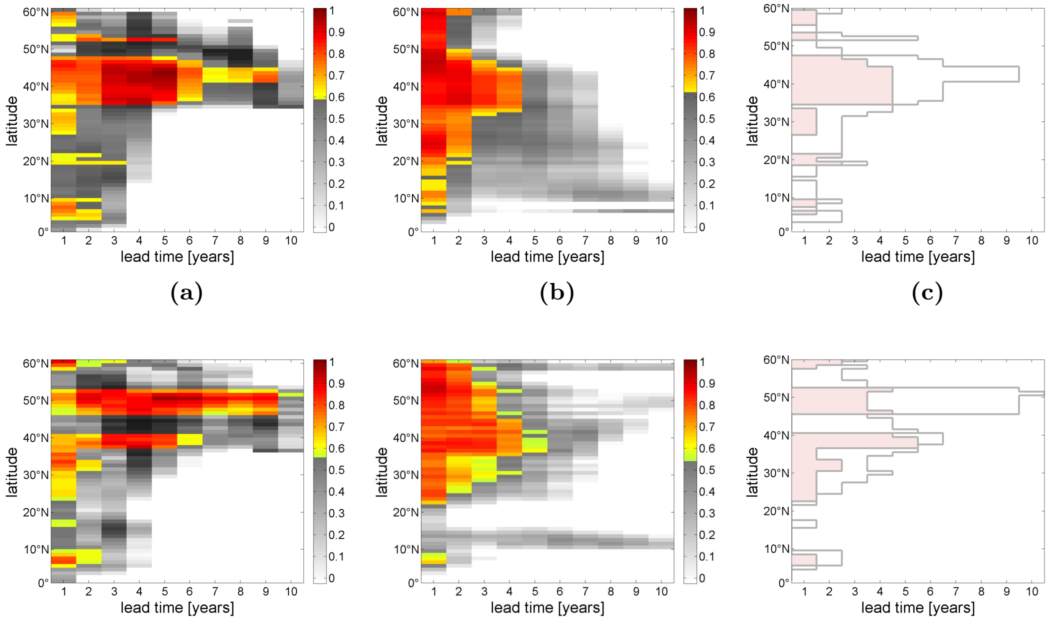

(a) (b) (c)

(d) (e) (f)

Fig. 5.2: Hovmöller diagrams of the potential predictability as a function of lead time in the North Atlantic (0°-60°N): (a) AMOC-Ek quantified with AC, (b) AMOC-Ek quantified with PPP, (c) combination of the predictable lead times of (a) and (b), (d) MHT-Ek quantified with AC, (e) MHT-Ek quantified with PPP, (f) combination of the predictable lead times of (d) and (e). The colored values in (a,b,d,e) are significant at the 90% level. The pink areas in (c,f) indicate the overlap of AC's and PPP's predictable lead times.

increase, while the predictable lead times at the subtropical and subpolar latitudes remain mostly unchanged (Fig. 5.2e).

Removing the wind-driven variability from the AMOC and the MHT leads to a seemingly similar potential predictability structure for the PPP (Fig. 5.2b and e), while the AC structures are considerably different (Fig. 5.2a and d), which is also mirrored in the differences of the resulting LAP structures (Fig. 5.2c and f). We can at this point not explain why the Ekman transport influences the predictable lead times of the AMOC and the MHT differently, and setup dependent influences cannot be excluded. We now turn to the analysis of the relation of the potential predictability structures of the AMOC and the MHT after removing the Ekman transport.

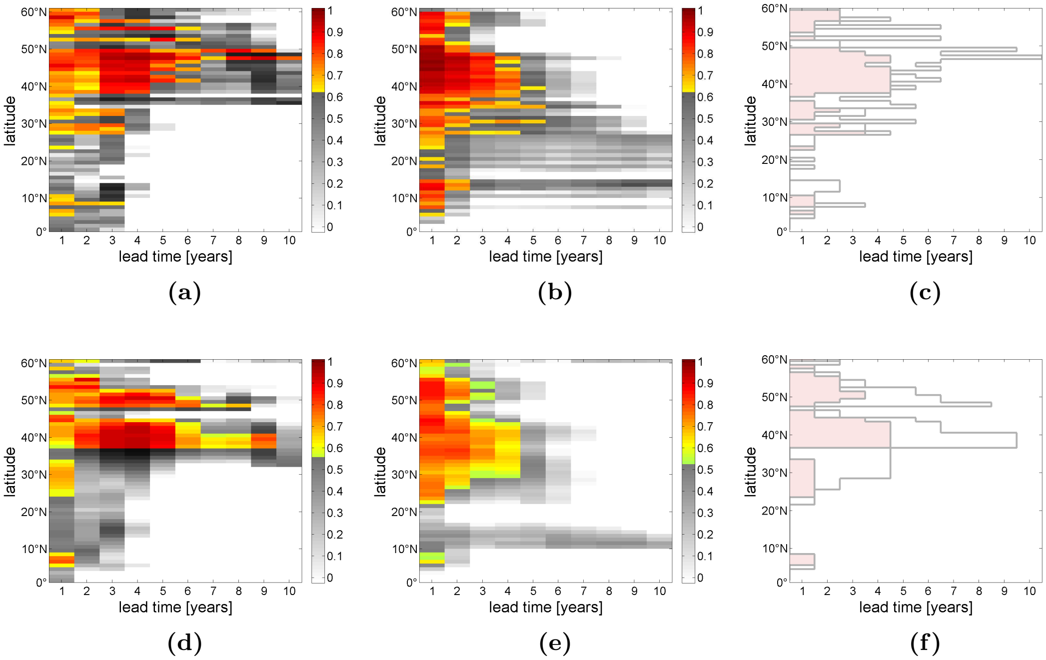

Fig. 5.3: Hovmöller diagrams of the potential predictability as a function of lead time in the North Atlantic (0°-60°N): (a) TW quantified with AC, (b) TW quantified with PPP (*cp. Fig. 3.7b*), (c) combination of the predictable lead times of (a) and (b), (d) $\mathrm{MHT_{oc}}$-Ek quantified with AC, (e) $\mathrm{MHT_{oc}}$-Ek quantified with PPP, (f) combination of the predictable lead times of (d) and (e). The colored values in (a,b,d,e) are significant at the 90% level. The pink areas in (c,f) indicate the overlap of AC's and PPP's predictable lead times.

5.4 Relating the potential predictability of AMOC and MHT

To investigate the relation of the potential predictability structures of the AMOC and the MHT, we focus on the geostrophic parts of the AMOC and the MHT respectively. For the AMOC, the geostrophic part is estimated from boundary densities through the thermal wind relation ($\mathrm{AMOC_{TWv}}$; cp. chapter 5.2). The AC and PPP structures of $\mathrm{AMOC_{TWv}}$ show maximum potential predictability at the gyre boundary and decreasing predictable lead times to the north and south (Fig. 5.3a and b). For the MHT, the geostrophic part is estimated from the overturning component with the Ekman heat transport removed ($\mathrm{MHT_{oc}}$-Ek; cp. chapter 5.2). Although the $\mathrm{MHT_{oc}}$-Ek's AC and PPP predictable lead times do not agree, we find for both measures maximum predictable lead times at the gyre boundary and decreasing predictable lead times to the north and south (Fig. 5.3d and e).

For both the $\mathrm{AMOC_{TW_V}}$ and the $\mathrm{MHT_{oc}}$-Ek, the LAP structures indicate maximum predictable lead times of about 4 years that are concentrated around the gyre boundary (Fig. 5.3c,f). The similar LAP structures suggests that AMOC's and MHT's potential predictability are only similar for their geostrophic parts.

While the $\mathrm{AMOC_{TW_V}}$'s AC and PPP structure seems generally similar to the AMOC-Ek's AC and PPP structure (Fig. 5.3a and b and Fig. 5.2a and b), the similarities between the $\mathrm{MHT_{oc}}$-Ek's and MHT-Ek's AC and PPP structures are altered by the respective metric's structure of the gyre component (Fig. 5.3d and e and Fig. 5.2d and e). While the influence of the gyre component is obvious for the MHT-Ek's AC structure, it cannot be seen for the MHT-Ek's PPP structure. These differences show that it can be misleading to derive the potential predictability of a quantity from only one measure (cf. Murphy, 1988; Collins, 2002). Although or rather because AC and PPP satisfy different predictability criteria, the combination of the correlation based and variance based measure adds value (robustness) to the found potential predictability structure in the present experimental setup.

Though we can relate the meridional LAP structures of the geostrophic component of the AMOC and the MHT, we cannot explain its origin. Specifically, it remains open to explain the dynamical origins of the presented geostrophic AC and PPP structures of AMOC and MHT with its maximum around 40°N and decreasing predictable lead times to the north and south. Potentially, southward traveling Kelvin waves modifying the variability of western boundary densities (e.g. Köhl, 2005; Köhl and Stammer, 2008), and westward propagating Rossby waves modifying the east-west density gradient (e.g. Köhl, 2005; Getzlaff et al., 2005; Hirschi et al., 2007), might be involved. But even the dynamical origin of the latitude dependence of the density gradient is not fully understood yet (Hirschi and Marotzke, 2007). In turn it is not straightforward to relate the AMOC's and the MHT's potential predictability even at a latitude where the MHT is dominated by the overturning component.

It is of course important to note that the present results are likely to be model-dependent. Similar to our findings, a coupled model hindcast experiment also shows AC structures of the AMOC and the MHT with maximum AC predictable lead times between ∼40°N and ∼50°N (D. Matei, personal communication). Both observations at additional latitudes and additional model studies will be needed to investigate the latitude-dependence of the AMOC's and MHT's predictive skill.

5.5 Conclusions

We investigate the latitude-dependent relation between the potential predictability of the AMOC and the MHT. The analysis is conducted with two potential predictability measures (anomaly correlation (AC) and prognostic potential predictability (PPP)). Based on the potential predictability structures that combine the significant predictable lead times of AC and PPP (LAP structures), we conclude that:

- The AMOC and the MHT show different LAP structures and cannot be directly compared. We hereby confirm earlier results that were found for the PPP structures only (Tiedje et al., 2012).
- The subtraction of the Ekman (heat) transport indicates some similarities between the AMOC's and the MHT's LAP structures, although they are still altered by the influence of the MHT's gyre component.
- Only the geostrophic parts of the AMOC and MHT are related in terms of potential predictability, which is shown by the similarities of the LAP structures of the thermal wind part of the AMOC and the overturning component of the MHT with the Ekman heat transport removed.

Given the limitations of the present observing system, it is an important caveat en route to predictions of the North Atlantic climate that the potential predictability of the MHT and the AMOC are neither interchangeable with each other nor to be generalized across the North Atlantic.

Acknowledgments This study is supported through the Cluster of Excellence 'CliSAP' (EXC177), University of Hamburg, funded through the German Science Foundation (DFG). We thank Daniela Matei for discussion.

6. NAO INFLUENCE ON THE POTENTIAL PREDICTABILITY OF MHT AND AMOC

6.1 Introduction

In this chapter I present preliminary results of the influence of the NAO state on the potential predictability of the AMOC and the MHT. The results are only preliminary because the present setup does not allow to clearly distinguish between the different NAO states. Nevertheless, I present the preliminary results here, as they point to interesting scientific questions which could be addressed in my future research.

The NAO refers to oscillations in the atmospheric sea level pressure difference between the Arctic and the subtropical Atlantic and primarily affects the mean wind speed and direction (e.g., Hurrell et al., 2003). These basin scale changes in the atmospheric forcing considerably influence the ocean's properties and circulation (e.g., Visbeck et al., 2003). The time scales of the ocean circulation's response range from weeks, during which an influence on SST, mixed layer depth, upper ocean heat content and Ekman transport can be found, to several years. While the heat transport is altered by the Ekman driven component within weeks, the geostrophically balanced large scale horizontal and overturning circulation response is assumed to take several consecutive years of the same NAO phase to adjust to changes in the forcing (Visbeck et al., 2003).

Several studies indicate a close connection between the NAO variability and lagged AMOC variations (e.g., Eden and Willebrand, 2001), and the general upward trend of NAO since the 1960s is associated with an increasing rather than a decreasing AMOC (Latif et al., 2006a). For the GECCO state estimate, Köhl and Stammer (2008) found that the variability of the AMOC at 48°N leads the variability at 25°N by 2 to 3 years indicating a lagged response to the high-latitude forcing variations characterized by the NAO. The adjustment of these forcing variations towards a new balanced state is established by coastally trapped (boundary) waves, equatorial

Kelvin waves and long Rossby waves (Visbeck et al., 2003; Köhl and Stammer, 2008).

Though it might be possible to predict a change in the AMOC strength based on the past NAO state, it remains the problem that the predictability of the NAO itself (particularly on time scales longer than a season) is small (e.g., Rodwell, 2003; Johansson, 2007). However, the NAO influence on a potential predictability study of the AMOC and MHT under realistic atmospheric forcing conditions seems to be inevitable. Since the NAO cannot be excluded from my present experimental setup (cp. chapter 2.4), I ask: Does the potential predictability differ between the different NAO states?

6.2 Present experimental setup

Usually, sea level pressure data is used to construct a time series of the normalized indices of the mean winter (December-March) NAO (Hurrell et al., 2003). With a correlation of ~0.99 (during 1948-2003) this NAO time series can also be constructed from the National Center for Environmental Protection - National Center for Atmospheric Research (NCEP-NCAR) reanalysis data[1]. Since the GECCO simulation is based on the forcing provided by the NCEP-NCAR reanalysis data, we assume that it is adequate to rely on this NAO state classification for our GECCO-like reference run. The NAO index changes sign a few times during the reference period, but in general the period from 1959 to 1972 is dominated by negative NAO years (NAO$^-$) and the period from 1973 to 1992 is dominated by positive NAO years (NAO$^+$, Fig. 6.1).

Since the initial conditions for the ensembles lie mainly within NAO$^+$ years, I am constrained to focus on the separation of the forcing periods into NAO$^+$ and NAO$^-$ periods for the potential predictability analysis. I will use the first five forcing periods (starting in 1959, ..., 1963; light blue in Fig. 6.1) for every ensemble to calculate the potential predictability of the AMOC and MHT during NAO$^-$ conditions. To analyze the effect of a mainly NAO$^+$ dominated period, I will use all forcing periods starting from 1972 (light red in Fig. 6.1). The setup for the NAO$^-$ conditions results in 50 members, while it results in 55 members for the NAO$^+$ conditions.

---

[1] Hurrell, James & National Center for Atmospheric Research Staff (Eds). Last modified 22 Jun 2012. "The Climate Data Guide: Hurrell North Atlantic Oscillation (NAO) Index (station-based)." Retrieved from https://climatedataguide.ucar.edu/guidance/hurrell-north-atlantic-oscillation-nao-index-station-based.

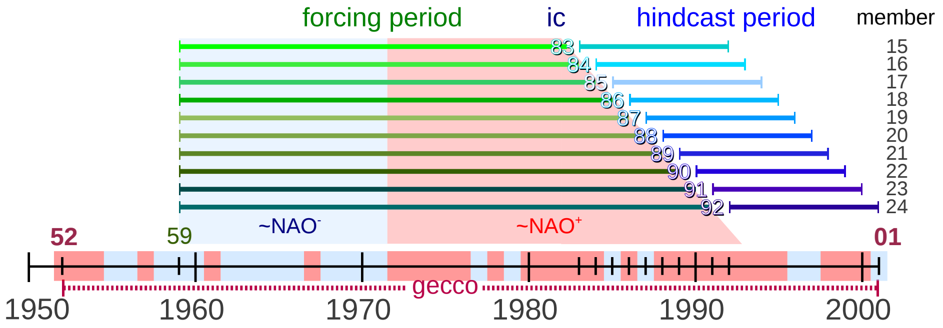

Fig. 6.1: Overview of the experimental setup (cp. Fig. 2.1) with NAO$^+$ and NAO$^-$ periods according to Hurrell et al. (2003) indicated by light red and light blue respectively.

As before, the PPP metric is used to quantify the potential predictability (chapter 2.2.3). The reference run (1959 to 2001) comprises both NAO states. The choice of the reference period as well as the bias in the number of ensemble members do not significantly change the resulting PPP structures (not shown).

6.3 Analysis of present setup

Starting with an analysis of the reference run, I find in the Hovmöller diagrams of the inter-annual AMOC and the MHT anomalies increasing positive anomalies during the second half of the reference run for both quantities, that can be related to the changing NAO state to a positive index (Fig. 6.2a and b). A detailed explanation of the AMOC structure for the original GECCO run can be found in Köhl and Stammer (2008).

To quantify the differences of the transports' strengths in the respective NAO phase, I present the composite mean of all NAO$^+$ and NAO$^-$ years (Fig. 6.2b and e). For both the AMOC and the MHT, I confirm earlier findings that the transports are stronger under NAO$^+$ conditions than under NAO$^-$ conditions. The difference between both states is larger for the AMOC than for the MHT, and reaches its maximum between 30°N and 50°N.

In anticipation of the following PPP analysis, I am particularly interested in the

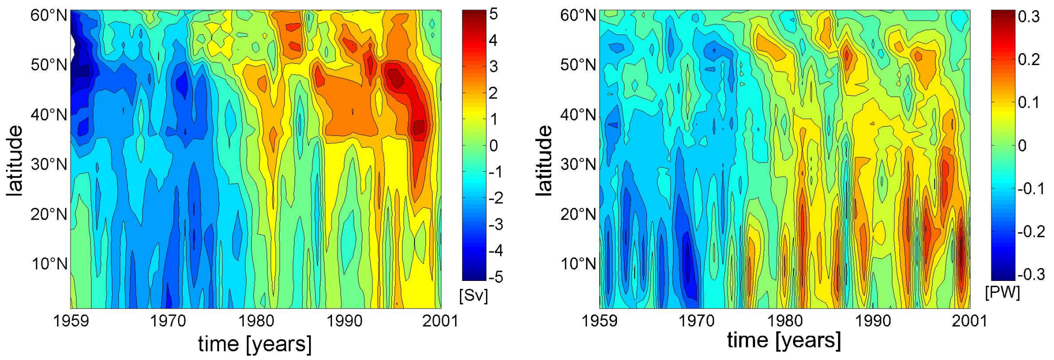

(a) AMOC **(d)** MHT

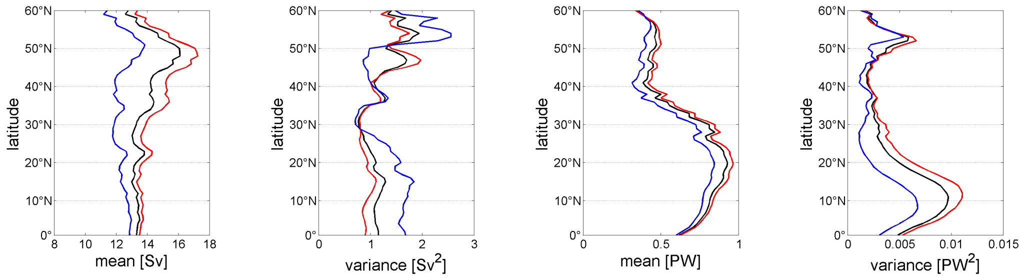

(b) **(c)** **(e)** **(f)**

Fig. 6.2: Upper row: Hovmöller diagrams of annual mean anomalies in the reference run: (a) AMOC and (d) MHT. Lower row: Latitudinal variation of the composite means (b,e) and variances (c,f) of NAO$^+$ (red) and NAO$^-$ (blue) years in the reference run (1959-2001): (b,c) AMOC and (e,f) MHT. Additionally, the means and variances of all years are shown in black (cp. Fig. 2.4a,b and Fig. 3.14a). Prior to the variance calculations, the data is detrended and annually averaged.

latitudinal variations of the composite variances of the AMOC and MHT (Fig. 6.2c and f). For the MHT, I find similar latitudinal variations for the NAO$^+$ and NAO$^-$ composites as for the total variance, with the NAO$^+$ composite exceeding the total variance and the NAO$^-$ composite showing a smaller variance. For the AMOC, the NAO$^-$ composite exceeds the total variance significantly between 50°N and 60°N and between 0° and 30°N. Whereas the NAO$^+$ composite follows closely the total variance, but exceeds the total variance only between 40°N and 50°N. The maximum variance appears to shift from ~45°N to ~55°N during a change of the NAO state. Overall, the mean and variance over both NAO states lie always between the individual estimates for one state.

I now turn to the analysis of the PPP under the influence of the different NAO states. The PPP analysis of the AMOC forced with mainly NAO$^-$ years shows shorter pre-

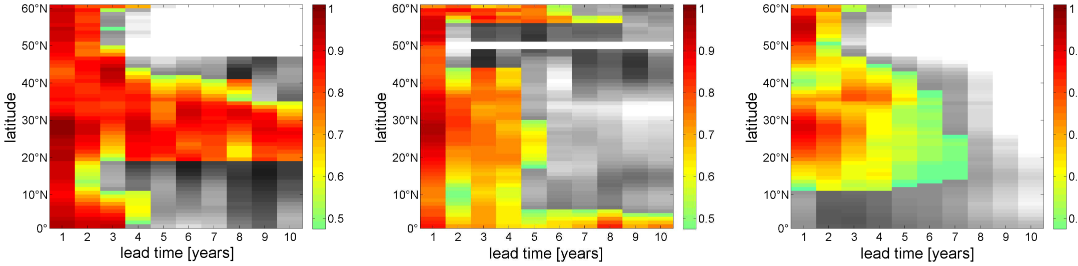

(a) (b) (c)

Fig. 6.3: Hovmöller diagrams of the PPP of the AMOC as a function of lead time: (a) only ensemble members with mostly NAO$^-$ forcing periods are used to calculate PPP, (b) only ensemble members with mostly NAO$^+$ forcing periods are used to calculate PPP, and (c) all ensemble members are used (cp. Fig. 2.8). The colored values are significant at the 90% level. Darker gray shades indicate higher PPP values than lighter gray shades.

dictable lead times at the subpolar latitudes than at the subtropical latitudes where the predictable lead times seem to be not limited between 20°N and 35°N under these NAO conditions (Fig. 6.3a). In general, this PPP structure can also be seen for the AMOC forced with mainly NAO$^+$ years, although the predictable lead times are much shorter particularly at the subtropical latitudes (Fig. 6.3b). The PPP structure of the AMOC influenced by both NAO states appears to be a mixture of the separated NAO results (Fig. 6.3c).

A first test with two single ensembles starting from different NAO states and using the corresponding NAO forcing periods shows that the resulting PPP structures seem to depend on the NAO state during the forcing period rather than on the NAO state of the initial conditions (not shown).

For the MHT, both NAO PPP structures show increased PPP values in the subpolar and the subtropical gyres, though the predictable lead times have different lengths: While under NAO$^-$ conditions the predictable lead times are longer at subtropical than at subpolar latitudes, they are shorter at subtropical than at subpolar latitudes under NAO$^+$ conditions (Fig. 6.4a and b). Surprisingly, the predictable lead times of the MHT influenced by both NAO states (Fig. 6.4c) are generally shorter within both gyres than for the NAO$^-$ and NAO$^+$ experiments. Note that this finding of shorter predictable lead times under the influence of both NAO states than under the influence of an individual NAO state is also true for the AMOC at specific latitudes.

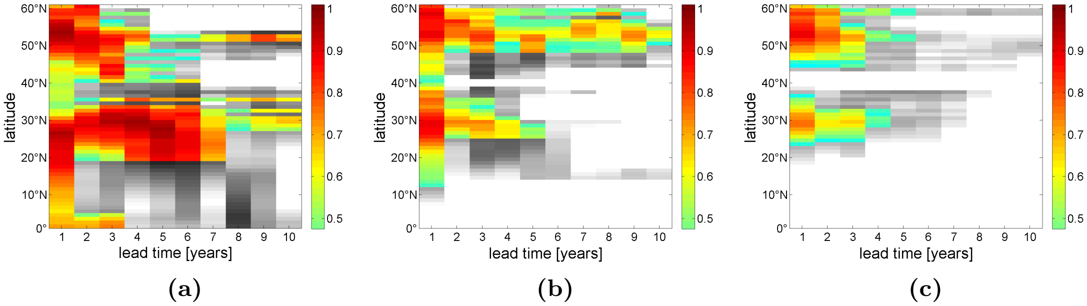

(a) **(b)** **(c)**

Fig. 6.4: Hovmöller diagrams of the PPP of the MHT as a function of lead time: (a) only ensemble members with mostly NAO$^-$ forcing periods are used to calculate PPP, (b) only ensemble members with mostly NAO$^+$ forcing periods are used to calculate PPP, and (c) all ensemble members are used (cp. Fig. 2.3). The colored values are significant at the 90% level. Darker gray shades indicate higher PPP values than lighter gray shades.

As for the MHT influenced by both NAO states (cp. chapter 2.3.2), the MHT's PPP structures with separated NAO forcings can be reconstructed from considering the PPP structures of the overturning and gyre component under the respective NAO conditions (not shown).

6.4 Future research questions and experiments

The presented results indicate an influence of the NAO state on the potential predictability of both AMOC and MHT. The results also suggest that the AMOC's and MHT's PPP structures shown in the previous chapters are not biased towards a specific NAO state. The findings for the NAO experiments, for example the regional separation of the MHT components' dominance, match our previous findings, but also raise new questions:

- Are the PPP structures the mean of both NAO conditions, or can particular features in the PPP structure be related to a specific NAO state?
- Does the NAO have a weaker projection on the meridional overturning circulation than on the gyre circulation (Bellucci et al., 2008), and thus a different effect on the PPP of the AMOC and the MHT?
- Why are the predictable lead times of the MHT with the mixed NAO forcing generally shorter than for the separate NAO forcings?

Also, it would be interesting to repeat some of the previous analysis in regard to the NAO influence, for example the influence on the Ekman variability or the density gradient.

Unfortunately, the present setup does not allow us to adequately answer these questions. The present setup is based on hindcast ensembles that are constructed to resemble a real forecast scenario such that no information is used in them that would not theoretically be available from observations at the time of the ensemble generation. To ensure an appropriate number of forcing years that do not fall in the hindcast periods, we picked the initial conditions from the later and mostly NAO$^+$ period of the reference run. Hence, it is unaccomplishable to robustly distinguish between NAO$^+$ and NAO$^-$ states when we continue to insist on the principles of a real forecast scenario.

To analyze the effect of the NAO on the AMOC's and MHT's potential predictability adequately, I would suggest to refrain from the idea of a kind of realistic forecast scenario. Staying in the ocean-only setup, I suggest to compose pure NAO forcing periods from all available NAO$^-$ or NAO$^+$ years of the reference run and add them randomly together. By picking e.g. five NAO$^-$ initial conditions and e.g. five NAO$^+$ initial conditions from the reference run, pure NAO$^-$ and NAO$^+$ ensembles could be generated. Since the main interest focuses on the behavior of the ensembles, I would continue to use the present reference run for the quantification with the PPP method. Unfortunately, the potential predictability quantification with the anomaly correlation would not be possible for the described setup, as we would need ten successive years of initial conditions to analyze ten years of predictable lead time. Note that it remains questionable, whether the available 50 years of the GECCO simulation provide a sufficient range of possible evolutions to test the NAO dependence.

On the other hand, staying in an ocean-only model setup would exclude the ocean's feedback on the NAO. It is assumed that changes of the North Atlantic SST related to variations in the deep ocean might have an effect on the atmospheric state and thus might reinforce or control the NAO state (e.g., Visbeck et al., 2003). How strong this feedback might be, is still a matter of discussion, but several model studies suggest only a modest yet statistically significant feedback (e.g., Czaja et al., 2003; Mosedale et al., 2005). However, since my initial focus would be on the question how does the effect of the NAO on the forcing periods and initial conditions alter the potential predictability, it would primarily not be advantageous to use a coupled model for the investigations. Nonetheless, for the following work it would be interesting to check the results of the elaborated ocean-only model NAO experimental setup to a similar experimental setup in a coupled model, and estimate the impact of the ocean-atmosphere feedback on the potential predictability.

7. CONCLUSIONS

I conclude this thesis on the multi-year potential predictability of the MHT and the AMOC by answering the three research questions posed in the introduction (chapter 1.3). In the course of the study further questions arose, of which two I find useful to add to the list of questions (chapters 7.4 and 7.5).

All answers are based on the same set of hindcast ensembles which are initialized from the oceanic state estimate GECCO and forced with its past optimized atmospheric conditions. The limitations concerning this experimental setup or concerning the analysis itself have already been discussed in detail in the previous chapters (chapters 2.4, 3.4, and 5.4). Specifically, I discussed the use of an ocean-only model, the input of climatic information from only a few decades, the pre-defined forcings and therefore the partly inter-dependent ensemble members, the verification of the ensembles against model simulation instead of observations, the significance of the predictable lead times, the Ekman influence, and the thermal wind calculation.

However, the advantage of the present experimental setup is that it is based on a self-consistent framework with respect to both initialization and consistency with observations. The following conclusions also benefit from the improved representation of oceanic variability in an oceanic state estimate.

7.1 Is the MHT potentially predictable? And if so, is the potential predictability of the MHT latitude-dependent?

I find that the MHT is potentially predictable on a multi-year time scale. I also find that the MHT's prognostic potential predictability (PPP) varies between the latitudes and shows specific differences between the subpolar and the subtropical gyre (chapter 2). A dynamical decomposition of the MHT in overturning and gyre component improves the understanding of these PPP differences: The overturning component plays a dominant role in the subtropical gyre, whereas the gyre component plays a dominant role in the subpolar gyre. Further, I find that also the influence of the temperature and velocity field variations on the MHT's PPP structure is latitude-dependent.

Hence, I conclude that an investigation of the MHT's potential predictability at a single latitude would not be able to provide the full picture of the potential predictability's dynamical origins, and that caution should be exercised, when interpreting the MHT's potential predictability at a single latitude.

7.2 Can the current understanding of the latitude-dependent potential predictability of the AMOC be improved by removing the wind-driven variability and focusing on the latitude-dependence of the geostrophic part?

To estimate the geostrophic part of the AMOC's potential predictability, the PPP of the AMOC minus the Ekman transport and the thermal wind transport based on boundary density gradients was calculated (chapter 3). I find that the potential predictability of the thermal wind transport provides the basis for the AMOC's PPP structure. I also find that (even on the investigated multi-year time scales) the influence of the Ekman transport variability is strong enough to conceal the direct comparability of the thermal wind transport's PPP structure to the AMOC's PPP structure. Further, excluding the variability of the eastern and lower western boundary density from the total density gradient's variability (to calculate the thermal wind transport) shows that the dynamical origins of the AMOC's potential predictability lie in the potential predictability of the upper western boundary densities. Ultimately, these findings open the prospect to use density boundary observations in combination with wind field data for estimating the potential predictability of the AMOC.

However, my analysis cannot fully explain why the predictable lead times are shorter or longer at a specific latitude. Thus, the dynamical reason for the geostrophic PPP structure of the AMOC, with a maximum around the gyre boundary and decreasing predictable lead times to the north and south, remains speculative and needs further investigations. Possibly, the limited predictable lead times at subpolar latitudes

(50°N-60°N) and subtropical latitudes (10°N-30°N) could result from propagating density anomalies (e.g., Köhl, 2005; Getzlaff et al., 2005; Hirschi et al., 2007; Köhl and Stammer, 2008; chapter 3.3.1.2).

7.3 How is the potential predictability of the MHT related to the potential predictability the AMOC?

The potential predictability of the MHT cannot be directly transfered to the potential predictability of the AMOC (chapter 2). Because of the obvious similarities between the potential predictability of the AMOC and the potential predictability of the MHT's overturning component, I conclude that the differences between the AMOC's and MHT's potential predictability can to some extent be explained by the influence of the gyre component on the MHT (particularly at subpolar latitudes).

Further, I find that only the potential predictability of the AMOC's and MHT's geostrophic parts are related (chapter 5). The geostrophic parts of the AMOC and the MHT are estimated from the thermal wind transport and the MHT's overturning component minus the Ekman variability, and show a similar potential predictability structure across the North Atlantic.

Subsequently, using density observations to estimate the potential predictability of the MHT might only be possible at latitudes where the gyre component can be neglected. Thus, an improved understanding of the relation between the AMOC's and the MHT's potential predictability will be crucial for the correct interpretation of actual inter-annual to decadal predictions based on density observations at an individual latitude.

Based on the prospect to use density and wind observations to estimate AMOC's potential predictability (chapter 7.2), potential future work could address the question of which observations would additionally be needed to estimate the MHT's potential predictability at a given latitude. For example, could SST observations help to improve the estimation of MHT's potential predictability in terms of capturing the differences to the AMOC's potential predictability?

7.4 How much information do we gain by considering two potential predictability measures?

The answer to the preceding question was found by using two potential predictability measures of which one is correlation-based (anomaly correlation) and one is variance-based (PPP). Although the predictable lead times do not agree at most latitudes, I come to the same dynamical conclusions as by analyzing the AC's and PPP's results individually (chapter 4 and 5). However, using both measures also provides the opportunity to gain new insights. For example, the influence of the gyre component on the MHT after subtracting the Ekman variability is obvious in the AC structure while its influence is hardly recognizable in the PPP structure (chapter 5.4). The concurrent consideration of both predictability measures has the advantage that an offset (bias) is not concealed by high correlation values, and that a small ensemble spread but no significant correlation leads to too optimistic predictability results. Overall, I consider the potential predictability structure resulting from the overlap of both measure's significant predictable lead times as a good way to meet two important predictability criteria.

7.5 Is the potential predictability altered by different NAO states?

The way I designed the experimental setup to resemble a realistic forecast scenario comes at the expense of mainly NAO^+ initial conditions and a mixture of NAO^+ and NAO^- forcing conditions (chapter 2.4). As a first step for potential future work, I tested the influence of the NAO state on the potential predictability of the MHT and the AMOC by rearranging the present set of hindcast ensembles into mainly NAO^+ forced and mainly NAO^- forced hindcasts (chapter 6). I find that the NAO state affects the PPP structures of the MHT and the AMOC, but also that they are not biased towards a specific NAO state. However, the structural PPP differences encourage to design an improved experimental setup to adequately analyze the influence of the NAO (chapter 6.4).

7.6 Concluding remarks

The innovation of the present study lies in the interrelation of the predictable lead times of the MHT and the AMOC throughout the Atlantic from 0° to 60°N. The insight gained from this analysis provides another piece to the puzzle of understanding the variability relation of the MHT and the AMOC and extends it to the subject of potential predictability.

However, besides the limitations of the experimental setup, the results presented here are of course model-dependent and serve therefore essentially as a reference point for the discussion of meridionally variable predictability structures. Since latitude-dependent potential predictability studies are rare, it is impossible to adequately estimate the model-dependence of the presented structures. Yet, the presented anomaly correlation structure of the AMOC is similar to the results of the coupled model experiments of Kröger et al. (2012) which show a peak of predictability around 50°N for the forecast years 1 to 5. Additionally, previous studies on initialized AMOC predictability at individual latitudes found comparable predictable lead times to the AMOC predictable lead times presented here (chapter 2.4). Nevertheless, further latitude-dependent studies using initialized hindcast ensembles from coupled models would be helpful to increase the robustness of the conclusions.

At present, measured long-term time series of the AMOC or the MHT are currently only available at 26.5°N and at 41°N (Cunningham et al., 2007; Willis, 2010; Johns et al., 2011; Hobbs and Willis, 2012). Thus, for the near future, latitude-dependent predictability studies cannot avoid verifying their hindcast ensembles against model data and will therefore remain model-based. Nevertheless, observations at two latitudes might not be sufficient to further a complete understanding of AMOC and MHT predictability, and an open demand remains for deploying observation systems at more latitudes.

As multi-decadal variations of the AMOC and the MHT were shown to affect the North American and European climate (e.g., Sutton and Hudson, 2005; Pohlmann et al., 2006), skillful predictions of both quantities could be of considerable benefit to society. The link between the predictability of the AMOC or the MHT and the predictability of the North Atlantic climate is not the focus of the present study. However, en route to predictions of the North Atlantic climate, it needs to be considered that the AMOC and the MHT and especially their predictability are not interchangeable. Furthermore, the predictability of the AMOC or the MHT at one particular latitude cannot be generalized to represent the predictability of the AMOC or the MHT for the entire North Atlantic region.

BIBLIOGRAPHY

Baehr, J. (2010). Influence of the 26°N RAPID-MOCHA array and florida current cable observations on the ECCO-GODAE state estimate. *J. Phys. Oceanogr.*, 40:865–879.

Baehr, J., Hirschi, J., Beismann, J.-O., and Marotzke, J. (2004). Monitoring the meridional overturning circulation in the North Atlantic: A model-based array design study. *J. Mar. Res.*, 62:283–312.

Bellucci, A., Gualdi, S., Scoccimarro, E., and Navarra, A. (2008). NAO-ocean circulation interactions in a coupled general circulation model. *Clim. Dyn.*, 31:759–777.

Bingham, R., Hughes, C., Roussenov, V., and Williams, R. (2007). Meridional coherence of the North Atlantic meridional overturning circulation. *Geophys. Res. Lett.*, 34:1–6.

Boer, G. (2004). Long time-scale potential predictability in an ensemble of coupled climate models. *Clim. Dyn.*, 23:29–44.

Boer, G. (2009). Changes in interannual variability and decadal potential predictability under global warming. *J. Climate*, 22:3098–3109.

Bryden, H. and Imawaki, S. (2001). Ocean heat transport. In Siedler, G., Church, J., and Gould, J., editors, *Ocean circulation and climate: observing and modelling the global ocean*, volume 77 of *International Geophysics Series*, chapter 6.1, pages 455–474. Academic Press, San Francisco.

Chen, M., Wang, W., and Kumar, A. (2010). Prediction of monthly-mean temperature: The roles of atmospheric and land initial conditions and sea surface temperature. *J. Climate*, 23:717–725.

Chidichimo, M., Kanzow, T., Cunningham, S., Johns, W., and Marotzke, J. (2010). The contribution of eastern-boundary density variations to the Atlantic meridional overturning circulation at 26.5°N. *Ocean Science*, 6:475–490.

Collins, M. (2002). Climate predictability on interannual to decadal time scales: The initial value problem. *Clim. Dyn.*, 19:671–692.

Collins, M. and Allen, M. (2002). Assessing the relative roles of initial and boundary conditions in interannual to decadal climate predictability. *J. Climate*, 15:3104–3109.

Collins, M., Botzet, M., Carril, A., Drange, H., Jouzeau, A., Laif, M., Masina, S., Otteraa, O., Pohlmann, H., Sorteberg, A., Sutton, R., and Terray, L. (2006). Interannual to decadal climate predictability in the North Atlantic: A multimodel-ensemble study. *J. Climate-Special Section*, 19(7):1195–1203.

Collins, M. and Sinha, B. (2003). Predictability of decadal variations in the thermohaline circulation and climate. *Geophys. Res. Lett.*, 30(6):1–4.

Cunningham, S., Baringer, M., Toole, J., sterhaus, S., Fischer, J., Piola, A., McDonagh, E., Lozier, S., Send, U., Kanzow, T., Marotzke, J., Rhein, M., Garzoli, S., Rintoul, S., Speich, S., Wijffels, S., Talley, L., Baehr, J., Meinen, C., Treguier, A.-M., and Lherminier, P. (2010). The present and future system for measurning the Atlantic meridional overturning circulation and heat transport. *Proceedings of OceanObs09: Sustained Ocean Observations and Information for Society*, 2:1–16.

Cunningham, S., Kanzow, T., Rayner, D., Baringer, M., Johns, W., Marotzke, J., Longworth, H., Grant, E., Hirschi, J.-M., Beal, L., Meinen, C., and Bryden, H. (2007). Temporal variability of the Atlantic meridional overturning circulation at 26.5°N. *Science*, 317:935–938.

Czaja, A., Robertson, A., and Huck, T. (2003). The role of Atlantic ocean-atmosphere coupling in affecting North Atlantic Oscillation variability. In Hurrell, J., Kushnir, Y., Ottersen, G., and Visbeck, M., editors, *The North Atlantic Oscillation*, pages 147–172. American Geophysical Union, Washington, D.C.

Dong, B. and Sutton, R. (2002). Variability in North Atlantic heat content and heat transport in a coupled ocean-atmosphere GCM. *Clim. Dyn.*, 19:485–497.

Drijfhout, S. and Hazeleger, W. (2006). Changes in MOC and gyre-induced Atlantic Ocean heat transport. *Geophys. Res. Lett.*, 33:1–4.

Eden, C. and Willebrand, J. (2001). Mechanism of interannual to decadal variability of the North Atlantic circulation. *J. Climate*, 14:2266–2280.

Ferrari, R. and Ferreira, D. (2011). What processes drive the ocean heat transport? *Ocean Modelling*, 38:171–186.

Fischer, M., Biastoch, A., Behrens, E., and Baehr, J. (2013). Observing system observations for a Line W based AMOC observing system. *submitted to Ocean Dyn.*

GARP (1975). Global Atmospheric Research Programme: The physical basis of climate and climate modelling. Report of the international study conference in Stockholm, organized by WMO and ICSUN and supported by UNEP. *GARP Publication Series*, 16:1–265.

Getzlaff, J., Böning, C., Eden, C., and Biastoch, A. (2005). Signal propagation related to the North Atlantic overturning. *Geophys. Res. Lett.*, 32:1–4.

Griffies, S. and Bryan, K. (1997). Predictability of North Atlantic multidecadal climate variability. *Science*, 275:181–184.

Hall, M. and Bryden, H. (1982). Direct estimates and mechanisms of ocean heat transport. *Deep-Sea Research*, 29:339–359.

Hermanson, L. and Sutton, R. T. (2009). Case studies in interannual to decadal climate predictability. *Clim. Dyn.*, 35:1169–1189.

Hirschi, J., Baehr, J., Marotzke, J., Stark, J., Cunningham, S., and Beismann, J.-O. (2003). A monitoring design for the Atlantic meridional overturning circulation. *J. Geophys. Res.*, 30(7):1–4.

Hirschi, J. and Marotzke, J. (2007). Reconstructing the meridional overturning circulation from boundary densities and the zonal wind stress. *J. Phys. Oceanogr.*, 37:743–763.

Hirschi, J. J.-M., Killworth, P., and Blundell, J. (2007). Subannual, seasonal, and interannual variability of the North Atlantic meridional overturning circulation. *J. Phys. Oceanogr.*, 37:1246–1265.

Hobbs, W. and Willis, J. (2012). Midlatitude North Atlantic heat transport: A time series based on satellite and drifter data. *J. Geophys. Res.*, 117:1–14.

Hurrell, J., Delworth, T., Danabasoglu, G., Drange, H., Drinkwater, K., Griffies, S., Holbrook, N., Kirtman, B., Keenlyside, N., Latif, M., Marotzke, J., Murphy, J., Meehl, G. A., Palmer, T., Pohlmann, H., Rosati, T., Seager, R., Smith, D., Sutton, R., Timmermann, A., Trenberth, K. E., Tribbia, J., and Visbeck, M. (2010). Decadal climate variability, predictability and prediction: Opportunities and challenges. *Proceedings of OceanObs09: Sustained Ocean Observations and Information for Society*, 1:1–12.

Hurrell, J., Kushnir, Y., Ottersen, G., and Visbeck, M. (2003). An overview of the North Atlantic Oscillation. In Hurrell, J., Kushnir, Y., Ottersen, G., and Visbeck, M., editors, *The North Atlantic Oscillation*, pages 1–35. American Geophysical Union, Washington, D.C.

Jayne, S. and Marotzke, J. (2001). The dynamics of ocean heat transport variability. *Rev. Geophys.*, 39:385–411.

Johansson, A. (2007). Prediction skill of the NAO and PNA from daily to seasonal time scales. *J. Clim.*, 20:1957–1975.

Johns, W., Baringer, M., Beal, L., Cunningham, S., Kanzow, T., Bryden, H., Hirschi, J., Marotzke, J., Meinen, C., Shaw, B., and Curry, R. (2011). Continuous, array-based estimates of Atlantic Ocean heat transport at 26.5°N. *J. Clim.*, 24:2429–2449.

Jungclaus, J. and Koenigk, T. (2010). Low-frequency variability of the artic climate: the role of the oceanic and atmospheric heat transport variations. *Clim. Dyn.*, 34:265–279.

Kanzow, T., Cunningham, S., Rayner, D., Hirschi, J.-M., Johns, W., Baringer, M., Bryden, H., Beal, L., Meinen, C., and Marotzke, J. (2007). Observed flow compensation assiciated with the MOC at 26.5°N in the Atlantic. *science*, 317:938–941.

Kanzow, T., Johnson, H., Marshall, D., Cunningham, S. A., Hirschi, J.-M., Mujahib, A., and Bryden, H. (2009). Basinwide integrated volume transports in an eddy-filled ocean. *J. Phys. Oceanogr.*, 39:3091–3110.

Keenlyside, N., Latif, M., Jungclaus, J., Kornblueh, L., and Roeckner, E. (2008). Advancing decadal-scale climate prediction in the North Atlantic sector. *Nature Lett.*, 453:84–88.

Köhl, A. (2005). Anomalies of meridional overturning: Mechanisms in the North Atlantic. *J. Phys. Oceanogr.*, 35:1455–1472.

Köhl, A. and Stammer, D. (2008). Variability of the meridional overturning in the North Atlantic from the 50-year GECCO state estimation. *J. Phys. Oceanogr.*, 38:1913–1930.

Kröger, J., Müller, W., and von Storch, J.-S. (2012). Impact of different ocean reanalyses on decadal climate prediction. *Clim. Dyn.*, 39:795–810.

Latif, M., Böning, C., Willebrand, J., Biastoch, A., Dengg, J., Keenlyside, N., and Schweckendiek, U. (2006a). Is the thermohaline circulation changing? *J. Climate*, 19:4631–4637.

Latif, M., Collins, M., Pohlmann, H., and Keenlyside, N. (2006b). A review of predictability studies of Atlantic sector climate on decadal time scales. *J. Climate-Special Section*, 19:5971–5987.

Latif, M., Roeckner, E., Botztet, M., Esch, M., Haak, H., Hagemann, S., Jungclaus, J., Legutke, S., Marsland, S., Mikolajewicz, U., and Mitchell, J. (2004). Reconstructing, monitoring, and predicting multidecadal-scale changes in the North Atlantic thermohaline circulation with sea surface temperature. *J. Climate*, 17:1605–1614.

Lee, T. and Marotzke, J. (1998). Seasonal cycle of meridional overturning and heat transport of the Indian Ocean. *J. Phys. Oceanogr.*, 28:923–943.

Lorenz, E. (1975). The physical basis of climate and climate modelling: Climate Predictability. *Global Atmospheric Research Programme (GARP) Publication Series, WMO*, 16:132–136.

Lozier, M., Roussenov, V., Reed, M., and Williams, R. (2010). Opposing decadal changes for the North Atlantic meridional overturning circulation. *Nature Geoscience*, 3:728–734.

Lumpkin, R. and Speer, K. (2007). Global ocean meridional overturning. *J. Phys. Oceanogr.*, 37:2550–2562.

Marotzke, J., Giering, R., Zhang, K., Stammer, D., Hill, C., and Lee, T. (1997). Hydrostatic, quasi-hydrostatic and non-hydrostatic ocean modeling. *J. Geosphys. Res.*, 102:5733–5752.

Marshall, J., Hill, C., Perelman, L., and Adcroft, A. (1997). Hydrostatic, quasi-hydrostatic and non-hydrostatic ocean modeling. *J. Geosphys. Res.*, 102:5733–5752.

Matei, D., Baehr, J., Jungclaus, J., Haak, H., Müller, W., and Marotzke, J. (2012a). Multiyear prediction of monthly mean Atlantic meridional overturning circulation at 26.5°N. *Science*, 335:76–79.

Matei, D., Pohlmann, H., Jungclaus, J., Müller, W., Haak, H., and Marotzke, J. (2012b). Two tales of initializing decadal climate prediction experiments with the ECHAM5/MPI-OM model. *J. Clim.*, 25(24):8502–8523.

Meehl, G. A., Goddard, L., Murphy, J., Stouffer, R. J., Boehr, G., Dixon, G. D. K., Giorgetta, M. A., Greene, A. M., Hawkins, E., Hegerl, G., Karoly, D., Keenlyside, N., Kimoto, M., Kirtman, B., Navarra, A., Pulwarty, R., Smith, D., Stammer, D., and Stockdale, T. (2009). Decadal prediction: Can it be skillful? *Bull. Amer. Meteor. Soc.*, 90:1467–1485.

Mehta, V., Meehl, G. A., Goddard, L., Knight, J., Kumar, A., Latif, M., Lee, T., Rosati, A., and Stammer, D. (2011). Decadal climate predictability and prediction: Where are we? *Bull. Amer. Meteor. Soc.*, 92:637–640.

Mosedale, T., Stephenson, D., Collins, M., and Mills, T. (2005). Granger causality of coupled climate processes: Ocean feedback on the North Atlantic Oscillation. *J. Clim.*, 19:1182–1194.

Msadek, R., Dixon, K., Delworth, T., and Hurlin, W. (2010). Assessing the predictability of the Atlantic meridional overturning circulation and associated fingerprints. *Geophys. Res. Lett.*, 37:1–5.

Msadek, R., Johns, W., Yeager, S., Danabasoglu, G., Delworth, T., and Rosati, A. (2013). The Atlantic meridional heat transport at 26.5°N and its relationship with the MOC in the RAPID array and the GFDL and NCAR coupled models. *J. Clim*, in press.

Murphy, A. (1988). Skill scores based on the mean square error and their relationships to the correlation coefficient. *Monthly Weather Review*, 116:2417–2424.

Park, W. and Latif, M. (2004). Ocean dynamics and the nature of sea-air interactions over the North Atlantic at decadal time scales. *J. Climate*, 18:982–995.

Pohlmann, H., Botzet, M., Latif, M., Roesch, A., Wild, M., and Tschuk, P. (2004). Estimating the decadal predictability of a coupled AOGCM. *J. Climate*, 17:4463–4472.

Pohlmann, H., Jungclaus, J., Köhl, A., Stammer, D., and Marotzke, J. (2009). Initializing decadal climate predictions with the GECCO oceanic synthesis: Effects of the North Atlantic. *J. Climate*, 22:3926–3938.

Pohlmann, H., Sienz, F., and Latif, M. (2006). Influence of the multidecadal Atlantic meridional overturning circulation variability on european climate. *J. Climate-Special Section*, 19:6062–6067.

Pohlmann, H., Smith, D., Balmasede, M., Keenlyside, N., Masina, S., Matei, D., Müller, W., and Rogel, P. (2013). Predictability of the mid-latitude Atlantic meridional overturning circulation in a multi-model system. *Clim. Dyn.*, in press.

Robson, J., Sutton, R., and Smith, D. (2012). Initialized decadal predictions of the rapid warming of the North Atlantic Ocean in the mid 1990s. *Geophys. Res. Lett.*, 39:1–6.

Rodwell, M. (2003). On the predictability of North Atlantic climate. In Hurrell, J., Kushnir, Y., Ottersen, G., and Visbeck, M., editors, *The North Atlantic Oscillation*, pages 173–192. American Geophysical Union, Washington, D.C.

Rowell, D. (1998). Assessing potential seasonal predictability with an ensemble of multidecadal GCM simulations. *J. Climate*, 11:109–120.

Sachs, L. (1997). *Angewandte Statistik: Anwendung statistischer Methoden*, chapter 551 Prüfung des Vorhandenseins einer Korrelation sowie einige Vergleiche, pages 537–542. Springer, Berlin Heidelberg.

Smith, D., Cusack, S., Colman, A., Folland, C., Harris, G., and Murphy, J. (2007). Improved surface temperature prediction for the coming decade from a global climate model. *Science*, 317:796–799.

Sutton, R. and Hudson, D. (2005). Atlantic ocean forcing of North American and European summer climate. *Science*, 309:115–118.

Talagrand, O. and Courtier, P. (1987). Variational assimilation of meteorological observations with the adjoint vorticity equation. I: Theory. *Quart. J. Roy. Meteorol. Soc.*, 113:1311–1328.

Tiedje, B., Köhl, A., and Baehr, J. (2012). Potential predictability of the North Atlantic heat transport based on an oceanic state estimate. *J. Climate*, 25(24):8475–8486.

Troccoli, A. and Palmer, T. (2007). Ensemble decadal predictions from analysed initial conditions. *Phil. Trans. R. Soc. A*, 365:2179–2191.

Visbeck, M., E.P.Chassignet, Curry, R., Delworth, T., Dickons, B., and Krahmann, G. (2003). The ocean's response to North Atlantic Oscillation variability. In Hurrell, J., Kushnir, Y., Ottersen, G., and Visbeck, M., editors, *The North Atlantic Oscillation*, pages 113–145. American Geophysical Union, Washington, D.C.

von der Haar, T. and Oort, A. (1973). New estimate of annual poleward energy transport by northern hemisphere oceans. *J. Phys. Oceanogr.*, 3:169–172.

von Storch, H. and Zwiers, F. (1999). *Statistical analysis in climate research*, chapter 17.1 The decorrelation time, pages 371–374. Cambridge University Press, Cambridge.

Willis, J. (2010). Can in situ floats and satellite altimeters detect long-term changes in Atlantic ocean overturning? *Geophys. Res. Lett.*, 37:1–5.

Zhang, S. (2011). Impact of observation-optimized model parameters on decadal predictions: Simulation with a simple pycnocline prediction model. *Geophys. Res. Lett.*, 38:1–5.

ACKNOWLEDGMENTS

First and foremost I wish to thank my advisor Johanna Baehr whose scientific guidance and advice was invaluable for my whole PhD study at its various stages. Above all, I would like to thank her for her constant support, her patient encouragement, and her unfailing dedication to this project.

I would also like to thank Armin Köhl, my co-advisor, for his constructive comments on this thesis and his technical support without which I couldn't even have started my studies. I am also grateful to Jin-Song von Storch for taking the time to be the chair of my advisory panel.

Many thanks go to my colleagues in our research group and my former and present office- and floor-mates for their scientific and moral support, for their open ears to my worries and for all the nerdy fun we had together. Specifically: Robert Piontek, Matthias Fischer, Charlotte Mielke, Sebastian Brune, Ralph Rösner, Oliver Kunst, Nicole Beisiegel, and Ina Lorkowski.

I would also like to thank my beloved family and friends who distracted me from my studies and colored my world outside of my office.

My deepest thanks go to Nikolai Redlich. Words fail me to express how grateful I am for his constant love and support.